

# **Development of Multi-Functional Flame Sprayed High Entropy Alloy (HEA) Coatings**

by

Sanhita Pal

A thesis submitted in partial fulfillment of the requirements for the degree of

Master of Science

Department of Mechanical Engineering

University of Alberta

© Sanhita Pal, 2022

## **Abstract**

High entropy alloys (HEAs) are a new class of advanced metallic materials that have received significant attention in recent years due to their stable microstructures and promising properties. They are characterized by their peculiar mixing of five or more principal elements in equimolar concentrations. It has been argued that HEAs exhibit high configurational entropy features that arise from compositionally complex mixing, which enable them to stabilize a single-phase solid solution structure. Owing to the solid solution phase formations, these alloys have shown immense structural properties, including excellent strength and fracture toughness, which make them potential candidates for extreme environmental conditions.

Surface modification allows the possibility of combining bulk properties of the substrate with the tailored capabilities of coatings, thereby creating a new range of possibilities. Smart functional coatings incorporating new functionalities and coherent responses have surpassed the traditional capabilities of coatings and have taken surface technologies to new heights. Presently, the potential benefits of HEAs are being extended to development of coatings via thermal spraying. The exploration of high entropy alloys in conjunction with thermal spraying techniques to address numerous challenges in extreme engineering environments is still in their early stage of development. Only a few studies were attempted to develop thermal-sprayed HEA coatings to protect against wear and corrosion. However, limited, if any, studies on functional properties such as thermal, electrical, and magnetic properties of thermal sprayed HEA coatings have been pursued.

Solid particle erosion is a typical wear mode that negatively impacts the longevity of parts in many sectors like aerospace, marine, mining, wind energy, and oil and gas; thus improving the erosion resistance of the components in this sector is economically important. The second aspect of this work revolves around studying the solid particle erosion properties of these coatings.

The goal of this study was to develop novel AlCoCrFeMo, AlCoCrFeMoW and AlCoCrFeMoV HEA compositions to understand how tungsten (W) and vanadium (V) additions in AlCoCrFeMo influence the evolution of microstructures, phase formations, microhardness, electrical resistivity and solid particle erosion properties.

A cost-effective flame spray technique was utilized to produce three different equiatomic AlCoCrFeMo, AlCoCrFeMoW, and AlCoCrFeMoV HEA coatings on stainless steel substrates. To avoid conductivity and short-circuiting during Joule heating experiments, an insulating layer of alumina was deposited on to the substrates before coating depositions. The coatings were characterized using XRD and SEM. The Vickers microhardness technique was used to quantify hardness. A custom assembly was used to determine the electrical resistivity and analyze the Joule heating performance of the coatings. The Joule heating performance was compared on the basis of the rate of increase in surface temperature for a given power input. Solid particle erosion studies were performed using a modified version of the ASTM G-76 standard with a low-pressure cold spray unit, using garnet sand as the erodent and the surface morphology was studied.

The microstructure of the HEA coatings showed the presence of multiple oxide regions along with solid-solution phases. The HEA coatings had an average thickness of approximately  $153 \pm 14 \mu\text{m}$

with porosity between 2 to 3%. High hardness values were recorded for all coatings with AlCoCrFeMoV showing the highest hardness. The electrical resistivity values were higher for all the HEA coatings compared to flame-sprayed Ni-20Cr and NiCrAlY coatings and AlCoCrFeNi HEA thin film, which may be attributed to the characteristics of HEAs, such as severe lattice distortion and solute segregations. The coatings have shown improved Joule heating performance when compared with conventional Ni-20Cr flame-sprayed coatings, as indicated by the higher rate of increase in surface temperature for a given power input. Solid particle erosion studies indicated that the coatings underwent a brittle mode of failure. The erosion rate of all three coatings was found to be independent of temperature on testing up to 250 °C. It was statistically determined that AlCoCrFeMo and AlCoCrFeMoW coatings have better solid particle erosion resistance than the AlCoCrFeMoV coatings. The erosion rate of the coatings was found to be linearly dependent on the H/E (elastic strain to break) ratio and decreased with increasing value of H/E ratio. The combined interaction of high hardness, increased electrical resistivity and improved erosion resistance properties suggests that the flame-sprayed HEA coatings can be used as multi-functional wear-resistant materials for energy generation applications.

## Preface

Parts of Chapter 2 sections 2.1, 2.2, 2.3, 2.4 and 2.5 and parts of chapter 3, sections 3.1, 3.2, 3.3, 3.4 and 3.5 have been published in the conference paper: “Pal S., Nair BR., McDonald A.,2020:” Influence of microstructure on hardness and electric resistivity of flame sprayed high entropy alloy coatings.” International Thermal Spray Conference and Exposition, May 4 – 6, 2022 (Vienna, Austria), DVS-The German Welding Society, (2022), 6 pages on compact disk.”

The findings of chapter 3, sections 3.1, 3.2, 3.3, 3.4 have been included in the proceedings of CSME 2022 as “Pal S., Nair BR., McDonald A.,2020: “Solid Particle Erosion Assessment of Flame-Sprayed High Entropy Alloy Coatings”: Proceedings of the Canadian Society for Mechanical Engineering International Congress 2022, 2022 CSME International Congress, June 5 – 8, 2022 (Edmonton, AB), University of Alberta, (2022), abstract on compact disk.”

Some of the sections included in this thesis have been prepared for submission to peer-reviewed journals as follows:

Parts of chapter 2, sections 2.1, 2.2, 2.3, 2.4 and 2.5 and parts of chapter 3, sections 3.1, 3.2, 3.3, 3.4 and 3.5 have been published by the “Journal of Materials Science, Springer” entitled as “Toward understanding the microstructure and electrical resistivity of thermal-sprayed high-entropy alloy coatings.” DOI : 10.1007/s10853-022-07921.

## Acknowledgement

*I would like to express my sincere gratitude to my supervisor Prof. André McDonald for the continuous support of my MSc studies and research. His patience, motivation, enthusiasm, experience, expertise, guidance and amazing organizational skills have helped me to complete my MSc in an orderly and timely manner. I am indebted to Dr. McDonald for providing me with the opportunity to be a part of his research group and to attend various professional activities during the program.*

*I would like to extend my gratitude to Dr. Rakesh Bhaskaran Nair, Post-Doctoral Fellow in our group for providing me with valuable insights on high entropy alloys and experimentation. I am also very thankful to Adekunle Ogunbadejo and my other colleagues for helping me from time to time with laboratory matters. A special thanks to Nathan Gerein, Guibin Ma and Rebecca Feng of the Earth Sciences Department for their help with SEM and XRD. I am also thankful to Dr. Philip Egberts and his research group at the University of Calgary for letting me use their Nanoindentation facility.*

*In the end, I am incredibly grateful to my parents Goutam and Mithu for letting me pursue my dreams, being present for me whenever I needed them, tolerating me and living with my absence from their life. I am obliged to Harshal for bringing joy and statistics to my life and being a constant support. I am so thankful to all my friends for being patient, listening to my cribbing and encouraging me whenever I was low. Lastly, I thank the universe for bringing my kitties- the love of my life, Mota and Luna to my life who made me immensely patient and were always by my side whenever I was sad or lonely.*

# Contents

<b>Chapter Title</b>	<b>Page No</b>
<b>Abstract</b> .....	ii
<b>Preface</b> .....	v
<b>Acknowledgement</b> .....	vi
<b>List of Tables</b> .....	ix
<b>List of Figures</b> .....	xi
<b>Commonly Used Abbreviations</b> .....	xiv
<b>Chapter 1: Introduction</b>	
1.1.High Entropy Alloy (HEA) .....	1
1.2.HEA Coatings .....	6
1.3.Thermal Sprayed HEA Coatings .....	11
1.4.Thermal Sprayed Coatings for Resistive Heating Applications .....	16
1.5. Rationale behind the designing of the novel HEA compositions used in the study.....	21
1.6. Solid Particle Erosion .....	23
1.7.The Hardness to Elastic Modulus ( $H/E$ ) Ratio and its relevance in wear and erosion .....	32
1.8. Objectives .....	36
1.9. Motivation .....	36
1.10.Thesis Organization .....	37

## **Chapter 2: Experimental Methodology**

2.1. Materials .....	38
2.2. Coating Fabrication .....	41
2.3. Coating Characterization .....	43
2.4. Microhardness .....	43
2.5. Electrical Resistivity and Joule Heating Performance .....	44
2.6. Nanoindentation .....	46
2.7. Solid Particle Erosion .....	48

## **Chapter 3: Result and Discussion**

3.1.X-Ray Diffraction (XRD) .....	51
3.2.SEM .....	54
3.3. Microhardness .....	60
3.4.Electrical Resistivity and Temperature Coefficient of Resistance (TCR) .....	62
3.5. Joule Heating Performance .....	67
3.6.Nanoindentation / Elastic Modulus and Nanohardness .....	71
3.7.Solid Particle Erosion .....	72
<b>Chapter 4: Conclusion and Summary.....</b>	<b>84</b>
<b>Chapter 5: Recommendations for Future Work.....</b>	<b>86</b>
<b>References .....</b>	<b>89</b>
<b>Appendix .....</b>	<b>101</b>

## List of Tables

<b>Table 1.</b> Chemical composition of the HEA powders obtained from EDS in comparison to the nominal composition in atomic percentage.....	41
<b>Table 2.</b> The flame spray parameters used in the study. Note FMR is a relative measure for regulating the flow rate of the powders.....	42
<b>Table 3.</b> Indicates the set of parameters used in erosion testing.....	49
<b>Table 4.</b> Porosity and thickness of the HEA and alumina layer.....	57
<b>Table 5.</b> Elemental composition of the HEA Coatings in atomic percentage as obtained from EDS analysis.....	57
<b>Table 6.</b> Average resistivity and TCR value of the flame sprayed HEA coatings.....	63
<b>Table 7.</b> p-values of the paired t-tests results between Material 1 and Material 2. The hypothesis for the given t-test is there is no significant difference in Joule heating performance between Material 1 and Material 2.....	70
<b>Table 8.</b> Indicating the microhardness, nano hardness, elastic moduli, $H/E$ and $H^3/E^2$ of the different coating systems under study.....	71
<b>Table 9.</b> Shows the $p$ -values of the results of the independent $t$ -test assuming equal variances. The null hypothesis was chosen as: “there is no significant difference in the mean erosion rate between samples eroded at room temperature and an elevated temperature of 250 °C.” .....	79

**Table 10.** Shows the  $p$ -values of the paired  $t$ -tests results between Material 1 and Material 2. The hypothesis for the given  $t$ -test is there is no significant difference in the mean erosion rate between Material 1 and Material 2 ..... 80

## List of Figures

<b>Figure 1.</b> 2D matrix of a solid solution containing 10 different components. Adapted from Murty <i>et al.</i> 2014 [178].....	2
<b>Figure 2.</b> Schematic diagram of the lattice distortion in a five-component BCC lattice compared to a single component alloy which has no lattice distortion. Adapted from Murty et al. 2014 [178].....	4
<b>Figure 3.</b> Shows the material hypertetrahedron summarizing the design-process-structure-property of HEAs. Adapted from Murty <i>et al.</i> 2014 [178].....	5
<b>Figure 4 (a).</b> Schematic diagram of flame spraying .....	12
<b>Figure 4 (b).</b> Graphical representation of the wide range of particle velocity and flame temperature available for thermal spraying. Adapted from Ang and Berndt, 2014 [53].....	13
<b>Figure 5.</b> Shows the different industries which incur substantial losses due to the damaging effect of solid particle erosion. The pictures in the inset show some of the degraded components a). Eroded turbine blades, b). The progressive change in shape of turbine blade because of erosion, c). Cross-sectional image of a pipe that has been subjected to solid particle erosion, d). Erosion-Corrosion of pipe.....	25
<b>Figure 6.</b> SEM images of feedstock powder of a). AlCoCrFeMo, b). AlCoCrFeMoW and c). AlCoCrFeMoV .....	39
<b>Figure 7.</b> EDS Mapping of feedstock powder of a). AlCoCrFeMo, b). AlCoCrFeMoW and c). AlCoCrFeMoV .....	40
<b>Figure 8.</b> Schematic of Joule heating experiment .....	44

<b>Figure 9.</b> A schematic representation of load versus indenter displacement showing quantities used in the analysis. Source Oliver and Pharr, 1992[120].....	47
<b>Figure 10.</b> SEM image of garnet sand (erodent) used in the solid particle erosion study.....	49
<b>Figure 11.</b> Schematic diagram of the high-temperature solid particle erosion setup for 30° impact angle [98].....	50
<b>Figure 12.</b> XRD Profile of the HEA powders. It shows the presence of two types of BCC phases. The lattice parameters of the two BCC phases have been indicated.....	52
<b>Figure 13.</b> XRD profile of flame sprayed HEA coating .....	53
<b>Figure 14.</b> SEM micrographs at low (a, b, c) and high (d, e, f) magnifications of (a and d) AlCoCrFeMo, (b and e) AlCoCrFeMoW, and (c and f) AlCoCrFeMoV of the flame sprayed HEA coatings .....	55
<b>Figure 15.</b> EDX map of a) AlCoCrFeMo, b) AlCoCrFeMoW, and c) AlCoCrFeMoV of the flame sprayed HEA coatings .....	59
<b>Figure 16.</b> Plot indicating the Vicker's Microhardness values of the flame sprayed HEA coatings.....	61
<b>Figure 17.</b> Plot showing the variation of voltage with current.....	62
<b>Figure 18.</b> Plot showing variation of electrical resistivity with temperature.....	64
<b>Figure 19.</b> Graph of electrical resistivity versus oxide content of flame-sprayed HEA coatings.....	66

<b>Figure 20.</b> Plot showing the variation of temperature with time at a). 3.5 W, b). 35 W and c). 75 W.....	67
<b>Figure 21.</b> Plot comparing the Joule Heating performance of the three HEA coatings with Ni-20Cr at different input powers. The labels above each column are a quantitative indication of the performance improvement when compared with Ni-20Cr at similar testing conditions.....	69
<b>Figure 22.</b> Shapes of the eroded scars obtained at different erosion impact angles.....	73
<b>Figure 23.</b> Comparison of solid particle erosion rate of the three HEA coatings at varying impact angle .....	74
<b>Figure 24.</b> Shows the low and high magnification scanning electron micrograph of the eroded surface morphology of AlCoCrFeMo flame sprayed HEA coatings at different testing conditions.....	75
<b>Figure 25.</b> Shows the low magnification scanning electron micrograph of the eroded surface morphology of 1. AlCoCrFeMo, 2. AlCoCrFeMoW, 3. AlCoCrFeMoV flame sprayed HEA coatings at different testing conditions .....	76
<b>Figure 26.</b> Comparison of solid particle erosion rate of the three HEA coatings at room and elevated temperatures .....	78
<b>Figure 27.</b> Shows the dependence of erosion rate on the $H/E$ ratio for the three HEA coatings tested under different conditions .....	82

## **Commonly Used Abbreviations**

HEA- High Entropy Alloy

SPE- Solid Particle Erosion

TS- Thermal Spray

FCC- Face Centered Cubic

BCC- Body Centered Cubic

HCP- Hexagonal Closed Pack

HVOF- High Velocity Oxy-Fuel

XRD- X-Ray Diffraction

SEM- Scanning Electron Microscopy

EDS/EDX- / Energy Dispersive X-Ray Spectroscopy

TEM- Transmission Electron Microscopy

TCR- Temperature Coefficient of Resistance

HV- Hardness in Vicker's Scale

GPa- Giga-Pascal

# **Chapter 1**

## **Introduction**

### **1.1. High Entropy Alloy (HEA)**

High entropy alloys (HEAs) are a novel class of materials which have received widespread attention recently because of their outstanding physical and mechanical properties. They are known for their high strength and fracture toughness at room [1-3] and high temperatures [4, 5], excellent resistance to wear [2], corrosion resistance [6-9], and high-temperature oxidation [6], and unique electrical and magnetic properties [10-12]. The most unique aspect of HEAs is their ability to form simple solid solution structures irrespective of their complex mixture of elements.

### **Background and Definition**

For the past two decades, a unique concept of alloy designing by the mixing of multiple principal elements in high concentration has been in vogue. This unconventional form of alloy designing was first explored by the research group of Jien-Wei-Yeh in 2004 who was the first to coin the term high entropy alloy (HEA). According to the original definition proposed by Yeh *et al.* [13], HEAs are those which are composed of five or more elements in equimolar or near-equimolar ratio with the atomic concentration of each principal element being between 5% and 35%. Around the same time, another research group led by Brian Cantor unaware of the term coined by Yeh independently published their work on equiautomic FeCrMnNiCo referring to it as multi-component alloys [14]. Yeh and Cantor are regarded as the founding fathers of this new class of

materials and their respective works on CuCoNiCrAl<sub>x</sub>Fe and FeCrMnNiCo (also known as Cantor alloys) HEA compositions and their modifications have been widely studied by researchers.

### The Four Core Effects- The reason for the unique properties of HEAs

The uniqueness of HEAs is attributed to the four core effects namely *high configurational entropy, severe lattice distortion, sluggish diffusion* and *cocktail effect*. Figure 1 is a representation of a 2D matrix of a solid solution with 10 different components. It is indicative of the difference in atomic sizes leading to lattice distortion, vacancies and other defects which are characteristics of HEAs.

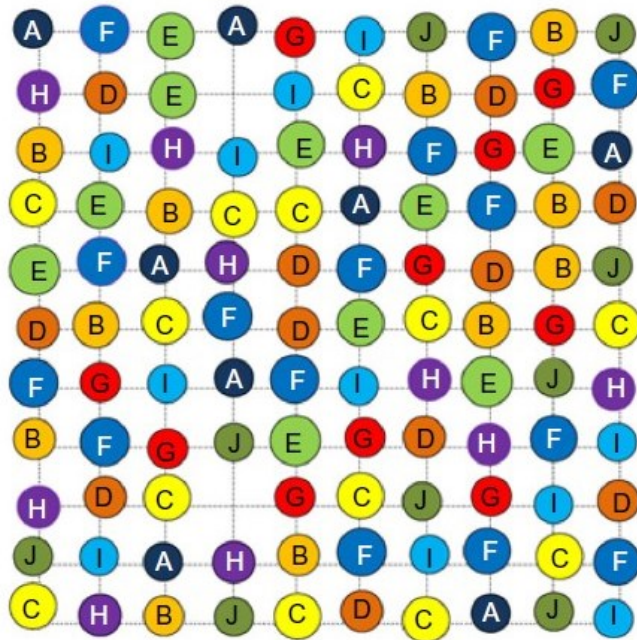


**Figure 1.** 2D matrix of a solid solution containing 10 different components. Adapted from Murty *et al.* 2014 [178].

The high entropy effect influences the thermodynamic phase formation ability and favours the formation of simple solid solution phases (FCC, BCC, HCP). By the mixture of different elements, there is a decrease in the diffusion rates which is referred to as sluggish diffusion. This stabilizes the HEAs from phase decomposition or coarsening of nano-precipitates. It also provides various advantages in controlling microstructure and properties like easiness to get supersaturated state and fine precipitates, increased recrystallization temperature, slower grain growth, reduced particle coarsening rate, and increased creep resistance. The presence of multiple principal components/elements results in every atom being surrounded by different kinds of atoms consequently leading to severe lattice strain and stress primarily because of the atomic size difference. Besides the atomic size difference, different bonding energies and crystal structures among constituent elements are also expected to cause even higher lattice distortion because of non-symmetry which changes from site to site. The lattice distortion not only affects various properties but also reduces the thermal effect on properties. Hardness and strength effectively increase because of large solution hardening in the heavily distorted lattice. Figure 2 depicts the lattice distortion in a five-component BCC lattice compared to a single component alloy which has no lattice distortion. The Cocktail Effect refers to the synergy of positive effects from a mixture of different elements with different properties. HEAs might have a single phase, or multiple phases depending on the composition and processing, the whole properties are from the overall contribution of the constituent phases. The mutual interaction and lattice distortion could then accentuate the properties beyond those predicted by the mixture rule – cocktail effect [178].

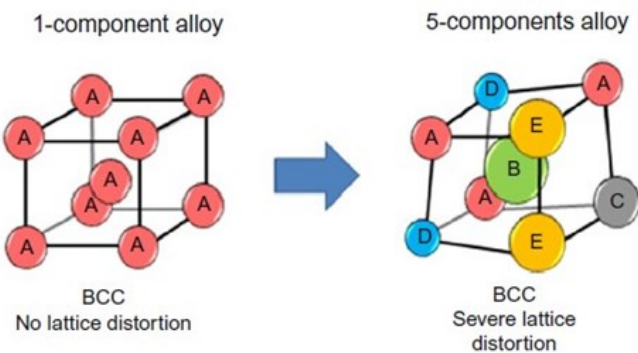


**Figure 2.** Schematic diagram of the lattice distortion in a five-component BCC lattice compared to a single component alloy which has no lattice distortion. Adapted from Murty et al. 2014 [178].

### Manufacturing of HEAs

Figure 3 shows the material hypertetrahedron summarizing the design-process-structure-property of HEAs. HEAs have been produced in a variety of forms like castings, sintered powder metallurgy parts, and films. The processing routes can be broadly classified into three groups, namely, the melting and casting route, powder metallurgy route, and deposition techniques. The processing routes are similar for equiatomic and non-equiatomic compositions. Melting and casting techniques, with equilibrium and nonequilibrium cooling rates, have been employed to produce HEAs in the shape of rods, bars, ribbons, and nanoparticles. The popular melt processing techniques include vacuum arc melting, vacuum induction melting, and melt spinning. Mechanical alloying followed by sintering has been the major solid-state processing route to produce sintered products. Sputtering, plasma nitriding, spraying and cladding are the surface modification techniques used to produce thin films and thick layers of HEAs on various substrates.

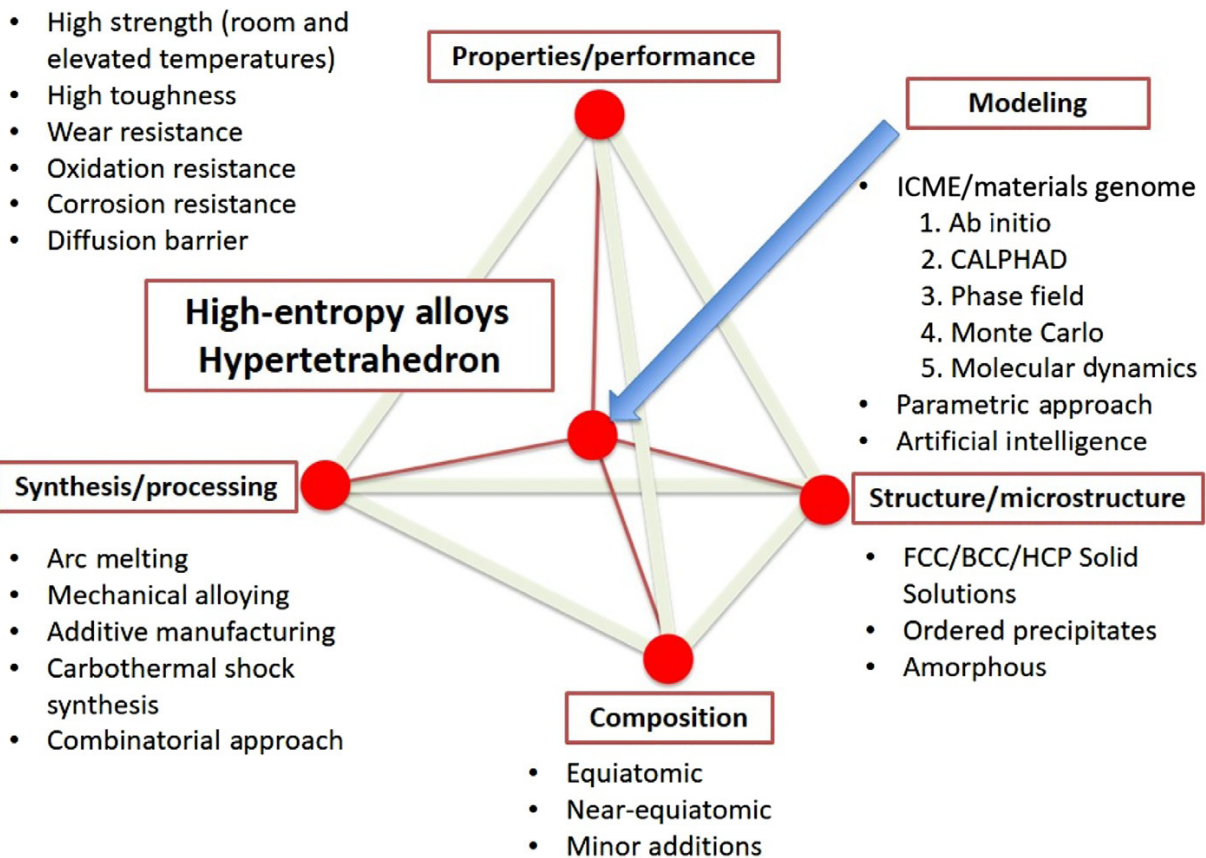


**Figure 3.** Shows the material hypertetrahedron summarizing the design-process-structure-property of HEAs. Adapted from Murty *et al.* 2014 [178].

### Why are HEAs interesting?

With the multi-principal-element-based design approach, the compositional space of alloys can be considerably expanded. According to Cantor's conservative estimate, the total number of possible alloys that may be mapped out of 60 feasible elements is in the order of  $10^{100}$  [15]. Expectedly, the expansion of the compositional space alloys will undoubtedly bring about rich opportunities in

achieving affluent, diverse microstructures as well as structural and functional properties unseen before. For example in contrast to conventional alloys which show a decrease in strength and ductility with increasing temperature the HEA studies on CrMnFeCoNi by Gludovatz *et al.* showed an increase in strength and ductility with increasing temperature making them promising candidates for cryogenic applications [1]. *Thus, the introduction of HEAs has opened the possibility of discovering new efficient alloys to fill targeted needs in niche applications.*

## 1.2. HEA Coatings

Surface modification allows the possibility of combining bulk properties of the substrate with the tailored capabilities of coatings, thereby creating a new range of possibilities. The development of coatings has furthered the inherent limits of materials and broadened the design possibilities by enhancing the surface properties of traditional materials with more desirable surface characteristics and performance. Coatings are present in almost every demanding environment with high-value applications in conditions with corrosive environments, wear protection, thermal insulation, or severe stress applications [16]. Smart functional coatings incorporating new functionalities and coherent responses have overpassed the traditional capabilities of coatings and have taken surface technologies to new heights. Since HEAs exhibit many attractive properties the properties of HEA coatings are of immense interest in surface technology. The different coating technologies of HEAs include sputter deposition [3, 17, 18], laser cladding [19, 20] spraying [21, 22], electrochemical deposition [23, 24] and other cladding techniques like plasma-transferred-arc [25], electrospark deposition [26].

## **HEA coatings their properties and application**

### *Mechanical Behaviour – High Hardness and Elastic Modulus*

Huang *et al.* [27] prepared the TiVCrAlSi HEA coating on the Ti-6Al-4V alloy surface by laser cladding, which had BCC phases and a microhardness close to 1000 HV0.2. Zhang *et al.* [28] prepared the Laser cladded 6FeNiCoSiCrAlTi HEA coating having a simple BCC solid solution with the microhardness of 780 HV<sub>0.5</sub>. FCC coatings CoCrFeNiAl<sub>x</sub>Cu<sub>0.7</sub>Si<sub>0.1</sub> having a high hardness of 502 HV<sub>0.5</sub>. have been prepared by He *et al.* [29]. DC Magnetron Sputtered single phase FCC coatings of FeAlCuCrCoMn having a hardness and Young's modulus of 17.5 and 186 Gpa respectively were studied by Li *et al.* [30]. Reactive-sputtered HEA nitride thin films pioneered by Chen *et al.* [31] are being widely studied because of their super high hardness of over 40 Gpa.

### *Tribological Properties*

The high hardness of the HEA coatings can help in the effective reduction of wear rate since the tribological properties are generally determined by mechanical properties. The excellent wear resistance of HEA coatings has been verified by numerous experiments. Some of them have been summarized below.

Lai *et al.* [32] studied the influence of the substrate bias voltage, on the microstructural and tribological properties of the (AlCrTaTiZr)N films prepared by reactive-magnetron sputtering. An almost constant low coefficient of friction of 0.75 and a low wear rate of  $3.65 \times 10^{-6}$  mm<sup>3</sup>/Nm were achieved at the bias voltage of 150 V. Tian *et al.* [33] prepared the AlCoCrFeNiTi coating consisting of BCC matrix, minor FCC, and ordered BCC solid-solution phases by APS (Atmospheric Plasma Spray). Although the volumetric wear rate increased with an increase in temperature still it was better than laser-cladded NiCrBSi coating at the same temperature. Zhang

*et al.* [34] synthesized the FeCoCrAlCu coating on the Q235 steel by laser surface alloying which had volume and specific wear rate values that were an order of magnitude lower than the substrate in dry-sliding conditions.

### *Corrosion resistance*

Dou *et al.* [35] deposited DC magnetron sputtered FeAlCoCuNiV coatings having single phase FCC solid solution which exhibited better electrochemical corrosion resistance than the 201 stainless steels in acidic alkali and salt corrosion media. Li *et al.* [26] produced AlCoCrFeNi coatings on the AISI 1045 carbon steel by electrospark deposition. They found that the corrosion current of the HEA-coated specimen was significantly lower than those for the 1045 steel and the cast HEA material. It has been observed that the high-entropy effect added to the ‘rapid quenching’ effect arising due to the nature of the preparation processes of the HEA films and coatings facilitates the formation of a single FCC or BCC solid-solution phase or amorphous phase with the more homogeneous microstructure than their bulk counterparts, resulting in an improvement of the corrosion resistance.

### *High-Temperature Stability*

Superhard (AlCrNbSiTiV)N film made by Huang *et al.* [36] exhibited excellent thermal stability and retained a simple FCC structure after annealing at 1000°C for 5 h. Feng *et al.* [37] found that TaNbTiW alloy films revealed no phase changes even after being annealed at 500 and 700°C for 90 min in vacuum whereas, annealing at 900°C, resulted in the formation of only a few oxides peaks. The microhardness of as prepared laser-cladded coatings TiZrNbWMo reached up to 700

HV0.5, which remarkably increased after heat treatment and reached the maximum of about 1300HV0.5 at 800°C Zhang *et al.* [38].

### *Oxidation Resistance*

The weight gains of thermal sprayed AlCrFeMo0.5NiSiTi and AlCoCrFeMo0.5NiSiTi HEA coatings prepared by Huang *et al.* [21] maintained at 1100°C for 150 h was about 8.2 and 9.2 mg/cm<sup>2</sup>, respectively, which were comparable with that of commercial oxidation-resistant NiCrAlY alloys. Shen *et al.* [183] studied the oxidation resistance of (Al<sub>0.34</sub>Cr<sub>0.22</sub>Nb<sub>0.11</sub>Si<sub>0.11</sub>Ti<sub>0.22</sub>)<sub>50</sub>N<sub>50</sub> coating prepared by reactive magnetron sputtering. The thickness of the oxide layer on the coating surface was 290 nm after 50 h of annealing at 900°C and the weight gain after thermal ramping to 1300°C was merely 0.015 mg cm<sup>-2</sup>. The oxidation resistance of these coatings was superior to other nitride coatings.

The high temperature and oxidation resistance of HEA coatings have been attributed to the high mixing entropy of the constituent elements, the lower diffusion coefficients and the re-distribution of solute elements during the annealing treatment, relative to the conventional films and coatings.

### *Physical Properties*

The review article by Tsai *et al.* [39] suggests a low-temperature coefficient of resistance (TCR) and favourable soft magnetic properties in bulk HEA. However, only a limited number of literature highlighting the physical behaviour of HEAs exists [40]. A few works exploring the magnetic and electrical properties have been indicated. Lin *et al.* [41] fabricated BCC FeCoNiCrAlSi thin films with excellent soft magnetic properties. The optimized magnetic properties of thin films obtained had a *Ms* (saturation magnetization) of 9.13×10<sup>5</sup> A/m, *hHc* (coercivity at the hard axis) of 79.6

A/m, and H<sub>k</sub> (out-of-plane uniaxial anisotropy field) of 1.59×103 A/m, respectively. Qiu *et al.* [19] prepared the Al<sub>2</sub>CrFeNiCoCu HEA coating by laser cladding having small coercive force, for use as soft magnetic material. BiFeCoNiMn HEA films prepared by Yao *et al.* [42] using electrodeposition showed soft magnetic behaviour in an as-prepared state, while the annealed films exhibited hard magnetic properties. Cheng *et al.* [43] deposited the amorphous BnbTa- TiZr thin films by magnetron sputtering, having a high electrical resistivity of 246  $\mu\Omega\text{-cm}$ . Lin *et al.* [44] prepared the NiCrSiAlTa thin films by direct current magnetron co-sputtering which when annealed at 300°C exhibited high electrical resistivity of 2215  $\mu\Omega\text{-cm}$  with 10 ppm/ $^{\circ}\text{C}$  of TCR. Recently, Wang *et al.* [45] have studied the resistivity -temperature behaviour of Al<sub>x</sub>CoCrFeNi ( $x=0.7\text{-}1.0$ ) thin films and bulk HEA. The films comprised mixed FCC and BCC phases and exhibited ultra low-temperature coefficient of resistance in a range of  $\pm 10$  ppm/K and the electrical resistivities ranged from 191.8  $\mu\Omega\text{ cm}$  (for  $x=1.0$ ) to 535.9  $\mu\Omega\text{ cm}$  (for  $x = 0.7$ ) which are way higher than those observed for conventional alloys. They have attributed these to severe lattice distortions, phonon scattering, and s-d scattering in transition metal alloys.

*Thus, it can be said that HEA thin films have high electrical resistivity and potential application as resistors.*

#### *Diffusion Retardation*

A series of works by Chang et al [46-49] on HEA nitride films indicated its use as an effective diffusion barrier material. Severe lattice strain and a high packing density caused by different atom sizes, and high cohesive energy, were believed to be the dominant factors for suppressed interdiffusion kinetics through the multi-component barrier materials.

### *Biocompatibility*

Braic *et al.* [50] deposited the (TiZrNbHfTa)N and (TiZrNbHfTa)C coatings on Ti-6Al-4V alloy by co-sputtering technique, with favourable outcomes. The investigated coatings did not induce any cytotoxic response by osteoblasts (24 and 72 h), and good morphology of the attached cells was observed. Cell viability analysis also showed a very high ratio of live cells compared with dead cells. Vladescu *et al.* [51] found in their research that the replacement of Ta by Si in the (TiZrNbTaHf)C coating led to an enhanced surface electrical, low electrical potential and high work function, exhibiting the best biocompatible properties out of the studied HEA.

*The works cited before are an indication of the myriad application of HEA coatings and thin films. Most of the work has focussed on the mechanical or tribological properties of HEA with little emphasis on the physical properties vis-à-vis electrical, magnetic or thermal. The limited literature on these aspects, however, indicates a wide range of possibilities. Moreover, little or no known attempts have been made to explore the multi-functional capabilities of HEA coatings.*

### **1.3. Thermal-sprayed HEA Coatings**

Thermal spraying is a versatile, cost-effective and industrially established surface modification technology with extensive applications in the aerospace, turbines, oil and gas industries to name a few. It is a line-of-sight process, wherein feedstock material, in the form of powder, wire, rod, or suspension, is fed into a spray torch followed by heating up to a molten or near-molten state and propelled toward a base material [52]. Figure 4(a) is a schematic representation of the powder

flame spray process. Thermal spray (TS) processes have been classified into three prime categories based on the energy source: (1) use of combustion heat sources, for example, detonation gun or high-velocity oxygen fuel spray (HVOF); (2) plasma or arc formation using electrical energy, for example, atmospheric plasma spray (APS); and (3) low-temperature processes that use energy evolving from gas expansion, such as, for example, cold spraying (CS). Thermal spraying provides a wide range of flexibility in terms of the flame temperature–particle velocities available as shown in Fig. 4(b), which has been adapted from Ang and Berndt, 2014 [53].

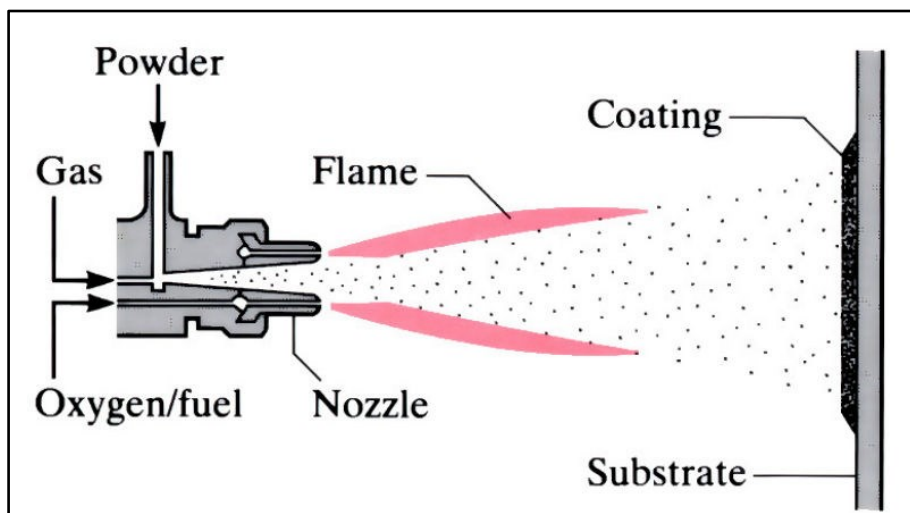


**Figure 4 (a).** Schematic diagram of flame spraying.<sup>1</sup>

<sup>1</sup> Adapted from <https://www.open.edu/openlearn/science-maths-technology/engineering-technology/manupedia/thermal-spraying-hardfacing>

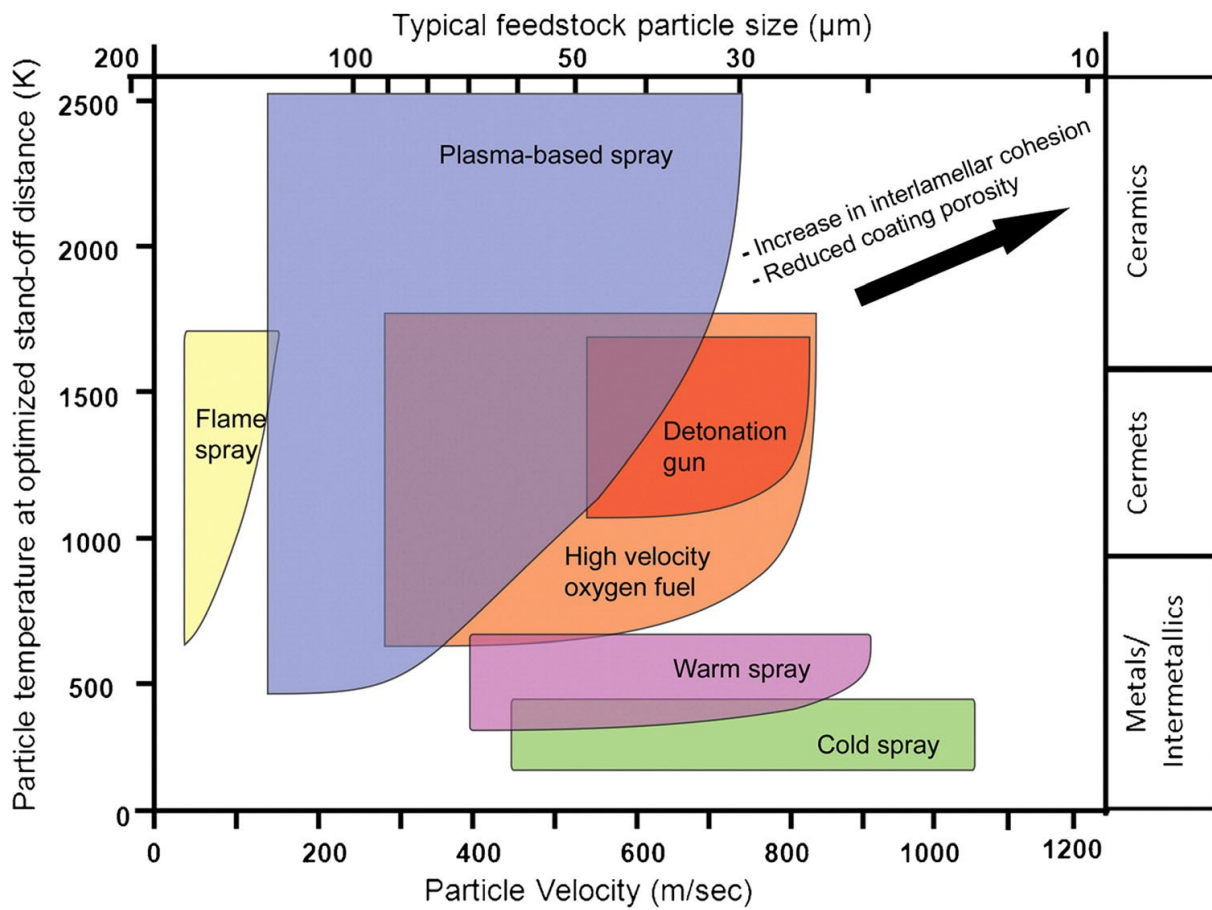


**Figure 4 (b).** Graphical representation of the wide range of particle velocity and flame temperature available for thermal spraying. Adapted from Ang and Berndt, 2014 [53].

TS technology has seen developments in feedstock materials with the exact choice depending on the final application. The surge in harsh industrial conditions has pushed materials research toward the development of novel alloys, like HEAs. HEA coatings have been synthesized using plasma spray (atmospheric and vacuum), high-velocity arc spray, HVOF, warm spray, and cold spray. The adoption of HEA feedstocks has resulted in the development of coatings having superior performances. The following studies provide a glimpse of the progress in the field of thermal sprayed HEAs.

The first TS HEA coatings using APS were reported by Huang *et al.* [21] who prepared the AlCrFeMo<sub>0.5</sub>NiSiTi and AlCoCrFeMo<sub>0.5</sub>NiSiTi coatings which showed significant hardening at high temperatures approximately around 925 HV after heat treatment for 1 hour [40,54] AlCoCrFeNiTi coating with an outstanding bond strength higher than 50.3±8.5Mpa and an average microhardness of the as-sprayed coating of 642 HV (approximately four times that of the 316 stainless steel -173 HV) were prepared by Tian *et al.* [33] using atmospheric plasma spray.

The use of HEAs as a potential alternative to traditional McrAlY bond coats has been studied by Hsu *et al.* [55] who prepared AlSi<sub>0.2</sub>Ti<sub>0.2</sub>CrFe<sub>0.2</sub>Co<sub>0.6</sub>Ni<sub>0.2</sub> HEA overlay coating using both APS and HVOF which had comparable hardness. However, the observed values of hardness 450 and 429 HV respectively for the APS and HVOF coatings are much higher than those observed for CoNiCrAlY-based coatings, which could imply better wear resistance for the HEA coatings. Lobel *et al.*[56] performed ball on disk and oscillating wear test on HVOF AlTiCrFeCoNi coatings which outperformed the hard chrome plated samples. HVOF Al<sub>30</sub>Si<sub>2</sub>Cr<sub>23</sub>Co<sub>22</sub>Ni<sub>23</sub> coatings studied by Bhattacharya *et al.* [182] have demonstrated excellent oxidation resistance as required for aerospace applications. Vallimanalan *et al.* [57] have analyzed the corrosion behaviour of HVOF-sprayed AlCrCoNiMo HEA coatings and compared it with a conventional NiCrSiB-based HVOF coating. Corrosion rate calculation using a Tafel plot demonstrated a lower corrosion rate (0.00276 mm/year) for the HEA coating compared to NiCrSiB coating (0.018 mm/year), thus concluding higher corrosion resistance for this particular HEA coating.

Nair *et al.* [151] compared the wear and corrosion properties of novel equimolar AlCoCrFeMo HEA alloy coatings made by flame spray and cold spray techniques. The microstructure and phases formed in the flame and cold sprayed coatings showed a significant difference. The flame sprayed coatings showed the presence of both oxides and BCC phases whereas the cold sprayed coatings had only BCC phases. The FS coatings showed a higher average hardness value of  $5.78 \pm 0.45$  GPa as compared to the cold sprayed coatings which had an average hardness of  $3.6 \pm 0.45$  GPa. They had claimed that the presence of oxides in the flame spray coatings might be responsible for the higher hardness. The dry abrasive wear tests echoed the hardness trend. However, the cold spray coatings had a lower corrosion rate due to the low porosity and lack of oxides compared to the flame spray coatings. Their work is suggestive of the influence of microstructure on the mechanical properties of the coatings.

The review study by Meghwal *et al.* [54] on thermal spray HEA coatings indicates that HVOF TS coatings have the highest average hardness amongst all other TS processes. The reason for this high hardness has been attributed to super-saturated solid solution strengthening, precipitation hardening and other mechanisms induced due to the processing technique. The present literature available on the wear properties of TS HEA suggests that the APS HEA coatings have better performance than HVOF and CS HEA. However, the commercial validity of TS HEA is yet to be validated due to the lack of high-temperature wear data. TS HEA coatings have not yet been extensively explored for their corrosive behaviour as compared to laser cladded coatings. Although the feasibility of producing HEA coatings by TS technology has been proven to be economically viable the present literature available suggests that the primary focus of TS HEA has been on the development of wear and oxidation-resistant coatings for high-temperature applications. Very few

studies have explored the corrosion, fatigue, creep, fracture toughness and tensile properties of TS HEA [54].

*To the best knowledge of the candidate, there have been no studies exploring the physical properties of TS HEA coatings for functional application. Thus, the unique aspect of this research project lies in exploring the physical property of TS HEA coatings and their potential applicability as multi-functional coatings.*

#### **1.4. Thermal Sprayed Coatings for Resistive Heating Applications**

Electric resistance heating systems have been used successfully employed in power-line de-icing [58], cementitious composites for removal of snow from the surface of transportation infrastructures [59], carbon fibre resistance heating for mitigation of ice accumulation on road surfaces [60], and anti-icing and de-icing of wind turbines [61] and pipelines to avoid freezing [179]. Mostly electrical heat tracers have been used for this purpose. Electric resistive heating systems based on the use of multi-layered thermally sprayed coatings have been proposed as an alternative to electrical heat tracers by Rezvani-Rad [62].

Thermal-sprayed coatings for different heating applications, substrate geometries and materials, and temperature ranges [63-68] have been investigated extensively. With the direct deposition of the films atop the test surface, as opposed to mechanically attaching the heater to the surface, the

thermal contact resistance between the thermal-sprayed heating element and the substrate is minimized. This results in the fabrication of more efficient heating elements. The structure of the heating system depends on the electrical resistance of the metallic alloy that is required to be achieved, the substrate material and its electrical conductivity. Owing to the high thickness required to achieve the appropriate electrical resistance, thermal spraying techniques are preferred over vapour deposition for the fabrication of the coating-based heating elements [63]. The application of thermal-sprayed coatings in electronics was first proposed almost five decades ago when planar ferrite microwave integrated circuits (MICs) were successfully fabricated by using the arc-plasma spraying (APS) process by Harris *et al.* [69]. The works of Smyth and Anderson [70] have suggested that APS can be used for cost-effective production of resistors and conductors with satisfactory long-term stability [70].

The fabrication of meso-electronics by thermal spray techniques was studied by Sampath, *et al.* [71], who reported that multilayer deposits of ceramics and metals having appropriate electrical properties can be produced by thermal spray methods to fabricate electrical components ranging from insulators, conductors, and resistors. They fabricated a NiCr resistor over alumina by plasma or HVOF processes having a sheet resistance in the range of 17-54 K $\Omega$ /sq. They concluded that the low cost, high production rate, capability of producing millimetre-thick layers of conductors and insulators and the flexibility of TS would make this process an alternative for the fabrication of components for power electronics. High-quality dielectrics and conductors have also been produced using cold spray techniques [71].

Deposition of several different thermal-sprayed metal alloys, namely Molybdenum (Mo), nickel (Ni), nickel-20 wt.% chromium (Ni-20Cr), nickel-5 wt.% aluminium (Ni-5Al), iron-13 wt.% chromium (Fe-13Cr), and Iron-chromium-aluminium (FeCrAl), by using various thermal spraying processes including APS, VPS, HVOF, wire arc, combustion spray, and wire flame spray, has been reported in the literature for usage as the heating elements [63-65, 67, 72-74].

Younis *et al.* [180] fabricated a metal film resistance heater of molybdenum by APS that was able to generate heat fluxes up to 7.2 MW/m<sup>2</sup> over an area of 10.3 cm<sup>2</sup> thus, showing that thermal-sprayed coatings can be used as heating systems. Following this Michels *et al.* developed resistive heating Ni-20Cr coatings on dielectric alumina using VPS and HVOF which showed considerable improvement in performance with flux generated up to 17 MW/m<sup>2</sup>. However, the heaters failed at very high-level electrical currents due to the delamination of the Ni-Cr layer from the insulating ceramic layer because of high thermal stresses generated between the deposited ceramic and metallic films due to the mismatch between the thermal expansion coefficients [180].

Tong, *et al.* [72] investigated the fabrication of microheaters by combining thermal spray, as an additive manufacturing process, with micromachining, as a subtractive manufacturing process, to produce functional microheaters. This technique has shown considerable potential in fabricating small-scale embedded functional parts within thermal-sprayed coatings.

Killinger *et al.* [64] deposited nickel-chromium (Ni20Cr) coating onto the alumina coating by plasma spraying process and using the spraying mask technique to form the metal-ceramic multilayer composite that is required for fabrication of the heating devices and studied their

properties. The thickness of the alumina and NiCr coatings were measured to be 200 and 30-50  $\mu\text{m}$ , respectively. It was observed that NiCr coatings having a thickness greater than 50  $\mu\text{m}$  tended to delaminate because of the high residual tensile stresses.

Prudenziati *et al.* [73], developed self-regulated heaters for both planar and cylindrical geometries by air plasma spraying process that showed reliable performance up to 600 °C over long periods and can be used for application in the field of high-temperature operating sensors.

Lopera-Valle and McDonald [75] proposed the use of novel flame-sprayed coatings for the elimination of the formation of ice on wind turbine blades. They found out in their study that the flame spraying process could be used to deposit NiCr and NiCrAlY coatings on FRCP substrates without any damage to the substrate. A layer of garnet sand was used as an intermediary layer between the FRCP and metallic coating to prevent damage to the fibres of the composite during the high-temperature deposition process as well as increase the roughness of the substrate to promote adhesion [75]. Their subsequent work showed that the embedded coating-based de-icing system was able to melt the ice that was formed on top of the coated polymer-based composite when the specimens were exposed to forced convection conditions.

Milad *et al.* [76] fabricated multi-layered coating-based heating systems based on Ni-20Cr and Ni-50Cr on carbon steel pipes for de-icing and anti-icing purposes by various thermal spraying techniques, namely flame spraying, suspension plasma spraying, high-velocity oxy-fuel spraying and air plasma spraying. The development of a multi-layered coating system that consists of two main elements, namely the heating element which is usually a metallic alloy and an electrically insulating ceramic layer or dielectric like  $\text{Al}_2\text{O}_3$  is required to prevent short-circuiting and leakage

current in the heating system made of an electrically conductive substrate. They observed that only 20 watts was adequate to heat almost 600 cm<sup>3</sup> of ice from -20°C to 0°C and, more importantly, melt it when the pipe was directly exposed to the cold air at -25°C. They observed a notable relative difference in electrical resistivity of 68% in the case of flame-sprayed Ni-20Cr coatings fabricated using different spraying parameters. *They thereby concluded that the microstructure of flame sprayed heating elements can be engineered according to the required power output and environmental conditions.*

Dehaghani *et al.* [77] introduced another novel metal matrix composite (MMC) coating-based heating system to solve the issue of ice accretion on wind turbine blades and aircraft wings operating in a cold environment. They used a NiCrAlY metal matrix with different ceramic and cermet reinforcing phases to produce the electrical heating elements using thermal spray techniques and the effect of ceramic particle reinforcement on microstructure, electrical properties and heating performance was studied. They observed that the electrical properties of the heating elements were significantly dependent on the ceramic reinforcing phase. The coatings having higher electrical resistance exhibited better heating performance. Given that the amount of supplied power was equal for all the heating systems, it was concluded that certain MMC heating elements could be effectively employed for the reduction of requisite energy consumption for de-icing.

Bobzin *et al.* developed a heating coating system of TiO<sub>x</sub>/Cr<sub>2</sub>O<sub>3</sub> for their potential use in mould tempering in injection moulding. The coatings were found to endure up to 10,000 thermal cycles between 60°C to 150°C without degeneration and showed homogeneous surface temperature

distributions. A following work by the same research group developed a multi-layer coating system for measurement of the temperature of the injection moulding tool surface by utilising the temperature-sensitive semiconducting  $\text{TiO}_x/\text{Cr}_2\text{O}_3$  coating between two isolated  $\text{Al}_2\text{O}_3$  and electrically contacted with NiCr coatings outside the isolation coatings. They concluded that  $\text{TiO}_x/\text{Cr}_2\text{O}_3$  can be employed as a functional coating for temperature sensing by monitoring its resistivity [78]. A recent work pursued by the same research group explored the feasibility of HEA as thermal spray heating elements. They explored the electrical properties of melt-spun tape of thirteen different compositions of  $\text{Al}_{0.5}\text{CoCrFeNiZr}_x\text{Si}_y$ . They observed that the addition of Zr to the popularly investigated  $\text{Al}_{0.5}\text{CoCrFeNi}$  alloy increases the resistivity. Although the addition of Si has no considerable effect on resistivity it has good phase stability up to 600 °C. They have proposed that  $\text{Al}_{0.5}\text{CoCrFeNiZr}_{0.2}\text{Si}_{0.2}$  HEA with high electrical resistivity and phase stability up to 600 °C could be a potential alternative to current heating elements (ITSC Conference Paper) [79].

## **1.5. Rationale behind the designing of the novel HEA compositions used in the study**

HEAs mainly include two categories of elements: 1). Refractory elements like V, Cr, Ti, Mo, Nb, Ta, W, Zr, and Hf) and 2) Commodity metals such as Cr, Co, Fe, Ni, Mn, and Cu [124]. The HEAs comprised of the elements of the first category often formed refractory alloys mostly having a BCC structure [125, 126] and are popularly referred to as Refractory High Entropy Alloys (RHEAs) [127]. On the other hand the second category of elements forms either FCC [128,129], BCC [130,131] , or a combination of both [132-134]. Although the FCC-based HEAs have

excellent ductility and plasticity they lack considerable yield strength and require thermomechanical treatment before practical industrial applications resulting in increased cost [135,136]. In contrast, the BCC HEAs inherently have relatively high intrinsic yield strength because of the limited number of active slip systems [137-138]. Moreover, the BCC RHEAs have excellent high-temperature mechanical properties [139-141]. For instance, the AlCrFeCoNi HEA with a single-phase BCC solid solution exhibits excellent compressive properties of yield stress 1250.96 MPa and plastic strain 32.7% [131]. VNbMoTa RHEAs exhibit excellent room-temperature ductility with a fracture strain > 25% and high-temperature strength compressive yield strength of 811 MPa at 1000°C [142].

Since BCC HEAs have high strength and are prospective materials for use in a high-temperature application the purpose was to design an alloy which primarily forms BCC structures. Adapted from the extensively studied AlCoCrFeNi HEA family the novel AlCoCrFeMo HEA composition had been chosen. It has been observed that the addition of Al in addition to Fe and Cr promotes the formation of BCC phases [143,178]. Molybdenum (Mo) replacement of nickel (Ni) was introduced in this study to understand its effect on phase formations and mechanical properties. Mo increases the hardening rate along with Co and Fe, which may be beneficial for improving wear resistance. Furthermore, Mo may also result in improved corrosion performance in terms of passivation resistance and pitting resistance of the HEAs [144].

Soni *et al.* [145], have claimed that adding W increases the relative amount of BCC solid solution responsible for grain refinement and strengthening, resulting in the enhanced compressive strength and Vickers microhardness of FeCoCrMnW<sub>x</sub> high entropy alloys. Similar conclusions were drawn

by Dong and Lu [146] in their investigation of the effect of W addition on Near-Eutectic AlCoCrFeNi<sub>2</sub> High-Entropy Alloy. Malatji *et al.* [147] have studied the microstructural, mechanical and electrochemical properties of AlCrFeCuNiW<sub>x</sub> high entropy alloys and found that the increase in W content results in higher plasticity at maximum compressive strength and showed better wear and corrosion performance. Binglun Yin *et al.* [148] proposed that V can be the prime element for strengthening HEAs, and HEAs containing V have higher strengths than their counterparts without V.

This study aimed to develop novel AlCoCrFeMo, AlCoCrFeMoW and AlCoCrFeMoV HEA compositions to understand how tungsten (W) and vanadium (V) additions in AlCoCrFeMo influence the evolution of microstructures, phase formations, microhardness, electrical resistivity and erosion performance. The addition of W and V creates lattice distortions and stabilization of BCC phases along with other elements such as Al, Co, Cr, Fe, and Mo, which may improve the electrical resistivity and erosion resistance of the compositions.

## 1.6. Solid Particle Erosion

Solid particle erosion (SPE) refers to the removal of material from component surfaces due to the successive impact of hard particles travelling at substantial velocities [80]. Material removal due to solid particle erosion is a consequence of a series of essentially independent but similar impact

events with the contact between the hard particles and the component surface being of very short duration. From an independent repeated impact point of view, SPE is completely different from the other closely related processes like sliding wear, abrasion, grinding and machining where the contact between the tool/abrasive and the target/work-piece is continuous [80].

This type of erosion is a typical wear mode that negatively impacts the longevity of parts in many industries like aerospace, marine, mining, wind energy, and oil and gas industries [80-83]. Figure 5 shows a graphical representation of the different industries affected by SPE and some eroded components. Thus, improving the erosion resistance is economically important. Different industries have explored different methodologies to deal with SPE like, the development of blade materials and the design of anti-solid particle steam passage in steam turbines [83, 84]; the use of filters and inertial particle separators in case of jet engines [81] or screens and gravels packs in the oil and gas industries [82]. However, most of these methods are not very efficacious.

One of the solutions to effectively combat SPE lies in the use of protective coatings which can improve the lifetime of the component without adding significant weight. Although research into SPE of surfaces has been ongoing for more than 60 years the protection of components by surface treatment technologies started somewhere in the late 1980s following aircraft reliability problems during military operations in sandy environments [85]. The advantage of coatings is that they are relatively cheap and can be applied in situ. Choosing the best coating process of all the different deposition techniques available depends on the functional requirements, adaptability of the coating material to the technique intended, the desired level of adhesion (size, shape, and metallurgy of the substrate), availability and cost of manufacturing. In general, widely used techniques to obtain

coatings include weld overlay, diffusion coatings, CVD/PVD coatings, thermal spraying and laser cladding.

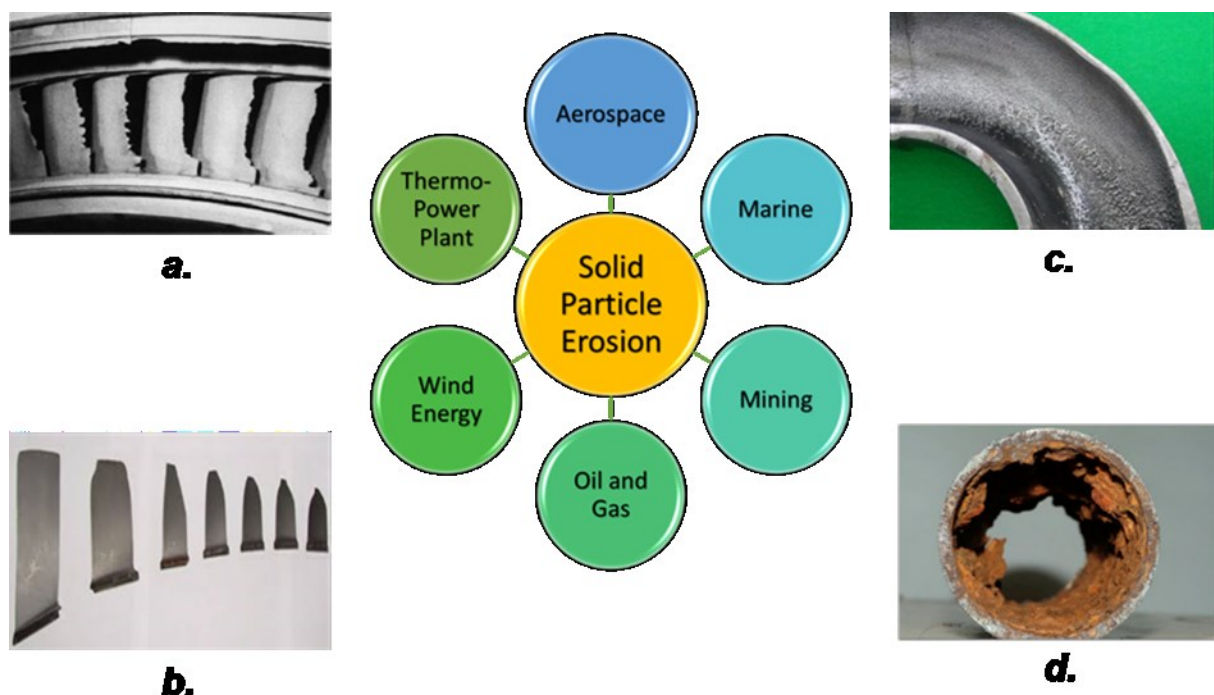


**Figure 5.** Shows the different industries which incur substantial losses due to the damaging effect of solid particle erosion. The pictures in the inset show some of the degraded components a). Eroded turbine blades, b). The progressive change in shape of turbine blade because of erosion, c). Cross-sectional image of a pipe that has been subjected to solid particle erosion, d). Erosion-Corrosion of pipe

Hard protective coatings like carbon-based films or TiN films have been widely investigated for wear, abrasion and erosion protection. The carbon-based films are predominantly thick diamond coatings deposited by chemical vapour deposition. Although they have very high hardness and are extremely resistant to SPE it is difficult to implement them in practice as they require high deposition temperatures which exceed the permissible limits of metallic components [86,87]. Hence, TiN-based in monolithic or multilayer forms that can be deposited on relevant substrates are usually used [88]. TiAlN is one such industrially implemented system that has great SPE and good high-temperature stability [89,90].

Bousser *et al.* studied the [88] material loss mechanisms of monolithic coatings subjected to solid particle erosion (SPE) using angular alumina particles with velocities below 100 m/s. They have co-related the erosion rate with the hardness of the substrate and found strong dependence. They have concluded that as the hardness of the surface increases and the amount of material displaced decreases a significantly larger number of impacts are needed for material removal leading to the very strong dependence of erosion rates on target hardness.

However, CVP/PVD and diffusion coatings are thin and cannot be produced on-site or repaired. In comparison, thermal sprayed coatings do not require the base metal to be heated to high temperatures which would impair the mechanical or microstructural properties. In the case of weld overlays a concerning factor is the repeated weld overlay application to the same tube area that may result in embrittlement of the old overlay and cracking. The aforementioned shortcomings in diffusion and weld overlay coatings have focused significant attention on thermal sprayed coatings for protection against erosion [91-94].

Branco *et al.* [95] investigated the room temperature solid particle erosion of plasma sprayed zirconia and alumina-based ceramic coatings, with different levels of porosity and varying microstructure and mechanical properties at an impact angle of 90°. They observed that the results cannot be explained by the current erosion models which were based on hardness alone and, that there is a strong relationship between the erosion rate and the porosity which needs to be incorporated in erosion wear modelling.

Kulu *et al.* [96] studied a variety of cost-effective self-fusing (or self-fluxing) alloys of MCrBSi composites, containing tungsten carbide–cobalt (WC–Co) based hard metals powders applied by spray and fusion methods for application as wear, corrosion and erosion resistant materials. The fused composite coatings of MCrBSi compositions, where M stands for either Ni, Co or Fe, can be fused by heating up to a temperature of 1050 °C. They have low porosity and a high bonding with the base material and can resist significant impact loads. They found that the erosion rate is strongly influenced by the impact angle and microstructure with little or no dependence on hardness and was 5-6 times higher at higher temperatures. However, the erosion rate at higher temperatures was not influenced by the impact angle [96].

Ramesh *et al.* [94] studied the SPE of HVOF sprayed WC-Co/NiCrFeSiB coatings on GrA1 boiler tube steel with a high hardness value of 1223 HV. The high hardness was attributed to the high cohesive strength and low average porosity (0.5%) of the HVOF coatings. The erosion resistance of WC-Co/NiCrFeSiB coating featured composite ductile and brittle modes of material removal, with a dominant brittle mode. Craters, grooves, lips and platelet formation and carbide particle pull-out comprised the erosion mechanism [94].

Krishnamurty *et al.* [97] observed the SPE behaviour of plasma sprayed alumina and calcia-stabilized zirconia coatings on Al-6061 substrate. The erosion results were well correlated with the microstructural and subsequent mechanical property change. They found that erosion of coating systems occurred through spalling of lamella exposed on the coating surface that resulted from cracking along the lamellar interface. The material removal may occur from the displaced material forming lips around the indentations as a result of the repeated impact of erodents. Higher volume erosion was seen at a 45° angle of impact and the failure behaviour was in between ductile and brittle.

Ashrafizadeh *et al.* [98] studied the effect of working temperature on SPE performance of Polyurethane (PU) elastomer. They found that the erosion rate improved at 60 °C for two of the studied elastomers due to an improved ability of the material to regain its initial deformation however it increased at 100 °C. Although no simple relation was observed between the elongation at break and the erosion rate, it was evident that the elongation at break affects the wear performance and the morphology of worn surfaces [98].

Recently, Bhosale *et al.* [99] used an air-jet erosion tester based on the ASTM G76 standard to compare the APS and HVOF WC-Cr<sub>3</sub>C<sub>2</sub>-Ni coatings to explore their applicability as coatings on boiler tubes, steam and gas turbines to prevent high-temperature erosion. The erosion resistance was 2-3 times better than the uncoated 316L stainless steel specimen at higher temperatures and impact angles of 30° and 90°. Both coatings exhibited a mixed mode of material removal with the HVOF coating offering higher erosion resistance than the APS coating because of its lower porosity, greater splat adhesion, a lower degree of decarburisation and higher inter-splat sintering

at elevated temperatures. This work suggests that the resultant microstructure because of the difference in processing technology has a marked influence on the performance.

High ductility along with superior erosion resistance compared to conventional wear-resistant coatings was reported by Vallimalan *et al.* [100], in their study of the slurry erosion characteristic of HVOF AlCoCrMoNi high entropy alloy coating using a water jet erosion tester at varying jet velocity and angular impingement. Although the increase in velocity of slurry increases the volume loss in each coating, the performance of HEA is much better than NiCrSiB and almost similar to WC-CoCr coating. Both the conventional coatings and developed HEA coating show a trend following a minimum mass loss at a lower angle ( $30^\circ$ ) and maximum mass loss at a higher angle ( $90^\circ$ ) of impingement [100].

Kumar *et al.* [101] synthesized  $\text{Al}_x\text{Fe}_{1.5}\text{CrMnNi}_{0.5}$  ( $x = 0.3, 0.5$ ) HEA by ball milling and reported the air jet erosion behaviour of the sintered alloy at different impingement angles. The erosion value is less for the samples sintered in air because of high hardness and higher aluminium of 0.5. The erosion results indicated that the erosion rate is maximum in all sintered HEAs at lower impact angles (45 deg). This is due to the shear-type plastic deformation which in turn is the result of the sliding action of the erodent particles, and is generally observed in the ductile mode of erosion [101].

Lv *et al.* [102] studied the effect of WC addition on the slurry erosion behaviour of HVOF sprayed AlCoCrFeNi HEA coatings composed of mixed FCC and BCC phases and having a porosity less than 1%. They observed that the microhardness was positively correlated with the WC content and

the volume loss and rate of volume loss of coatings decreased with an increase in WC content. The coatings underwent a ductile mode of failure with some under-layer peeling. Although the WC protected the HEA/WC coatings by the second phase strengthening there was a gradual brittle detachment of WC particles at high grazing impact angles causing erosion [102].

Zhang *et al.* [103], studied the microstructure and high-temperature solid particle erosion behaviour of laser cladded CoCrFeNiSi HEA coatings at different impact angles and compared them with Stellite-6 (wt%) Co-based alloy. An FCC structure with a hardness value of 580 HV was reported for the HEA. The HEA coating showed comparatively lower erosion rates than Co-based alloy coating under all test conditions (impact angles of 30°, 60° and 90° and temperatures of 20, 500, 600 and 700 °C). It has been claimed that a dense and continuous oxidation film could form on HEA coating at 700°C which may have been responsible for the protection of the coating from erosion at high temperatures to some extent [103].

Kim *et al.* [104] studied the mechanical and electrical properties of NbMoTaW refractory HEA thin film deposited by magnetron sputtering. The films studied by them had a single phases BCC solid solution with an average grain size of 15 nm along with a high hardness of 12 GPa and electrical resistivity of 168  $\mu\Omega$  cm because of the nanoscale grains and severe lattice distortion. The nanoscale grains and severe lattice distortion of these films resulting in the high electrical resistivity and hardness make them favourable for use as hard coatings in protective layers and as electrical resistors in nanofabricated devices.

### **Choice of sand as the erodent medium**

The primary erodent in the oil and gas industry is sand [149]. Moreover, the erosion in power plants is a result of the impact of particulates, such as coal ash, dolomite and unburned carbon particles on the surface of heated boiler tubes. It is generally believed that the most erosive species in the fly ash are quartz, (a crystalline form of  $\text{SiO}_2$ ) and mullite [92,94]. Thus, sand is often chosen as the erodent being one of the main constituents of fly volcanic ashes [150]

The ratio of hardness to elastic modulus is an appropriate parameter as far as the correlation with the erosive wear rate of the coating is concerned. Santana *et al.* [105] explored the influence of mechanical properties of tungsten carbide–cobalt HVOF thermal spray coatings on their solid particle erosion behaviour. Under the given experimental conditions WC–10Co–4Cr coating exhibited a higher erosive wear resistance as compared to the WC–12Co coating. They concluded that as the ratio of hardness to elastic modulus increased, in the case of WC–10Co–4Cr the erosive wear rate of the coating due to the impact of small SiC particles decreased. Thus, the WC–10Co–4Cr coating, with a higher hardness to elastic modulus ratio, exhibits a smaller erosive wear rate than the WC–12Co coating. As such as the hardness to elastic modulus ratio increases, the erosive wear rate of the coating due to the impact of small SiC particles decreases [105].

## **1.7. The Hardness to Elastic Modulus ( $H/E$ ) Ratio and its relevance in wear and erosion**

Hardness is a measure of the resistance to localized plastic deformation induced by either mechanical indentation or abrasion. There are three main ways of measuring hardness namely, scratch, indentation and rebound. Values can be converted from one scale to the other with the help of available conversion tables.

The elastic modulus (also known as modulus of elasticity) is the unit of measurement of an object's or substance's resistance to being deformed elastically (i.e., non-permanently) when a stress is applied to it. The elastic modulus of an object is defined as the slope of its stress–strain curve in the elastic deformation region. Stiffer the material higher is the elastic modulus. The three primary types of elastic modulus includes the Young's Modulus (E), Shear Modulus (G) and Bulk Modulus (K). A stiffer material will have a higher elastic modulus.

### **Nanoindentation technique to determine the Nanohardness and Young's Modulus**

The indentation test is a simple and effective method to evaluate the mechanical properties of materials like the hardness and elastic modulus, by driving an indenter into the material surface and subsequently imaging the impression [118]. Indentation tests were primarily used for the measurement of hardness. A hard object having a certain shape and size is used as an indenter and indented into the test material under certain pressure holding for a while before unloading. The hardness of the tested material can be determined from the relationship between the total indentation load and displacement or area. The traditional methods of hardness testing, such as the

Vickers hardness method (Vickers), Knoop hardness method (Knoop), and Rockwell hardness method (Rockwell) operate on this principle [119].

With the development of nanotechnology, nanoindentation emerged as the most common technique to investigate the mechanical properties of nanomaterials. The nanoindentation method, also known as the ‘Depth Sensing Indentation Technique’ was first proposed and developed by Oliver and his Coworkers [120]. In this method, a nanometer-sized hard tip or nanoindenter is pressed into a sample by applying a small force. Young's modulus and hardness—resistance to permanent or plastic deformation—of the sample is measured from the test. The analysis of the loading-unloading curve also gives information about viscoelasticity, creeping, fracture toughness, strain-hardening effect, residual stress, phase transition, and dislocation movement in addition to Young's Modulus and Hardness.

At the submicron scale, nanoindentation has provided insights into a broad range of material properties. Weppelmann and his co-workers [121] used this technique to study the indentation cracking of brittle thin films on brittle substrates. Fracture toughness, adhesion and mechanical properties of dielectric thin films by nanoindentation were studied by Volinsky, Vella and Gerberich in 2003 [122]. Yang *et al.* 2006 [123] worked on strain hardening and recovery in a bulk metallic glass under nanoindentation

### **Hardness to Elastic Modulus ( $H/E$ ) Ratio**

An important trend in coating research for several years has focused on the development of super-hard coatings to prevent wear and erosion. This rationale for super-hard coatings was based on the

Archard wear model wherein the wear volume was found to be inversely proportional to the hardness of the softer material in a sliding/adhesive contact. However, super-hard coatings are usually susceptible to brittle fracture. Matthews, Leyland and co-workers have determined that in many practical wear situations hardness alone is not particularly an effective predictor of wear resistance [106-109]. They found that the abrasive wear resistance of 5–19 at.% C-doped W coatings varied with coating hardness and was least at an optimal hardness of 15-20 GPa after which the wear rate increased with increasing hardness.

Matching the elastic modulus of the coating with the substrate would result in similar strain thus minimising the coating/substrate interfacial stress distribution under applied load. This will allow the coating to deflect without cracking or debonding. The improved ability of the coating to accommodate substrate strain can be a significantly more important factor in wear/erosion resistance than extremely high hardness [110].

Leyland and Matthews have proposed the ratio of coating hardness (H) to coating elastic modulus (E),  $H/E$ , as an indicator of coating durability as this parameter is a measure of the elastic-strain-to-break and coating resilience and is strongly correlated with energy dissipation in mechanical contact [106, 107, 111].

A high  $H/E$  ratio can have a strong influence on wear resistance in more tribologically complex loading situations, such as sliding/abrasion or impact/erosion. The  $H/E$  and  $H^3/E^2$  ratios have been considered as potential indicators of coating fracture resistance. Strong correlation between  $H/E$  and surface cracking in the indentation and bending of various oxide and nitride coatings

have been reported by Musil and co-workers [112, 113]. Coatings with very high  $H^3/E^2$  have also shown enhanced resistance to erosion, e.g., when eroded by 50  $\mu\text{m}$  alumina [114-116], or 40–100  $\mu\text{m}$  silicon carbide erodent [117].

*Thus, it is understood that hardness is not the only criterion for predicting coating wear, the ratio of hardness to modulus  $H/E$  which is related to elastic strain to failure and fracture toughness has been proposed as one of the key parameters controlling wear and erosion*

*It is well evident from sections 1.5 and 1.6 that the erosion rate can be influenced by the impact angle and temperature besides other factors like impact particle velocity, size and shape and flow rate [80]. Also, there exists a correlation between mechanical properties like hardness, elastic modulus, and the rate of erosion [88, 98]. Different types of trends in erosion rates have been observed in the case of different material systems processed in different ways. There is no one way to generalize the observed behaviour because of the complex nature of the process. Moreover, the commonly explored erosion resistance materials include WC- Co-based systems or composites or TiN systems. Very few studies have delved into exploring the solid particle erosion properties of flame-sprayed high entropy alloys. Hence, this study investing the erosion mechanism, and the relation between the hardness, elastic modulus and erosion rates of FS HEA will provide a new understanding of the nature of failure mechanisms of HEA.*

## **1.8. Objectives**

1. To **develop** novel AlCoCrFeMo, AlCoCrFeMoW and AlCoCrFeMoV HEA compositions using flame spray technique.
2. To **understand** how tungsten (W) and vanadium (V) additions in AlCoCrFeMo influence the evolution of microstructures, phase formations, microhardness, and electrical resistivity and solid particle erosion performance.
3. To **explore** the potential use of these alloys as **heating elements**.
4. To **assess** the behavior of the HEA coatings to solid particle erosion (SPE) at varying impact angle and temperature.
5. To **investigate** the relationship between microhardness, elastic modulus and rate of erosion.

## **1.9. Motivation**

The summary of the various research works presented throughout Chapter 1 has proven that this new class of metallic alloys the high entropy alloy has outperformed most conventional alloys. However, their physical properties have not yet been fully explored. The superior properties of the HEA coatings that have been reported and the many other properties that have not yet been pursued have motivated the candidate to explore the new avenue of electrical and heating properties of flame sprayed HEA coatings. During this work, it also came to light that the multifunctional aspects of HEA have not been conceived. It is expected that the erosive wear of heating coatings will result in a change in performance. Thus, getting an estimate of the erosion rate will help in the

development of superior erosion-resistant heating coatings for future applications. The ingenuity of this work essentially lies in the exploration and investigation of the multifaceted aspect of novel flame sprayed High Entropy Alloy coatings.

## **1.10. Thesis Organization**

This thesis manuscript is organized into several chapters. Chapter 1 provides a comprehensive review of the various aspects of this project highlighting the previous results and prospects. Beginning with an introduction and background of HEA, Chapter 1 moves on to highlight the exceptional properties of HEAs. It then discusses the manufacturing of HEA coatings and their applications using different techniques including thermal spray. Following this, the review of the existing literature on TS HEA suggests its feasibility as an efficacious manufacturing technique. The readers are then introduced to functional i.e. resistive heating thermal spray coating and an overview of the progress in this field has been presented. Following this, to explore the possible multi-functional aspect of HEA coatings an introduction to solid particle erosion and the factors influencing the rate of erosion has been presented. A summary of each section has been provided at the end to highlight the most important aspects that have motivated the conceptualization of this work. Chapter 2 describes the experimental procedure used to fabricate and characterize the flame-sprayed HEA coatings. Chapter 3 presents the results and discusses the objectives of this study. Further, Chapter 4 documents the conclusions from this research and finally, Chapter 5 outlines the future work and recommendations.

## Chapter 2: Experimental Methodology

### 2.1. Materials

Customized mechanically alloyed feedstock powders having the nominal composition (at%) of Al<sub>20</sub>Co<sub>20</sub>Cr<sub>20</sub>Fe<sub>20</sub>Mo<sub>20</sub>, Al<sub>16.67</sub>Co<sub>16.67</sub>Cr<sub>16.67</sub>Fe<sub>16.67</sub>Mo<sub>16.67</sub>W<sub>16.67</sub>, and Al<sub>16.67</sub>Co<sub>16.67</sub>Cr<sub>16.67</sub>Fe<sub>16.67</sub>Mo<sub>16.67</sub>V<sub>16.67</sub> manufactured by ABM Nano LLC, Missouri, TX, USA, have been used in this study. The average particle size of the HEAs was estimated from the SEM (Zeiss Sigma 300 VP-FE, Carl Zeiss Canada Ltd., Toronto, ON, Canada) images by using the image analysis technique (ImagePro, Media Cybernetics, Bethesda, MD, USA). At least thirty images of each powder were analyzed. The particle size distribution ( $-d_{90} \pm d_{10}$ ) were found to be  $-30 \pm 2.8 \mu\text{m}$ ,  $-48 \pm 8 \mu\text{m}$ ,  $-55 \pm 10 \mu\text{m}$  for AlCoCrFeMo, AlCoCrFeMoW and AlCoCrFeMoV respectively.

Elemental mapping analyses were performed using energy-dispersive spectroscopy (EDS) to determine the homogenization of powder particles. Figure 6 shows the morphologies of the feedstock powders. The HEA powders exhibited agglomerated and irregular morphologies. This is mostly caused due to the repeated welding, fracturing, and rewelding of powder particles in a high-energy ball mill [151]. Elemental mapping analyses were performed using energy-dispersive spectroscopy (EDS) to determine the homogenization of powder particles. The EDS mapping is shown in Fig. 7. proves that the particles were well homogenized with little or no traces of oxides. Table 1 compares the chemical composition of the HEA powders with the nominal composition. It shows that the chemical composition obtained after mechanical alloying was in near agreement with the nominal composition. The presence of an increased amount of aluminium and a lesser

amount of cobalt in AlCoCrFeMoW and AlCoCrFeMoV compositions could be attributed to manufacturing error.

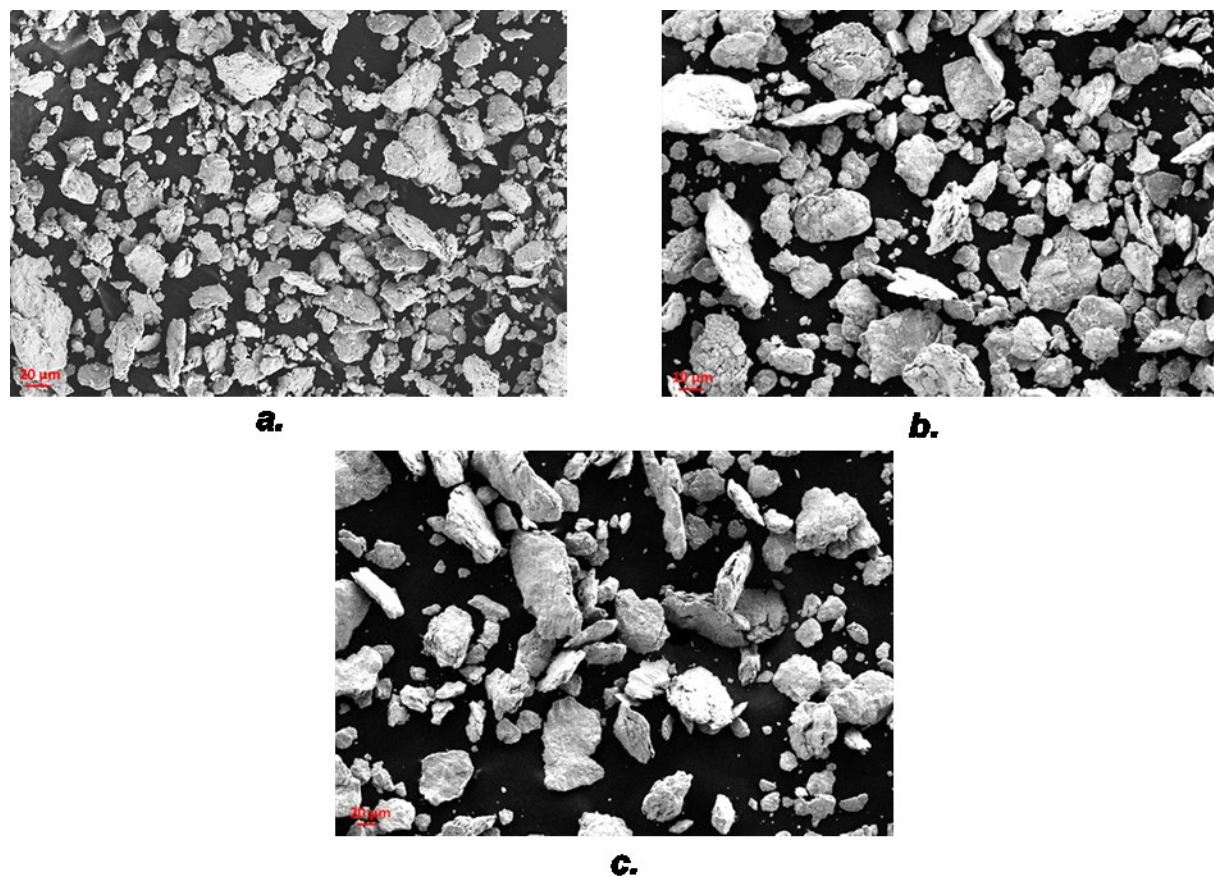
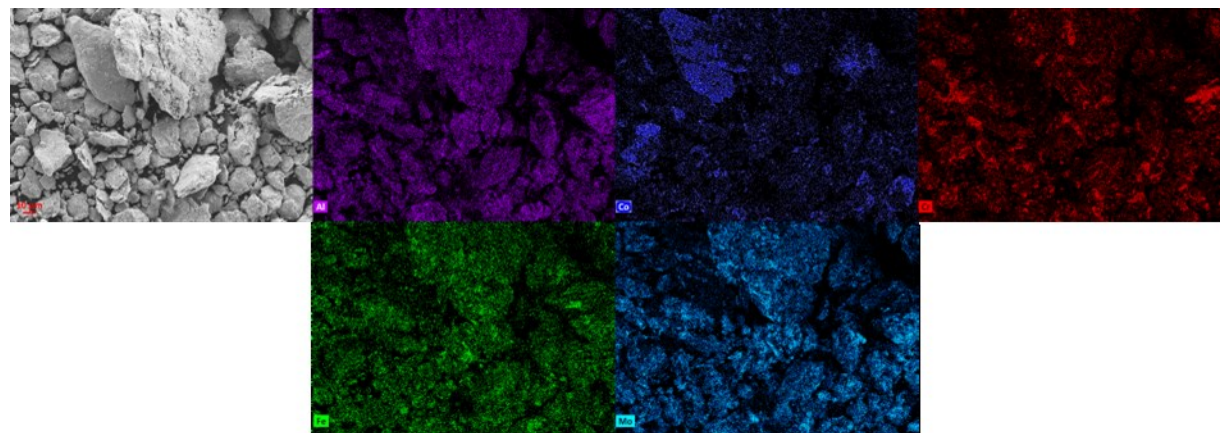
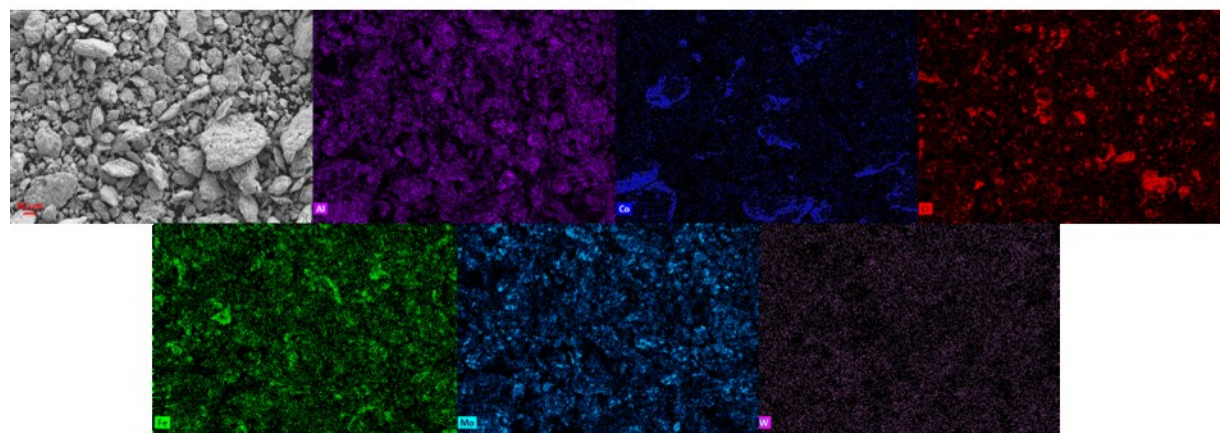


**Figure 6.** SEM images of feedstock powder of a). AlCoCrFeMo, b). AlCoCrFeMoW and c).

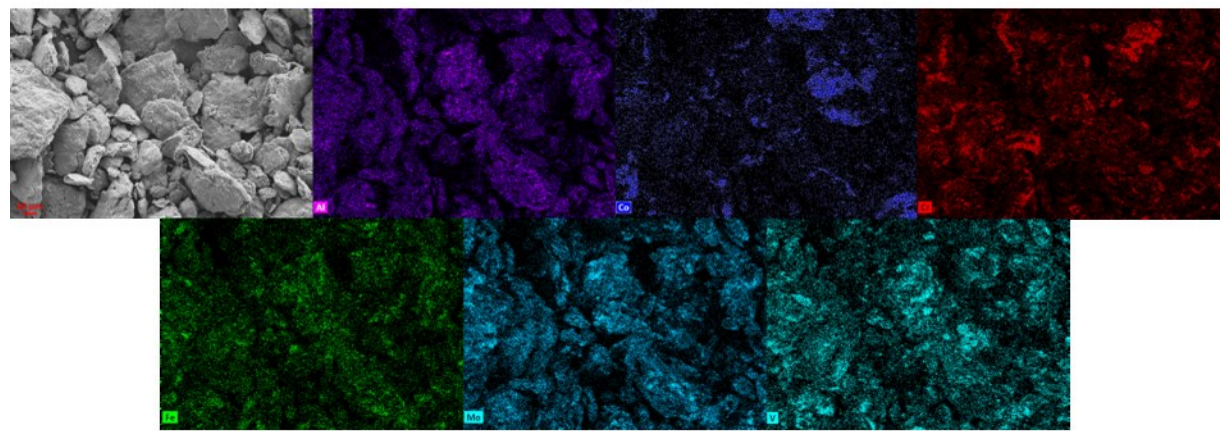
AlCoCrFeMoV



**a.**



**b.**



**c.**

**Figure 7.** EDS Mapping of feedstock powder of a). AlCoCrFeMo, b). AlCoCrFeMoW and c).

AlCoCrFeMoV

**Table 1.** Chemical composition of the HEA powders obtained from EDS in comparison to the nominal composition in atomic percentage.

Element	AlCoCrFeMo Composition (at %)		AlCoCrFeMoW Composition (at %)		AlCoCrFeMoV Composition (at %)	
	Nominal	EDS	Nominal	EDS	Nominal	EDS
<b>Al</b>	20	20.5 ± 2.1	16.67	17.9 ± 1.8	16.67	20.5 ± 1.4
<b>Co</b>	20	19.2 ± 0.9	16.67	11.7 ± 2.5	16.67	12.8 ± 2.5
<b>Cr</b>	20	19.4 ± 0.4	16.67	15.8 ± 1.5	16.67	17.2 ± 0.4
<b>Fe</b>	20	20.4 ± 0.8	16.67	17.6 ± 0.8	16.67	15.2 ± 0.8
<b>Mo</b>	20	20.5 ± 1.1	16.67	22.3 ± 2.3	16.67	17.2 ± 0.7
<b>W</b>	-	-	16.67	13.7 ± 1.9	-	-
<b>V</b>	-	-	-	-	16.67	17.1 ± 0.8

## 2.2. Coating Fabrication

Commercially available stainless steel 316L (Metal Supermarkets, Edmonton, AB, Canada) was used as a substrate in this study. Prior to deposition, the substrates were grit blasted with #24 alumina grit (Manus Abrasive Systems Inc., Edmonton, AB, Canada) to remove impurities and to enhance the roughness of the coatings for better coating adhesion. Pre-alloyed AlCoCrFeMo, AlCoCrFeMoW, and AlCoCrFeMoV HEA feedstocks were deposited on stainless steel 316L substrates using an oxy-acetylene flame spray torch (6PII, Oerlikon Metco, Westbury, NY, USA) equipped with a volumetric powder feeder (5MPE, Oerlikon Metco, Westbury, NY, USA). In order to avoid conductivity and short-circuiting during the Joule heating experiments, an insulating layer of alumina  $-45$  to  $+5 \mu\text{m}$  (AMDRY 6060, Oerlikon Metco, Westbury, NY, USA) was deposited on to the substrates before the deposition of HEA layers. The flame spray torch was

manoeuvred using a fixed robot assembly (HP-20, Motoman Yaskawa Electric Corp, Waukegan, IL, USA) to ensure the consistency and repeatability of deposition. The optimized parameters have been listed in Table 2. For all specimens, two passes of alumina and two passes of the HEAs were performed to produce the coatings. At least three coatings were produced for each test.

**Table 2.** The flame spray parameters used in the study. Note FMR is a relative measure for regulating the flow rate of the powders.

<b>Parameter</b>	<b>Alumina</b>	<b>HEA</b>
	<b>Layer</b>	<b>Layer</b>
Acetylene Flow (NLPM)	20	25
Oxygen Flow (NLPM)	30	30
Argon Flow Rate (m <sup>3</sup> /h)	0.56	0.56
Powder Feed Rate (FMR)	100	100
Standoff Distance (mm)	172	178
Torch Velocity (mm/s)	250	350
Increment (mm)	3	3
No of Passes	2	2

## **2.3. Coating Characterization**

Coating specimens were sectioned cross-sectionally, and cold mounted using epoxy resin (LECO, Mississauga, ON, Canada) to perform microstructural characterization. The cross-sectioned specimens were grounded using silicon carbide grit papers (180 to 1200) (LECO, Mississauga, ON, Canada), followed by polishing using diamond slurries of  $3\text{ }\mu\text{m}$  and  $1\text{ }\mu\text{m}$  (LECO, Mississauga, ON, Canada), respectively. Specimens were cleaned using alcohol and acetone to remove diamond residues before microstructural investigations. The microstructures and chemical compositions of the HEA coatings were analyzed by a scanning electron microscope (SEM) equipped with an energy dispersive spectroscopy (EDS) (SEM, Zeiss Sigma 300 VP-FE, Carl Zeiss Canada Ltd., Toronto, ON, Canada) using a voltage of 15kV. A backscattered (BSE) detector was used to capture the micrographs, which were qualitatively analyzed using image analysis (ImagePro, Media Cybernetics, Bethesda, MD, USA) to evaluate the porosity and thickness. At least ten micrographs were used to determine the average values of porosity and thickness. Phases were determined by X-ray diffraction (XRD) (Ultima IV diffractometer Rigaku, Akishima-Shi, TYO, Japan) using Cu K $\alpha$  radiation ( $\lambda = 1.546\text{ \AA}$ ) scanning from  $20^\circ$  to  $100^\circ$  at a rate of  $2^\circ/\text{min}$ .

## **2.4. Microhardness**

The cross-sectional microhardness of the coatings was measured by a Vickers hardness tester (VH1102 Vickers hardness tester, Buehler Wilson, Lake Bluff, IL, USA) according to ASTM Standard E384 [ASTM]. A load of 300-gram force (gf) was applied for a dwell time of 15 s. At least 30 indents ( $n = 30$ ) were made to ensure repeatability of the results.

## 2.5. Electrical Resistivity and Joule Heating Performance

A custom-designed setup has been used to study the change in electrical resistivity with temperature and the joule heating performance. The schematic diagram of the experimental setup used is shown in Fig. 8. Electrical wires were attached to the coating specimens to ensure current flow through the surface of the coatings. Six K-type thermocouples (T1 to T6) (Twidec 3M K-Type Sensor Probe, Suzhou, Jiangsu, 215008, CN) were employed to record the surface temperature of the coatings and substrates, as shown in the Fig. 8. A direct current (DC) power supply (1902B DC, B&K Precision Corporation, Yorba Linda, CA, USA) with a maximum voltage and current specification of 60 V and 15 A was employed to generate voltage differences within the heating elements. The data to study the temperature dependence of resistance was collected during self-heating of the samples, i.e., recording the values of flowing currents and the corresponding voltage drops across the resistor when operating as a heater.

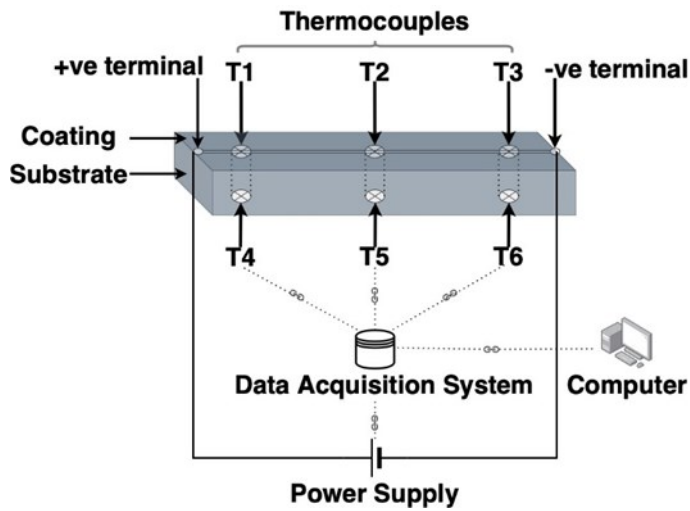


**Figure 8.** Schematic of Joule heating experiment

The specimens were heated from the ambient temperature up to 250°C by applying a voltage between 1 V and 20 V. A data acquisition system (SCXI-1600, National Instruments, Austin, TX, USA) was used to determine the current, voltage and temperature at a frequency of 10 Hz (10 data points per second). Before conducting the tests, the four-point Kelvin connection technique was employed to measure the electrical resistance of all the samples using a digital multimeter (34461A Digital Multimeter, 6 ½ Digit, Keysight Technologies, Mississauga, ON, Canada).

The sample resistance was then calculated from the recorded data using Ohm's law given in equation 1.

$$V = IR \quad (1)$$

where  $V$  is the voltage,  $I$  is the current and  $R$  is the resistance.

The resistivity values were calculated from the recorded resistance values and dimensions of the specimen using equation 2

$$\rho = \frac{R A}{l} \quad (2)$$

Where  $\rho$  is the resistivity,  $R$  is the resistance,  $A$  is the cross-sectional area of current flow (= thickness of the HEA coating), and  $l$  is the length of the specimen (=152 mm).

The temperature coefficient of resistance (TCR) was calculated from the recorded values as per equation 3.

$$TCR = \frac{(R - R_0)}{R_0(T - T_0)} \quad (3)$$

where  $R$  is the electrical resistance at temperature  $T$  and  $R_0$  is the electrical resistance at a reference temperature of  $T_0$ .

Joule heating can be quantified using the relation given in equation 4.

$$Q = I^2R \quad (4)$$

Where  $Q$  is the amount of heat generated,  $I$  is the current, and  $R$  is the resistance. To study the joule heating performance of the coatings an identical amount of power was given to each system for a period of fifteen minutes and their real-time surface temperatures were recorded. The Joule heating performance was then compared based on the rate of increase in surface temperature for given power input. The testing was performed at three different values of input power of 3.5, 35 and 75 W, respectively, by adjusting the applied voltages depending on the resistivity of the coating material, to capture its impact on the performance and any possible variation in the performance trend. All tests were conducted at room temperature and under free convection conditions. At least three tests were conducted to ensure the reproducibility of the results. Ni-20Cr has been chosen as the reference to compare the results as it is the most commonly utilized material for heating elements.

## 2.6. Nanoindentation

The nanoindentation was performed using a Bruker Hysitron TI Premiere Nanoindenter. The indentations were performed at a load of 5 mN using a sharp three-faced pyramid Berkovich diamond tip indenter was used to ensure limited volume penetration. The loading and unloading cycles were separated by 30 s. At least 20 indents were taken for each coating to ensure consistency.

The Oliver and Pharr Methodology [152] has been used to compute the Young's Modulus and Hardness from the series of load-displacement data sets. This method has been reported to be less erroneous due to the analysis of an array of unloading points and can be implemented without using a microscope to image the residual indent for the calculation of hardness [153]. A typical load-displacement plot adapted from the original work by Oliver and Pharr indicating the different parameters has been shown in Fig. 9 for reference [120].

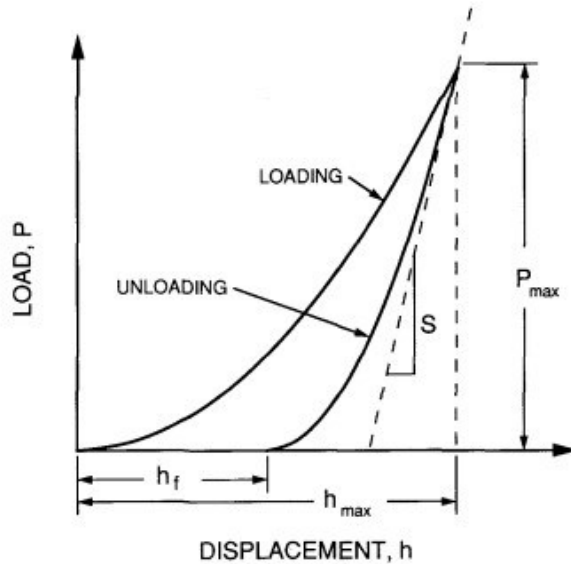


**Figure 9.** A schematic representation of load versus indenter displacement showing quantities used in the analysis. Source Oliver and Pharr, 1992[120].

The Hardness and reduced elastic modulus is given by equation 5 and equation 6 respectively.

$$H = \frac{P_{max}}{A} \quad (5)$$

$$E_r = \frac{\sqrt{\pi}}{2} \frac{S}{\sqrt{A}} \quad (6)$$

Where H is the Hardness,  $P_{max}$  is the peak load attained during indentation (in  $\mu\text{N}$ ) and A is the Contact Area (in  $\text{nm}^2$ ),  $E_r$  is the reduced elastic modulus, S is the stiffness (in  $\mu\text{N}/\text{nm}$ ) that can be determined from the upper portion of the unloading curve as shown in Fig. 9. and A is the contact area of the indenter and substrate.

## 2.7. Solid Particle Erosion

A modified version of the ASTM G-76 standard was used to evaluate the erosion resistance of the HEA coatings. A cold gas dynamic spray system (SST Series P, CenterLine Ltd., Windsor, ON, Canada) was used to accelerate the erodent particles at ambient gas temperatures. The operating parameters have been listed in Table 3. Garnet sand (Super Garnet, V.V. Mineral, Tamil Nadu, India) having an angular morphology and approximate particle diameter of  $349 \pm 57 \mu\text{m}$  ( $n=30$ ) was chosen as the erodent medium. Figure 10. shows the SEM micrograph of the sand particles used in the study. The velocity of the erodent particles at the nozzle exit is estimated to be in the range of 65 to 73 m/s [98] The erosion testing was performed at two different impact angles  $30^\circ$  and  $90^\circ$  at ambient temperature. Erosion tests were also conducted at elevated temperatures and an impact angle of  $30^\circ$  by heating the substrates to  $250^\circ \text{C}$  with the help of cartridge heaters (50 W Miniature High-Temperature Cartridge Heater (D 1/8"×1 1/4"), McMaster-Carr, Aurora, OH, USA) embedded in the copper substrate holder. A temperature controller (E5CC, Process Temperature Controller, 100 ~ 240VAC Panel Mount, Omron Automation and Safety) was used

to maintain the temperature of the copper cube at the desired set-point. A schematic diagram illustrating the setup is shown in Fig. 11.

**Table 3.** Indicates the set of parameters used in erosion testing.

Erosion Testing Parameters	
Pressure of Air (kPa)	43
Test Time (sec)	60
Test Temperature (°C)	23, 300
Erodent Feed Rate (g/min)	53
Standoff Distance (mm)	20
Impact Angle (degree)	30, 90

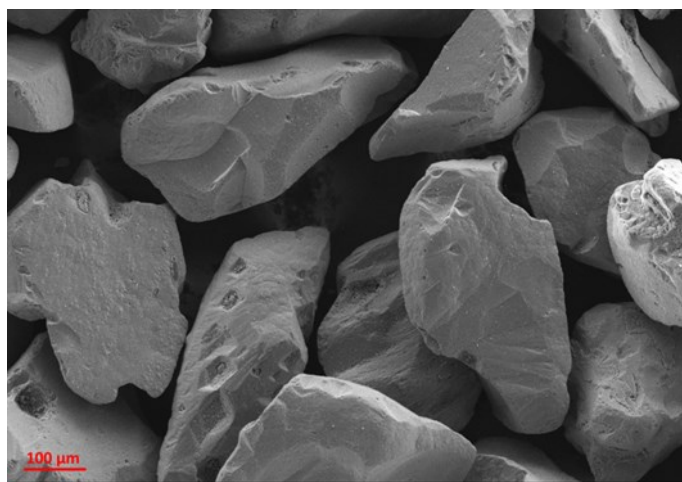


**Figure 10.** SEM image of garnet sand (erodent) used in the solid particle erosion study.

The coated specimens were weighed before and after erosion using a balance (Adventurer Pro AV313, OHAUS Corporation, Parsippany, NJ, USA) with an accuracy of  $\pm 1$  mg. The erosion rate has been defined as the volume loss of the sample per unit mass of erodent particle. The density of the coatings was calculated from the rule of mixtures and the mass losses recorded have been converted to corresponding volume losses. The calculated densities are 7.21 g/cc, 9.5 g/cc, and 7.0 g/cc for AlCoCrFeMo, AlCoCrFeMoW and AlCoCrFeMoV respectively. The sand flow rate was calculated by collecting and weighing the amount of sand ejected from the nozzle for three minutes and is equal to  $50.3 \pm 4.4$  g/min ( $n=5$ ). At least three samples were tested for each parameter set and the average erosion rate values have been reported.

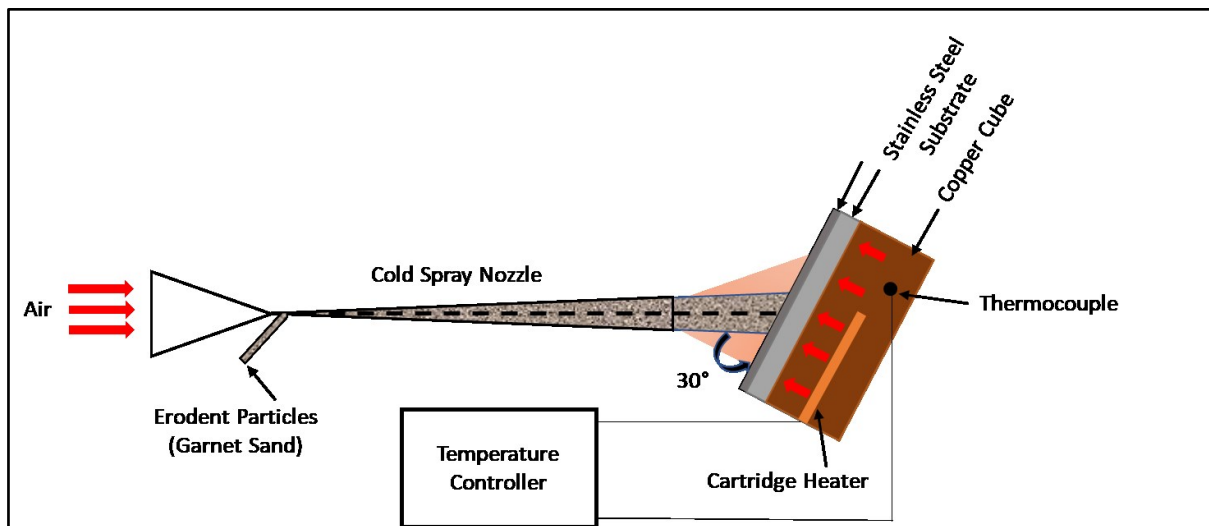


**Figure 11.** Schematic diagram of the high-temperature solid particle erosion setup for  $30^\circ$  impact angle [98].

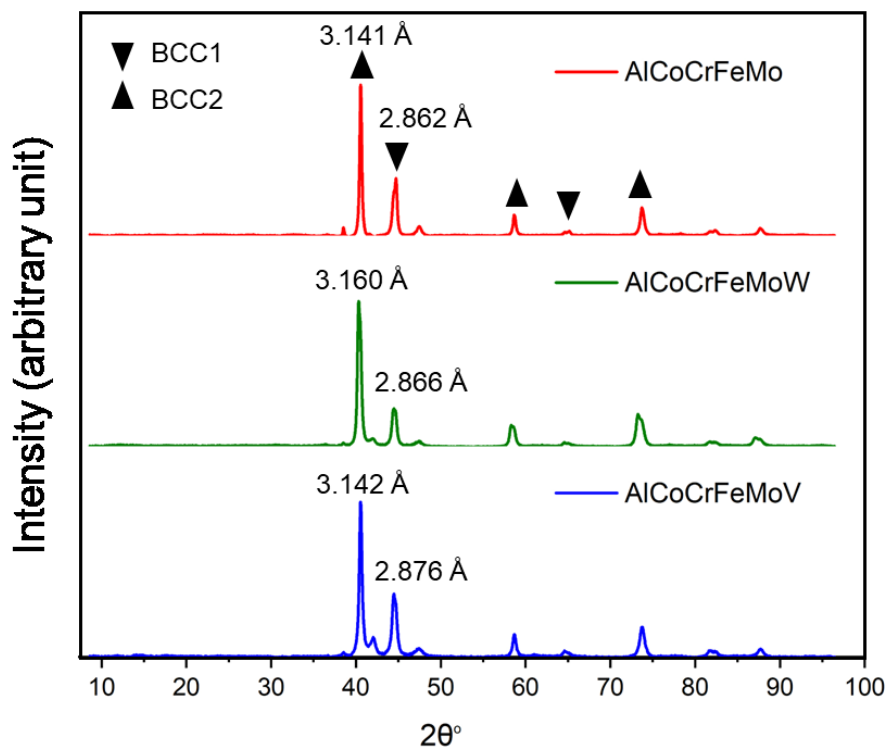
## Chapter 3: Result and Discussion

### 3.1. X-Ray Diffraction (XRD)

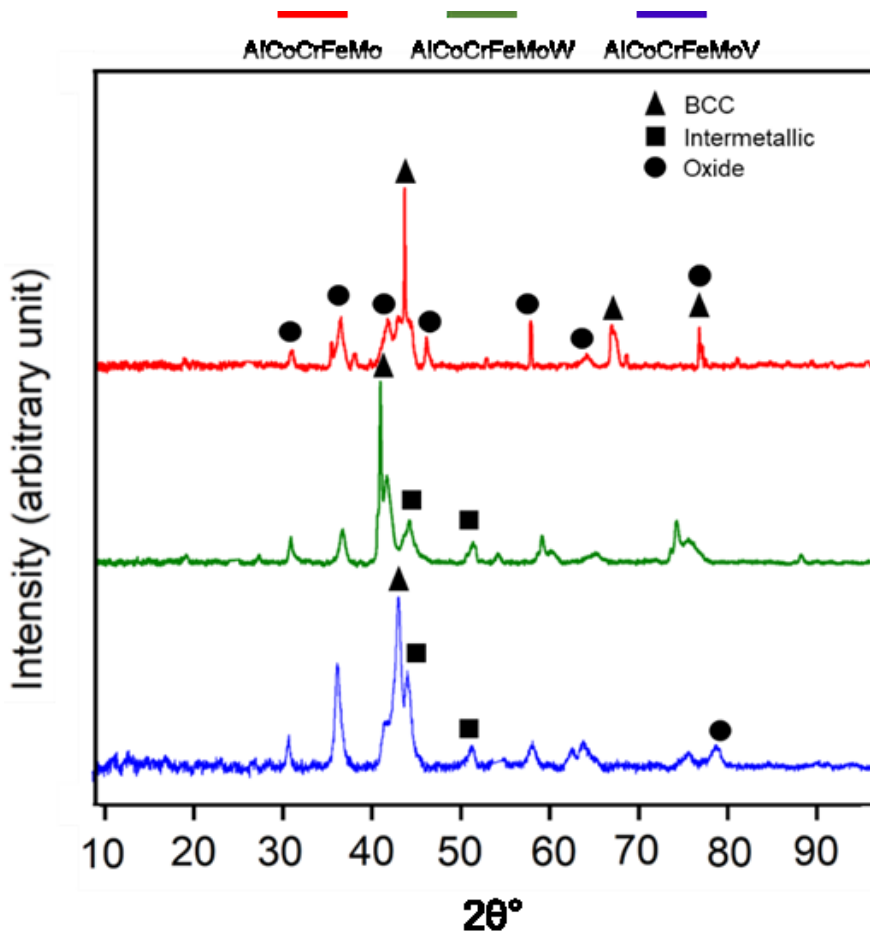
The XRD profiles of the feedstock powders have been shown in Fig. 12. All the three HEA powders show the presence of BCC1 and BCC2 phases. The BCC1 phase is rich in Al, Co, Cr and Fe in the case of AlCoCrFeMo and AlCoCrFeMoW HEA powder and has a lattice parameter of about 2.86 Å. For AlCoCrFeMo HEA powder the BCC1 phase also has a rich content of V and a lattice parameter of 2.87 Å. This is consistent with the observations made by other researchers where the addition of Al in addition to Fe and Cr promotes the formation of BCC phases [143,178]. The BCC2 phase is Mo rich phase with a lattice parameter of 3.14 Å present in both AlCoCrFeMo and AlCoCrFeMoV. On the other hand, the BCC2 phase rich in Mo and W is formed in AlCoCrFeMoW HEA powder. An earlier study by Nair *et al.* [151] suggested that the higher atomic radius of Mo (0.139 nm) and the medium enthalpy of mix of Mo with the other components might be responsible for the limited solubility in AlCoCrFe BCC structure. The similarity in the atomic radius of W and Mo leads to the formation of Mo-W rich BCC phase in AlCoCrFeMo HEA powder.

Figure 13 shows the XRD profiles of the flame-sprayed HEA coatings. All coatings show the presence of mixed oxides and BCC phases. This aligns well with the results previously reported by Nair *et al.* 2022 [151] in their study of flame-sprayed AlCoCrFeMo HEA. Similar results were also reported by Meghawal *et al.* for AlCoCrFeNi fabricated via air plasma spraying [153] and by Patel et al for CoCrFeMnNi high-velocity oxy-fuel coatings [154]. When the XRD profiles of the HEA coatings (in Fig. 13.) are compared with those of the HEA powders (in Fig. 12.) it is noted that the peaks shift to a higher angle in the coatings. This may be attributed to the lattice strains

and changes in composition associated with oxide formation [151]. However, only a minor peak shift is observed in the AlCoCrFeMoW HEA coating when compared to the AlCoCrFeMoW HEA powder. This is probably because of the higher melting point of W compared to the other elements as a result of which it is unable to fuse completely to bring about significant changes. The presence, of unmolten and partially molten particles rich in W, have been observed in the SEM images.



**Figure 12.** XRD Profile of the HEA powders. It shows the presence of two types of BCC phases. The lattice parameters of the two BCC phases have been indicated.



**Figure 13.** XRD profile of flame-sprayed HEA coating

The broadening of peaks in Fig.13. is suggestive of the presence of amorphous structures which can be accounted for by the presence of oxides and intermetallics. Quantitative phase analysis by X-Ray (Rietveld – RIR analysis) has confirmed the presence of a notable amount of oxide and intermetallic phases in AlCoCrFeMoW and AlCoCrFeMoV compositions. The major oxides found for AlCoCrFeMo and AlCoCrFeMoV is a spinel oxide ( $AB_2O_4$ , where A=Fe, B=Co) having a lattice parameter of 8.264 Å and  $Al_2O_3$ . Approximately 24% and 17% of spinel oxides were present in AlCoCrFeMo and AlCoCrFeMoV respectively. However, no presence of spinel oxides

was found in AlCoCrFeMoW. Also, the total percentage of oxide formed in AlCoCrFeMoW was 52% and 39% lower as compared to AlCoCrFeMo and AlCoCrFeMoV. The major oxide formed in AlCoCrFeMoW is of  $\text{ABO}_4$  type which is of monoclinic nature (lattice constants  $a=4.947$ ,  $a/b=0.870$ ,  $c/b=0.821$ ) with A, B being Co, W, Fe, or Al. Moreover, a negligible amount of  $\text{Al}_2\text{O}_3$  was observed in AlCoCrFeMoW. The results of RIR analysis suggest that W tends to preferentially combine with Co, Al and Mo to form complex intermetallics of cubic nature. V on the other hand preferentially combines with Al and Fe resulting in an intermetallic having a BCC-like structure. The presence of iron-chromium intermetallic has also been noted in AlCoCrFeMoV. On addition of W and V to AlCoCrFeMo, there is a peak shift happening to the left. The peak has shifted from  $2\theta = 46^\circ$  for AlCoCrFeMo to  $2\theta = 43^\circ$  for AlCoCrFeMoV and  $2\theta = 40^\circ$  for AlCoCrFeMoW. The shift to a lower angle is more pronounced in AlCoCrFeMoW. This shifting is attributed to the lattice strains caused due changes in chemical composition [155]. The lattice constants calculated are 2.78 Å, 3.18 Å and 2.97 Å for AlCoCrFeMo, AlCoCrFeMoW, and AlCoCrFeMoV respectively. Thus, the addition of tungsten with an atomic radius of 0.139 nm which is higher than all other elements in the given composition causes severe lattice distortion which results in straining and an ultimate peak shift.

### 3.2. SEM

The backscattered cross-sectional SEM micrographs of the three different HEA coatings at low and high magnification have been shown in Fig.14. The typical splat morphology and lamellar structure of the flame-sprayed coatings are evident in all three coatings.

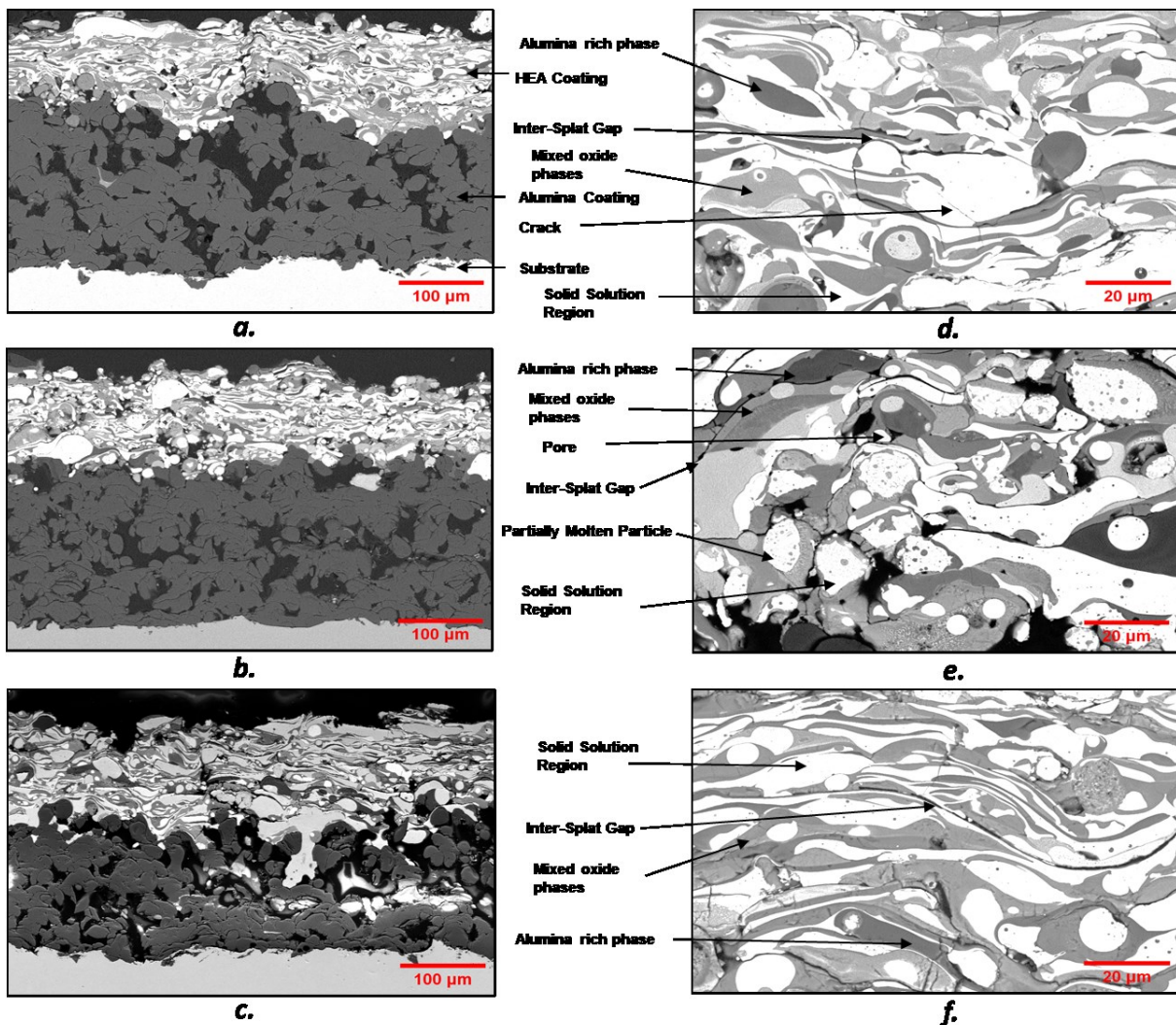


**Figure 14.** SEM micrographs at low (a, b, c) and high (d, e, f) magnifications of (a and d) AlCoCrFeMo, (b and e) AlCoCrFeMoW, and (c and f) AlCoCrFeMoV of the flame sprayed HEA coatings

Thin, flat and elongated splats are observed for AlCoCrFeMo and AlCoCrFeMoV, however, for AlCoCrFeMoW the splats are thicker and more rounded. Tungsten (W) which has a high melting point of 3695 K when added to AlCoCrFeMo results in incompletely melting of the feedstock powder particles before impacting the substrate and consequently rounder splats. The images at

higher magnifications indicate the presence of multiple contrasting regions comprising white, grey and dark grey regions. Additionally, the presence of partially molten, un-molten particles and inter-lamellar cracks are also observed. The presence of partial and un-molten particles could be due to splashing and fragmentation during the impact of large/medium-sized particles on the substrate [151]. Nair *et al.* [151] and Ang *et al.* [156] in their studies on flame-sprayed AlCoCrFeMo and plasma sprayed AlCoCrFeNi and MnCoCrFeNi, respectively have reported the presence of similar microstructure. As observed in Fig.14. there is no observed discontinuity or delamination at the interface between the HEA and alumina layer coating, suggesting proper adhesion between the layers [76]. There is also no evidence of penetration of the HEA layer into the alumina layer in any case.

The apparent porosity and average coating thickness for the three HEA coatings as well as the alumina layer (common in all three coatings) have been reported in Table 4. It can be seen that all the three HEA coatings have similar thickness and porosity levels. The alumina layer shows the presence of inter-connected elongated pores and has a significantly higher level of porosity as compared to the HEA coatings. The lack of fusion between the sprayed particles of alumina which has a high melting point of  $2054^{\circ}\text{C}$  could account for the higher porosity levels [157]. The porosity is also highly dependent on the feedstock powder size and increases with an increase in the size of the feedstock powder [158] thus, the difference in the particle diameters will add to the porosity. However, the presence of high porosity in the alumina layer is desirable as it contributes to the efficiency in electrical insulation.

**Table 4.** Porosity and thickness of the HEA and alumina layer

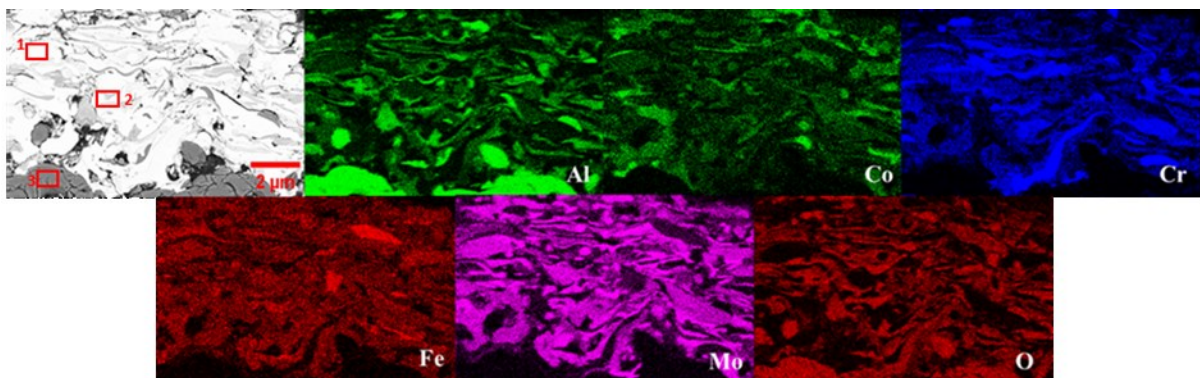
<b>Coating Material</b>	<b>Porosity % (n=10)</b>	<b>Thickness <math>\mu\text{m}</math> (n=10)</b>
<b>AlCoCrFeMo</b>	$2.2 \pm 0.9$	$146 \pm 4$
<b>AlCoCrFeMoW</b>	$3.5 \pm 1.3$	$154 \pm 2$
<b>AlCoCrFeMoV</b>	$4.2 \pm 1.5$	$157 \pm 3$
<b>Alumina</b>	$10.2 \pm 3.1$	$163 \pm 9$

**Table 5.** Elemental composition of the HEA Coatings in atomic percentage as obtained from EDS

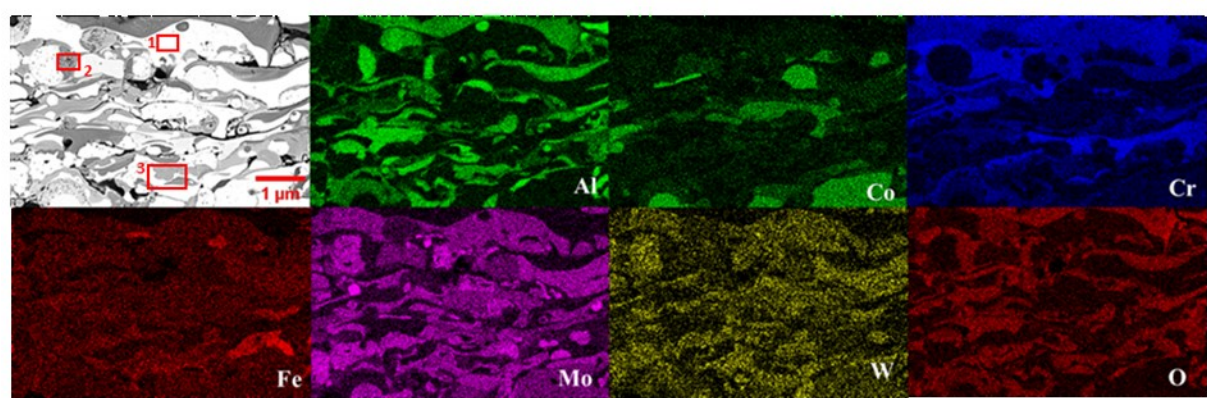
<b>Material</b>	<b>Region</b>	<b>Elemental Composition</b>							
		<b>Al</b>	<b>Co</b>	<b>Cr</b>	<b>Fe</b>	<b>Mo</b>	<b>W</b>	<b>V</b>	<b>O</b>
<b>AlCoCrFeMo</b>	<b>1</b>	9.1	18.3	20.5	20.3	22.1	NA	NA	9.7
	<b>2</b>	10.8	17	17.5	14.7	22.6	NA	NA	17.4
	<b>3</b>	41.9	-	-	-	-	NA	NA	58.1
<b>AlCoCrFeMoW</b>	<b>1</b>	1.0	16.8	9.1	21.9	22.0	16.6	NA	12.7
	<b>2</b>	16.6	0.7	8.8	10.6	1.6	5.2	NA	56.4
	<b>3</b>	8.5	0.9	8.7	21.5	5.4	4.9	NA	50.1
<b>AlCoCrFeMoV</b>	<b>1</b>	25.1	4.3	6.7	9.0	10.8	NA	8.3	35.9
	<b>2</b>	3.4	12.6	11.2	15.4	21.8	NA	14.6	21.0
	<b>3</b>	9.8	14.7	10.6	12.5	24.2	NA	16.1	12.1

To quantify the chemical composition of the phases and oxides EDS analysis and elemental distribution mapping were done and is shown in Fig.15. The three different contrasting regions observed in each coating has been labelled and their respective chemical composition in atomic percentages have been reported in Table 5. Presence of high amount of oxygen is noted in all regions. The evolution of oxides due to the in-flight oxidation of powder particles is a characteristic feature of high-temperature processes [54, 155, 156].

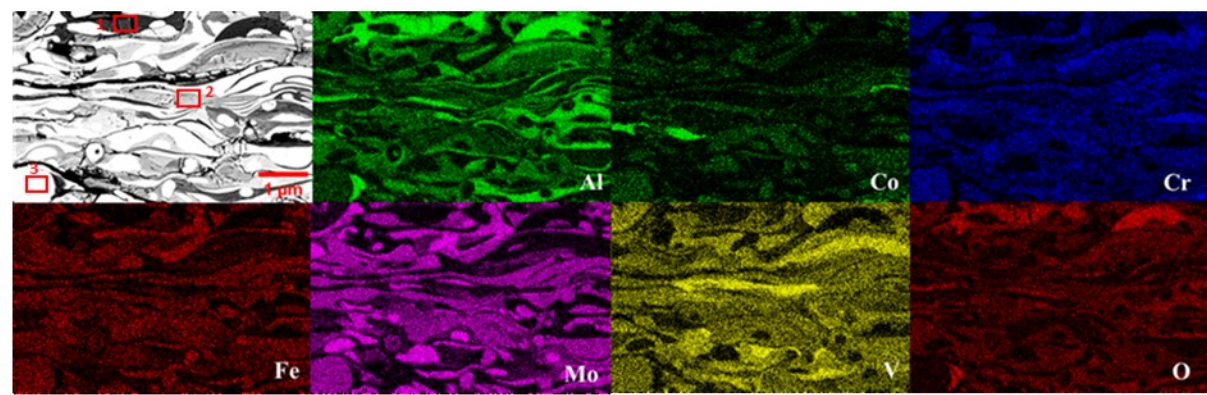
The dark grey region (denoted by 3, 2, and 1 in Fig. 15. 5 a, b, and c respectively) are oxides of aluminium as noted in Table 5. The light grey regions comprise of mixed oxides of the different elements. The bright white regions in all three coatings are depleted of Al and contain a high amount of Mo and an almost equal amount of Co, Cr, Fe, W (in the case of AlCoCrFeMoW) and V (in case of AlCoCrFeMoV) [156]. This suggests the presence of mixed oxide embedded BCC phases [151]. These observations are well in accordance with the XRD results reported in the previous section. The strong affinity of the HEA components to bond with oxygen is possible due to the p-d bonding of Al, Fe and Cr with oxygen. The high enthalpy of formation of  $\text{Al}_2\text{O}_3$  (-1676  $\text{kJ mol}^{-1}$ ) results in the evolution of Al-based dominant oxide phases in the flame spray coatings[151].



**a.**



**b.**



**c.**

**Figure 15.** EDX map of a) AlCoCrFeMo, b) AlCoCrFeMoW, and c) AlCoCrFeMoV of the flame sprayed HEA coatings

### 3.3. Microhardness

The average microhardness of all the coatings is shown in Fig.16. As shown in Fig.16. AlCoCrFeMo HEA coatings showed an average hardness of approximately  $592 \pm 58$  HV. The obtained microhardness also outperforms the AlCoCrFeMo HEA coatings fabricated through the cold spray technique, reported previously by Nair *et al.* [151]. However, the addition of W to AlCoCrFeMo HEA coatings showed a slight improvement of about 3% in microhardness value. On the other hand, AlCoCrFeMoV HEA coatings exhibited the highest average hardness value of around  $714 \pm 64$  HV, which was approximately 17% and 20% higher than that of AlCoCrFeMoW and AlCoCrFeMo HEA coatings, respectively. Higher hardness achieved for the AlCoCrFeMoV HEA coatings could be attributed to concurrent interactions of BCC phases and intermetallics coupled with the existence of oxide inclusions. Prior studies also reported the influence of hard intermetallic phases on high microhardness values [159]. In addition, the high misfit of the atomic radius of the constituent elements may contribute to an increase in hardness for the AlCoCrFeMoV HEA coatings. The Al (0.143 nm), Mo (0.139 nm), W (0.139 nm) and V (0.136 nm) exhibits high atomic radius than Co (0.125nm), Cr (0.128 nm), and Fe (0.126 nm), which facilitate lattice distortion, which eventually may lead to solid-solution strengthening, thus, high hardness. Similar behaviour by the influence of vanadium (V) on both the FCC Co-Cr-Fe-Mn-Ni-V and BCC Cr-Mo-Nb-Ta-V-W-Hf-Ti-Zr families of the high-entropy alloy was reported previously by Yin *et al.* [148]. They have concluded from their work that the presence of vanadium is the key to high strength in both FCC and BCC high entropy alloys and have attributed this to the uniqueness in the atomic volume of vanadium in both BCC and FCC crystals vis-à-vis larger in FCC and smaller in bcc HEAs [148]. Solid solution strengthening due to the mismatch in atomic sizes is a primary cause of the high strength and hardness of HEAs in general. The amount of oxides follow the trend

AlCoCrFeMo (~70%) > AlCoCrFeMoV (~55%) > AlCoCrFeMoW (~33%) whereas, the amount of intermetallics follows the trend AlCoCrFeMoW (~48%) > AlCoCrFeMoV (~28%) > AlCoCrFeMo (~12%). Thus, the presence of both oxides and intermetallics in optimal amount might be the reason for the higher strength in AlCoCrFeMoV.

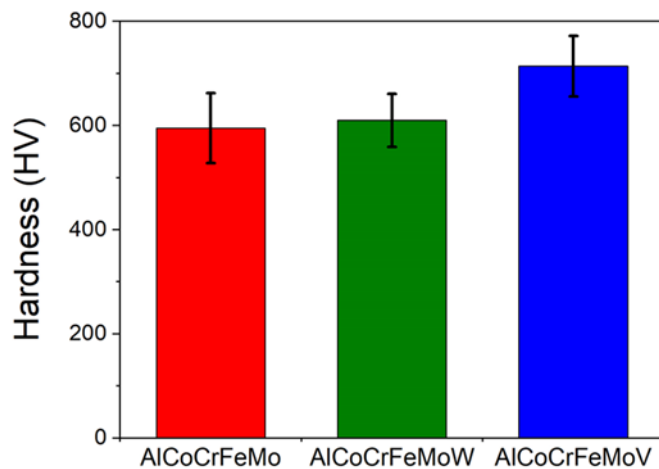


**Figure 16.** Plot indicating the Vicker's Microhardness values of the flame sprayed HEA coatings

### 3.4. Electrical Resistivity and Temperature Coefficient of Resistance (TCR)

The Voltage-Current (VI) characteristics for all three flame-sprayed HEA coatings are shown in Fig. 17. As shown in Fig. 17, a linear relationship between voltage and current was observed for all the coatings, indicating that the HEA coatings were Ohmic in nature.

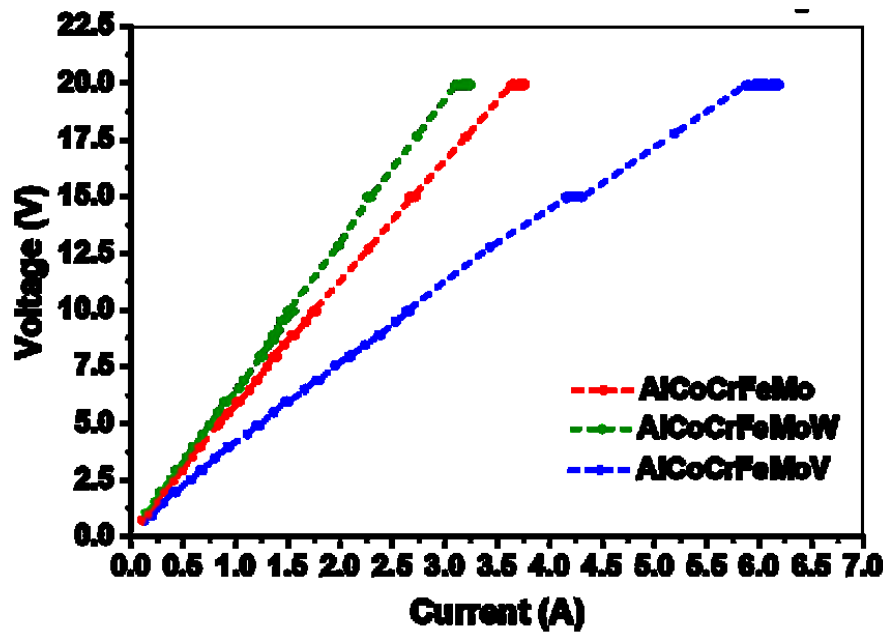


**Figure 17.** Plot showing the variation of voltage with current

Electrical resistivity as the function of temperature for all the HEA coatings is shown in Fig. 18. As shown in Fig. 18 a decrease in trend for the resistivity values with an increase in temperature was found for all the HEA coatings. Table 6 listed the average electrical resistivity and temperature coefficient of resistance recorded after the completion of the test.

**Table 6.** Average resistivity and TCR value of the flame sprayed HEA coatings.

Material	Average Resistivity ( $\times 10^2 \mu\Omega \text{ cm}$ )	TCR ( $\times 10^{-4} \text{ }^\circ\text{C}^{-1}$ )
AlCoCrFeMo	$128.89 \pm 9.69$	-3.82
AlCoCrFeMoW	$78.70 \pm 9.41$	-31.89
AlCoCrFeMoV	$94.83 \pm 6.92$	-7.74

The AlCoCrFeMo HEA coatings exhibited the highest resistivity of around  $128.89 \pm 9.69 \times 10^4 \mu\Omega \text{ cm}$ . By the addition of W and V to AlCoCrFeMo HEA coatings, the electrical resistivity showed approximately 26% and 39% lower values than that of AlCoCrFeMo HEA coatings. However, the values obtained for the HEA coatings were significantly higher than that of the commercially utilized Ni-20Cr coatings, which showed approximately two orders of magnitude higher than those of flame-sprayed Ni-20Cr coatings  $7.9 \times 10^2 \mu\Omega \text{ cm}$  [160],  $1.83 - 4.63 \times 10^2 \mu\Omega \text{ cm}$ , [74] and NiCrAlY coatings  $6.53 \times 10^2 \mu\Omega \text{ cm}$  [161], respectively. The possible reason could be explained based on topological lattice distortion – one of the core effects of high entropy alloys, which may result in high resistivity values for the HEA coatings [12, 104]. The pronounced atomic size misfit due to the high atomic radius for Al (0.143 nm), Mo (0.139 nm), V (0.136 nm), and W (0.139 nm) facilitate severe distortion in the lattice structure. As a result of severe lattice distortion, a strong scattering of electrons may take place due to the reduction of the electron's mean free path, which contributed to an increase in electrical resistivity values for the HEA coatings. A similar study with an increase in resistivity as a result of severe lattice distortion

was found for the physical vapour deposition of AlCoCrFeNi HEA coatings, reported previously by Wang *et al.* [45]. Their study reported that the high atomic radius of Al (0.143 nm) facilitated the topological distortion in the lattice structure, contributing to an increase in electrical resistivity for the HEA coatings.

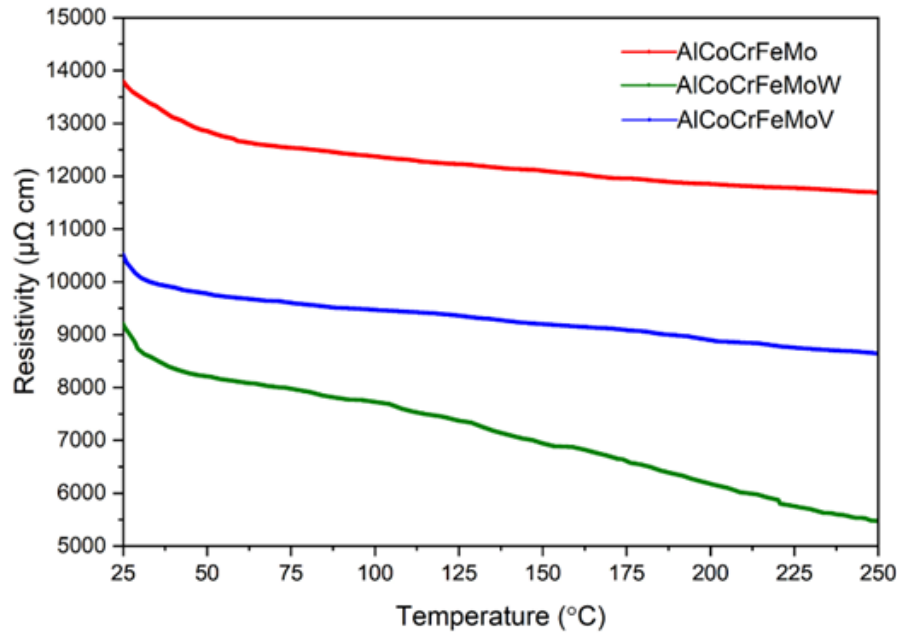


**Figure 18.** Plot showing variation of electrical resistivity with temperature

In addition, HEAs exhibit transition metals with a high concentration of point defects resulting from multi-principal elements in a pseudo-unitary lattice cell [162, 163]. These intrinsic structural defects induce pronounced scattering of electrons, contributing to higher electrical resistivity for the HEA coatings compared to that of conventional Ni-20Cr coatings. Figure 19. shows the

correlation of electrical resistivity with the weight fractions of oxides in HEA coatings. An apparent correlation of Adj. $R^2 = 92\%$  was found between oxides and electrical resistivity as shown in Fig. 19. This correlation suggests that the evolution of oxides due to oxidation in-flight has a strong dependence on the electrical resistivity of the HEA coatings. AlCoCrFeMo HEA coatings exhibited high weight fraction of oxides approximately 70%, followed by AlCoCrFeMoV (~55%) and AlCoCrFeMoW HEA coatings (~30%), respectively. According to literature [164] transition, metal-based oxides are typically non-stoichiometric compounds, which have been found to follow general behaviour as a semiconductor. Furthermore, all the HEA coatings exhibited a negative temperature coefficient of resistance as shown in Table 6. A negative temperature coefficient of resistance is suggesting the decrease in resistivity of the materials with an increase in temperature. As shown in Table 6, AlCoCrFeMo HEA coatings showed the least value approximately  $3.82 \times 10^{-4} \text{ }^\circ\text{C}^{-1}$ , which was 102% and 732% lower than that of AlCoCrFeMoV and AlCoCrFeMoW HEA coatings, respectively. Research studies have reported the occurrence of negative TCR values in the case of many disordered alloys [165-167]. As mentioned previously, the evolution of the high fraction of oxides due to oxidation in-flight acts as a semiconductor, wherein, electrons in the valence band get excited and jump to the conduction band due to an increase in temperature, contributing to a negative temperature coefficient of resistance [165]. According to Mott (1964), the *s-d* scattering of electrons depends on the temperature, expressed in the equation 7.

$$\rho_{s-d} = 1 - \left(\frac{\pi^2}{6}\right) \left(\frac{T}{T_0}\right)^2 \quad (7)$$

where  $kT_0 = E_0 - E_F$ ,  $k$  is the Boltzmann Constant,  $E_0$  and  $E_F$  are Fermi Energy of the d-band at 0 K and T K temperatures. Based on the equation 7, the increase in temperature ( $T$ ) decreases the

resistivity ( $\rho_{s-d}$ ) of the materials, suggesting a negative coefficient of temperature. Hence, as presented in the results, the evolution of oxides and underlying microstructure coupled with topological lattice distortion associated with large atomic size misfit appears to be the primary responsible factor for improvement in electrical resistivity for all the HEA coatings.

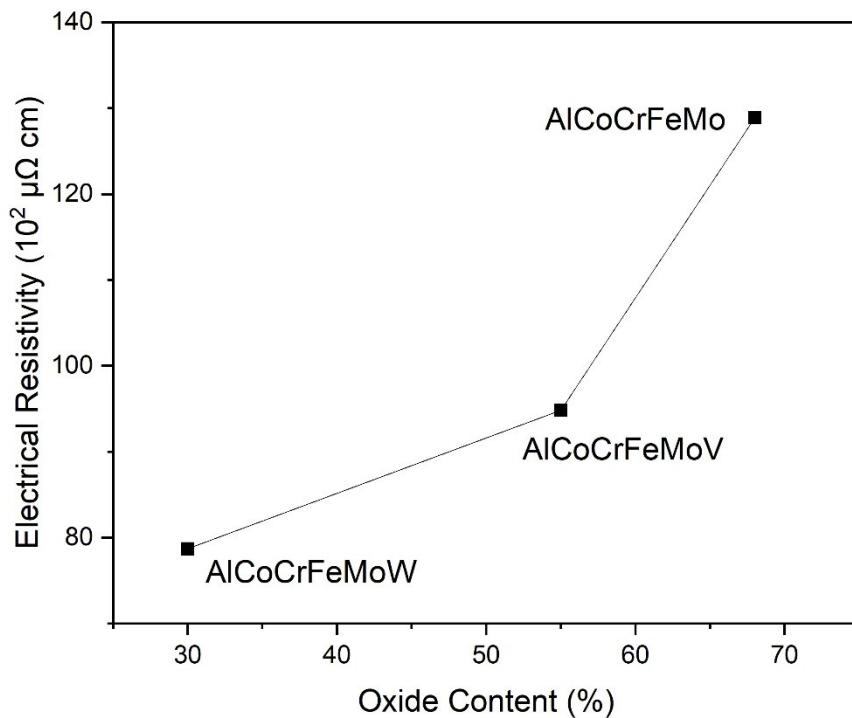


**Figure 19.** Graph of electrical resistivity versus oxide content of flame-sprayed HEA coatings.

### **3.5. Joule Heating Performance**

Joule heating, also known as Ohmic or resistive heating, is the generation of heat in a metal as a result of passing electrical current through the metal over a voltage difference. Under free heat convection conditions, heat may be lost from the coating substrate ensemble as a result of fluid movement due to pressure and density gradients in the air. The air velocities near the coating-substrate system are low, with the majority of air remaining stagnant. On supplying electrical power, the surface temperatures of the coating increased beyond the ambient temperature due to the generation of heat by Joule heating. The Joule heating performance of the coatings has been compared based on the rate of increase in surface temperature for given power input. Figure 20 shows the variation in surface temperature as a function of time during Joule heating of the coatings under free convection. For the purpose of comparison, Ni-20Cr has been utilized in the present investigation. As shown in Fig. 20, it is apparent that the surface temperatures show a linear dependency on time. A linear regression of 99% was found for all the coatings.

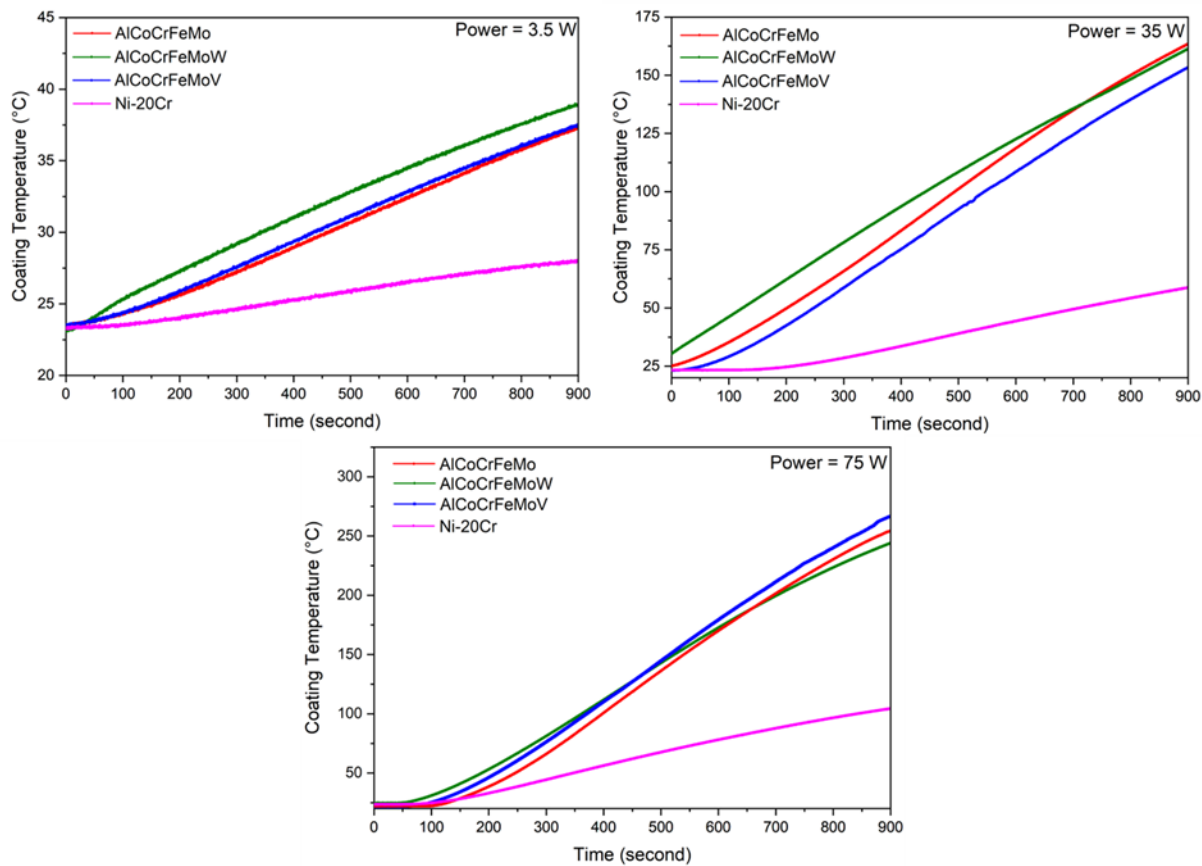


**Figure 20.** Plot showing the variation of temperature with time at a). 3.5 W, b). 35 W and c). 75 W.

The slope of the curve corresponding to the rate of change in temperature was calculated and plotted in Fig. 21. A more rapid change in the rate of increase in temperature is observed at higher powers. The rate of increase in temperature becomes ten times when the power is increased from 3.5 to 35 and two times when the power is doubled from 35 to 75 W. This is expected as more energy is being delivered to the system at higher powers. It should be noted that all the HEA coatings have a higher rate of increase in surface temperature ranging between 2.5 to 3.3 times that

of Ni-20Cr, as observed in the Fig. 21. However, the variation in performance between the HEAs themselves is minuscule. The addition of W and V to AlCoCrFeMo HEA coatings can result in either an increase in the Joule heating performance up to 2% or a decrease to 9% depending on the power input. At low power of 3.5W, AlCoCrFeMoW HEA coatings have a relatively better (~2%) performance. This may be because of the lower resistance of AlCoCrFeMoW which allows a larger current to flow resulting in a greater amount of heat generated as given by equation 4. However, when the power increases from 3.5 to 35 W there is a drop in the temperature values for AlCoCrFeMoW after about 10 minutes as seen in Fig. 21. A similar trend for AlCoCrFeMoW can also be seen after 8 minutes of power being supplied at 75W (Fig. 21). It is also observed that there is a noticeable increase in the temperature values recorded for AlCoCrFeMoV at 75 W. Local changes in the structure like the formation of quasi-stable atomic clusters at elevated temperatures can lead to a decrease in electrical resistivity which will then allow more current to pass resulting in more heat being generated [168]. Advanced characterization like in-situ TEM would be required to support the claims. When a similar amount of electrical energy (power) is given to each of the systems, the HEAs can reach a higher maximum temperature as compared to Ni-20Cr. The stark difference in the Joule heating performance and the higher maximum temperatures attained could be attributed to the difference in resistance (resistivity) values observed between the HEAs and Ni-20Cr coatings.

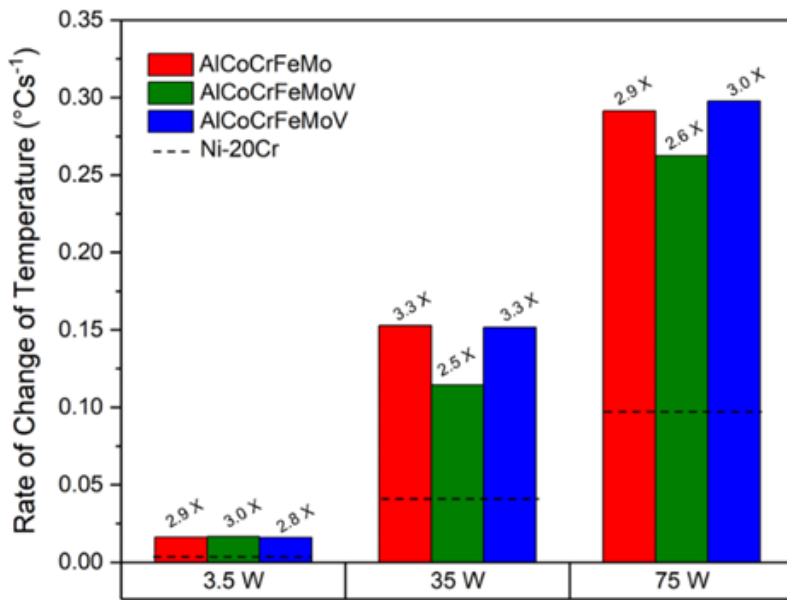


**Figure 21.** Plot comparing the Joule Heating performance of the three HEA coatings with Ni-20Cr at different input powers. The labels above each column are quantitative indications of the performance improvement when compared with Ni-20Cr at similar testing conditions.

Paired *t*-tests were conducted between the three HEA coatings and Ni-20Cr to identify the material with the best performance. The number of data points analyzed were less than 30 hence, it is assumed that the samples follow the *t*-distribution thus, justifying the use of the *t*-statistic for hypothesis testing<sup>2</sup>. To get an accurate comparison between materials and get a better estimation of *p*-values, resampling is applied to experimental results to increase the sample size for each material to 10. The null hypothesis was chosen as: “there is no significant difference in Joule

<sup>2</sup> Evans, M.J. and Rosenthal, J.S., 2004. Probability and statistics: The science of uncertainty. Macmillan.

heating performance between material 1 and material 2.” The python code employed to compute the statistics has been included in Appendix. Table 7 indicates the *p*-value for each pair. A *p*-value (the probability of obtaining test results at least as extreme as the result actually observed) is lesser than the  $\alpha$  value of 0.05 would indicate the presence of a significant difference. It can be seen that the *p*-value is greater than 0.05 when comparing the three HEA coatings themselves. However, the *p*-value is lesser than 0.05 when each of the HEA coatings is compared with Ni-20Cr. Thus, we can conclude statistically that all three HEA coatings have a better Joule heating performance than Ni-20Cr but no significant difference in performance between themselves. Hence, other factors like high-temperature properties, fracture, corrosion and fatigue resistance could be investigated to ascertain the best material for the given application.

**Table 7.** *p*-values of the paired *t*-tests results between Material 1 and Material 2. The hypothesis for the given *t*-test is there is no significant difference in Joule heating performance between Material 1 and Material 2.

<b>Material 1</b>	<b>Material 2</b>	<b><i>p</i>-value</b>
AlCoCrFeMo	Ni-20Cr	0.0019397040399221014
AlCoCrFeMo	AlCoCrFeMoW	0.8453920671263961
AlCoCrFeMo	AlCoCrFeMoV	0.3995021304305474
AlCoCrFeMoW	Ni-20Cr	0.010375297501606503
AlCoCrFeMoW	AlCoCrFeMoV	0.5410487644497303
AlCoCrFeMoV	Ni-20Cr	0.04303931303971115

### 3.6. Nanoindentation / Elastic Modulus and Nanohardness

The nano-hardness, elastic modulus and hardness to elastic modulus ( $H/E$ ) ratio has been computed from the nanoindentation studies of the coatings and reported in Table 8. The nanohardness and the reduced elastic modulus values were recorded to follow the same trend as that of microhardness which has been explained earlier. The average nanohardness and reduced elastic modulus and  $H/E$  the ratio of APS AlCoCrFeNi coatings reported by Meghwal *et al.* is approximately 11 GPa, 152 GPa and 0.063 respectively [153]. All three HEA coatings in this study have lower elastic modulus than those reported for APS AlCoCrFeNi coatings. The flame sprayed AlCoCrFeMoW and AlCoCrFeMoV coatings have a higher hardness than AlCoCrFeNi coatings. The AlCoCrFeMo has a lower hardness and exceptionally low elastic modulus. However, the AlCoCrFeMo has the highest  $H/E$  ratio. This is followed by AlCoCrFeMoW and AlCoCrFeMoV.

**Table 8.** Indicating the microhardness, nano hardness, elastic moduli,  $H/E$  and  $H^3/E^2$  of the different coating systems under study.

Material	Micro-Hardness (GPa) <b>n = 30</b>	Nano-Hardness (GPa) <b>n = 20</b>	Elastic Modulus (GPa) <b>n = 20</b>	$H/E$
<b>AlCoCrFeMo</b>	$5.806 \pm 0.568$	$7.956 \pm 2.109$	$57.751 \pm 7.556$	0.137773
<b>AlCoCrFeMoW</b>	$6.296 \pm 0.5198$	$13.927 \pm 7.969$	$112.723 \pm 37.728$	0.123552
<b>AlCoCrFeMoV</b>	$7.002 \pm 0.627$	$15.518 \pm 6.442$	$138.125 \pm 23.277$	0.112321

The microhardness values reported earlier have been converted to GPa by multiplying by 0.009807 (Gordon calculator reference) and included in Table 8. Compared to the nanohardness the Vickers microhardness values measured seem to be lower. This was anticipated and can be attributed to the indentation size effect (ISE) because of the relatively low load (5 mN) that was used to measure the nanohardness compared to the higher load (300 gf = 2.94 N) used to measure the Vicker's microhardness. According to the indentation size effect (ISE), the generation of strain fields under the smaller indent areas leads to dislocations that are responsible for higher hardness. The Vicker's microhardness measurement is however provides a better indication of the macroscopic properties as it is a calculated balance of different the different microstructural artefacts like phases, porosity and defects that are characteristics of thermal spray processes. On the other hand, because of the small indent size and precise positioning of the indent in nanoindentation defects have minimal impact on the observed values. It thus provides the hardness values of specific phases. The high variability in the nanoindentation results is because the values depend on the individual phase structure and compositions and positioning of the indent within the microstructure.

### 3.7. Solid Particle Erosion

The solid particle erosion rates in terms of volume loss of material per unit mass of erodent particle as a function of impact angle for the three flame-sprayed HEA coatings have been shown in Fig. 23. Figure 22. is indicative of the difference in the shape of the eroded area obtained at different impact angles. The eroded surface area as expected is elliptical at 30° and circular at 90°. Although the eroded area appears to be large at 30° more volume loss of material i.e., a higher erosion rate

has been recorded at an impact angle of  $90^\circ$  as compared to  $30^\circ$ . Erosion rates were 21%, 23 % and 29% lower for AlCoCrFeMo, AlCoCrFeMoW and AlCoCrFeMoV respectively at an impact angle of  $30^\circ$  as compared to  $90^\circ$ . This suggests that the coatings undergo a brittle mode of erosion [80]. Brittle erosion develops in hard materials (such as ceramics) due to the formation of crack networks, and these materials erode quickly at normal incidence ( impact angle = $90^\circ$ ) [114]. The limited number of active slip systems in BCC structures coupled with the complexity of atomic arrangement and difference in the bonding enthalpy of near neighbour atoms in HEA could hinder the movement of dislocations resulting in increased hardness and brittleness [137, 138, 178, 181].

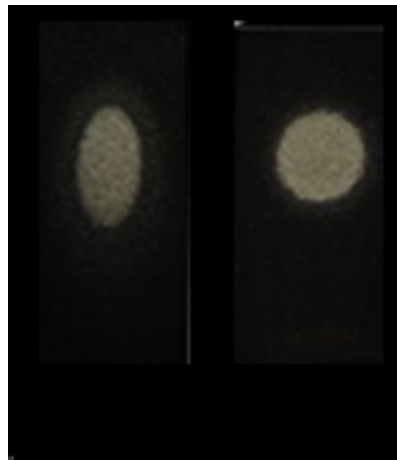


**Figure 22.** Shapes of the eroded scars obtained at different erosion impact angles

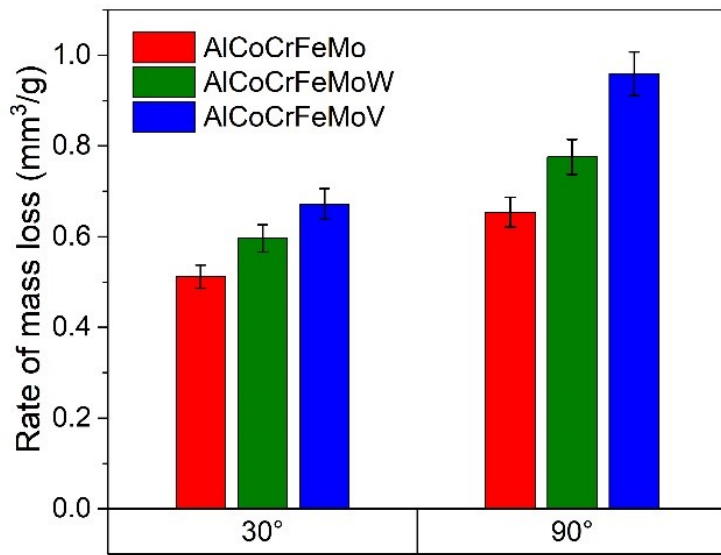


**Figure 23.** Comparison of solid particle erosion rate of the three HEA coatings at varying impact angle.

Figure 24. shows the SEM micrographs of the eroded AlCoCrFeMo HEA coated specimens under the three different testing conditions at low and high magnifications. The eroded surface morphology at an impact angle of 30° has characteristic ploughing marks and lips. The presence of pits, microindents and a few cracks have also been observed. In contrast, the surface eroded at normal incidence (90°) shows the presence of large craters, wide cracks, micro-indents and lips. Figure 25. shows the eroded surface morphology for all the three HEA coatings for the three testing conditions. The AlCoCrFeMoW and AlCoCrFeMoV coatings are observed to have similar surface morphology to that of AlCoCrFeMo as described earlier and hence, have not been further elucidated.

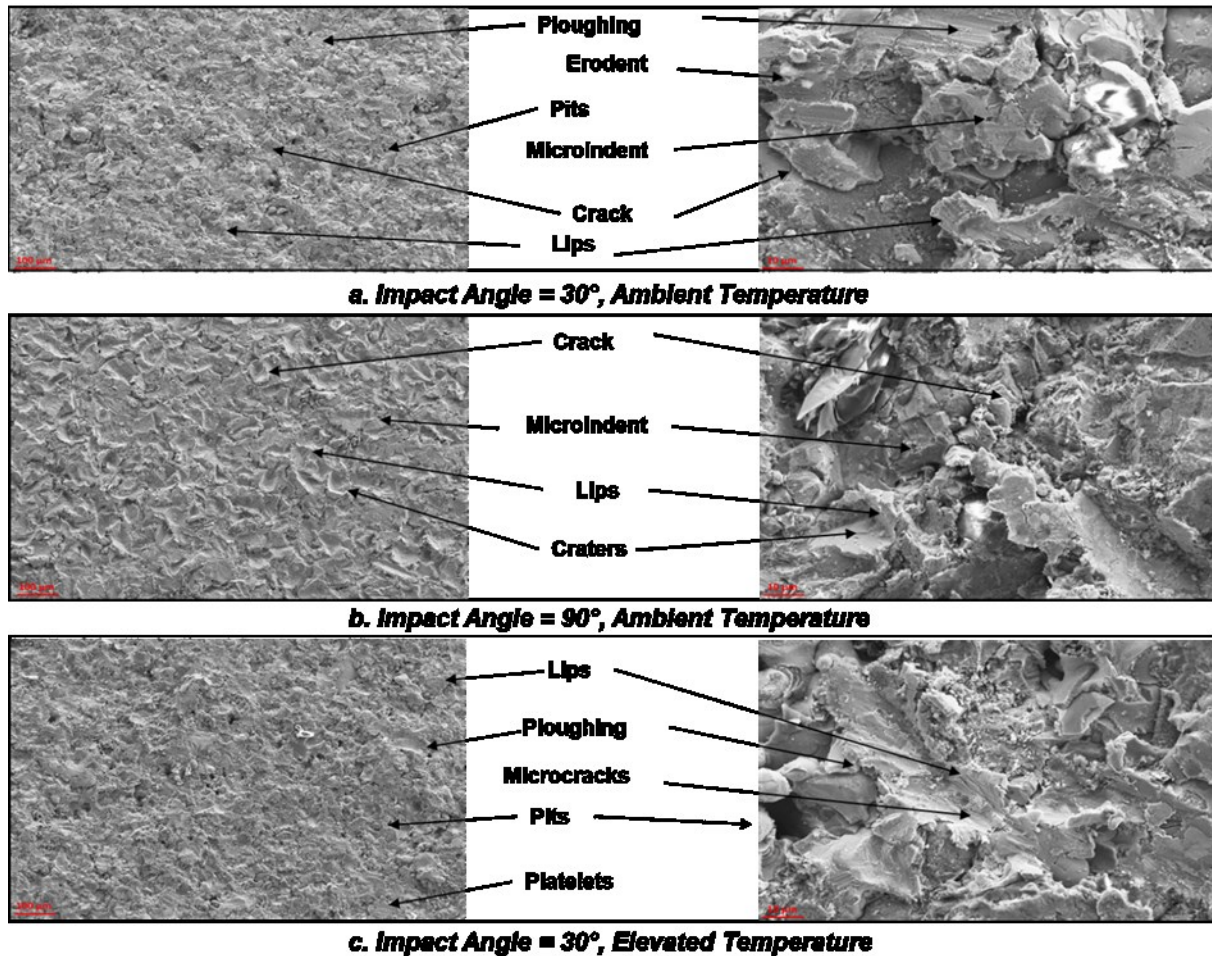
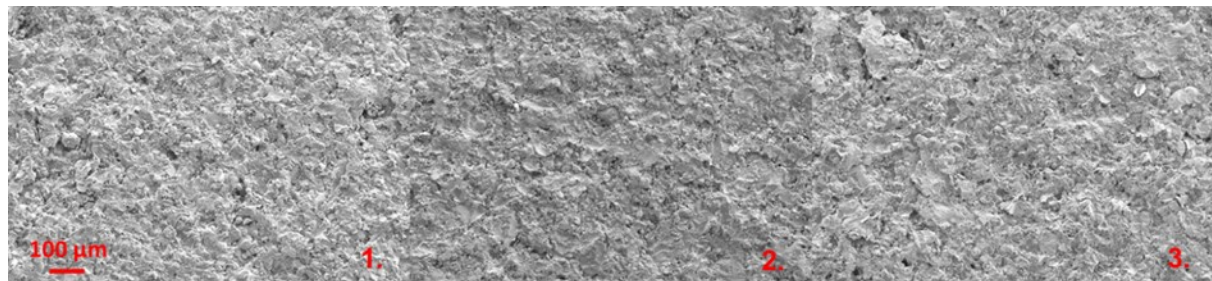
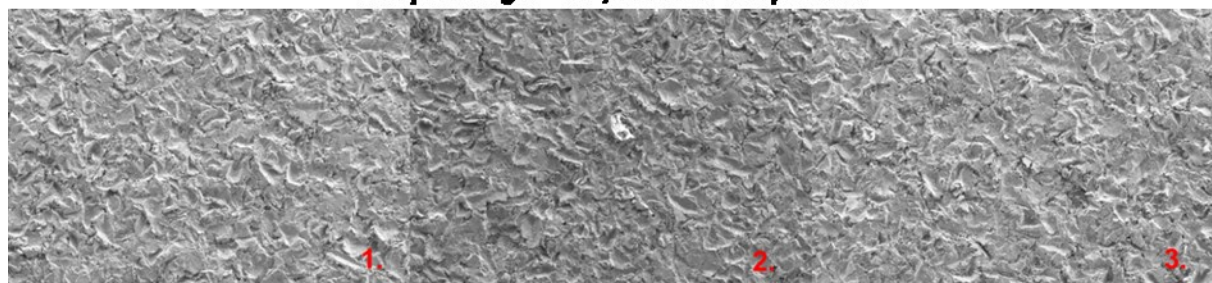


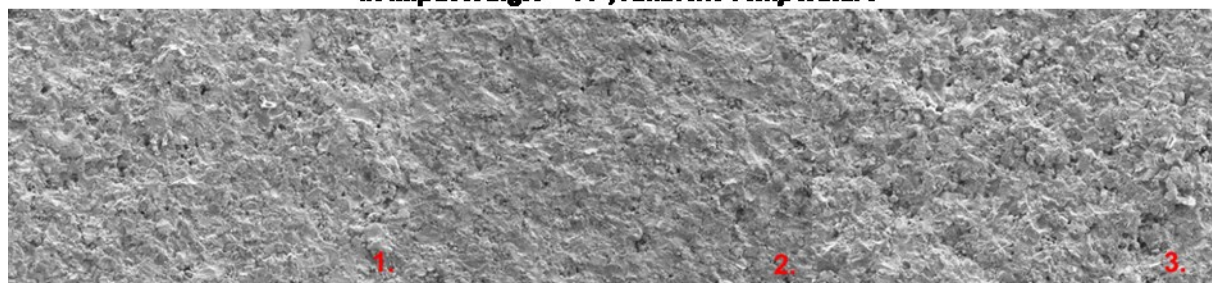
**Figure 24.** Shows the low and high magnification scanning electron micrograph of the eroded surface morphology of AlCoCrFeMo flame sprayed HEA coatings at different testing conditions.



a. Impact Angle = 30°, Ambient Temperature



b. Impact Angle = 90°, Ambient Temperature



c. Impact Angle = 30°, Elevated Temperature

**Figure 25.** Shows the low magnification scanning electron micrograph of the eroded surface morphology of 1. AlCoCrFeMo, 2. AlCoCrFeMoW, 3. AlCoCrFeMoV flame sprayed HEA coatings at different testing conditions.

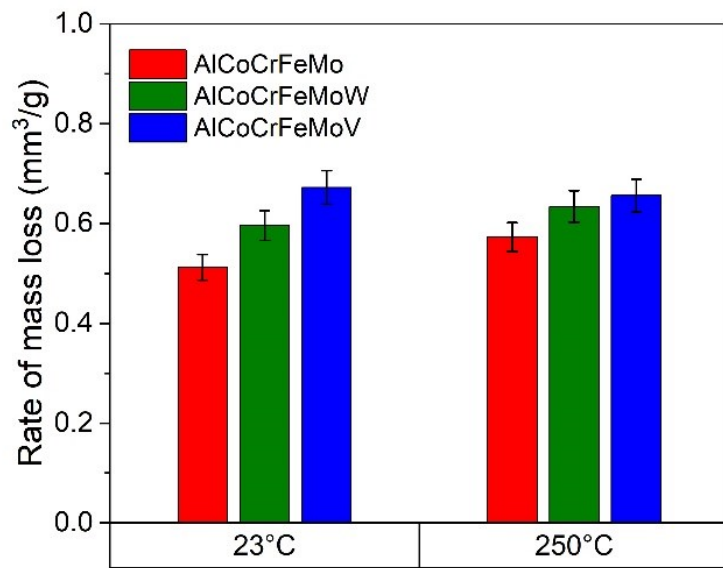
The ratio of particle hardness to target hardness is known to have a strong controlling influence on the erosion mechanism. When this ratio is greater than 1 it results in indentation-induced fractures [97]. This ratio in our case is evidently greater than 1 (hardness of sand particle approximately around 1500 to 1700 HV and coatings between 594 to 750 HV) leading to erosion by splat ejection and indentation-induced material removal. The erosion at an oblique impact angle of 30° is dominated by ploughing and cutting. As observed from the eroded surface morphology at oblique impact angles, the surface of the coatings is first cut by the erodent particles due to large horizontal stress to form furrows. The continuous impact of erosion particles then leads to the extrusion of materials to the edge and the formation of lips. The extrusion lip keeps accumulating material and deforming until it is removed from the surface by fracture. At vertical impact angles loss in material occurs due to the constant impact in the form of indents. The erodent particle impacting the surface of the coating at a normal angle result in the formation of microindents and the initiation of cracks. These cracks grow and propagate during subsequent continuous impact leading to the flaking of materials and the formation of craters. Thus, the major erosion mechanism at a vertical angle is dominated by cracking and crater formation [80, 97, 169-171].

Figure 26 depicts the rate of erosion at room and elevated temperatures for the three HEA coatings. A quick look suggests the absence of a significant difference between the erosion rate at room and elevated temperatures. Independent two-sample *t*-tests were performed for each material. The number of data points analyzed were less than 30 hence, it is assumed that the samples follow the *t*-distribution thus, justifying the use of the *t*-statistic for hypothesis testing<sup>3</sup>. *t*-tests statistically ascertain the difference in the averages of two populations and can be used to determine the equality or relative inequality of respective population means based on sample information [172].

---

<sup>3</sup> Evans, M.J. and Rosenthal, J.S., 2004. Probability and statistics: The science of uncertainty. Macmillan.

The null hypothesis was chosen as: “there is no significant difference in the mean erosion rate between samples eroded at room temperature and at an elevated temperature of 250 °C.” It has been assumed that the two distributions have the same variance. The sample sizes were equal and the tests were performed at a 5% level of significance i.e.  $\alpha = 0.05$ . The obtained  $p$ -values have been indicated in Table 9. Details of the Independent two-sample  $t$ -test and the python code used to generate the results have been included in Appendix A. The  $p$ -values (the probability of obtaining test results at least as extreme as the result actually observed) obtained for all three materials were greater than the  $\alpha$  value of 0.05 thus confirming the null hypothesis. The  $t$ -test results thus provide evidence at a 5% level of significance that there is no difference in the erosion rates at room and elevated temperatures of 250 °C for all the three HEA coatings.



**Figure 26.** Comparison of solid particle erosion rate of the three HEA coatings at room and elevated temperatures.

**Table 9.** Shows the *p*-values of the results of the independent *t*-test assuming equal variances. The null hypothesis was chosen as: “there is no significant difference in the mean erosion rate between samples eroded at room temperature and an elevated temperature of 250 °C.”

Material	<i>p</i> -value
<b>AlCoCrFeMo</b>	0.08974546279588673
<b>AlCoCrFeMoW</b>	0.5047698223225346
<b>AlCoCrFeMoV</b>	0.7475635847327808

These HEA coatings have a high melting point ( $\text{AlCoCrFeMo} \approx 1632^\circ\text{C}$ ,  $\text{AlCoCrFeMoW} \approx 1930^\circ\text{C}$ ,  $\text{AlCoCrFeMoV} \approx 1678^\circ\text{C}$  as calculated using the rule of mixtures) and thus the temperature required to reach the point of thermal softening point which is approximately 0.3 to 0.5  $T_m$  (melting Temperature) is well above 250 °C. Although no significant differences were observed at 250 °C the trend in Fig. 26. could be suggestive an of increase in the rate of erosion at temperatures greater than 500°C or more. The thermal softening effect at elevated temperatures could result in a decrease in strength, hardness and impact resistance AlCoCrFeMo and AlCoCrFeMoW coatings leading to higher erosion at elevated temperatures [173]. Evaluation of erosion rate at higher temperatures and high-temperature mechanical properties would be required to corroborate the aforementioned rationale. The erosion mechanism at elevated temperatures expectedly is similar to what has been described earlier for the erosion at 30° and room temperature

i.e. through ploughing and cutting. Repeated impacts by hard particles have resulted in the formation of highly deformed platelets that are removed by subsequent impacts.

When comparing the erosion rates amongst the coatings themselves it is observed that AlCoCrFeMo has the best performance followed by AlCoCrFeMoW and AlCoCrFeMoV under all testing conditions. The observed trend in the erosion rates is different from the hardness trend wherein AlCoCrFeMoV had the highest hardness followed by AlCoCrFeMoW and AlCoCrFeMo. This suggests that higher hardness does not necessarily imply better erosion resistance and other factors like strength, ductility and toughness have a significant impact on the abrasion, impact and erosion wear properties [106].

**Table 10.** Shows the *p*-values of the paired *t*-tests results between Material 1 and Material 2. The hypothesis for the given *t*-test is there is no significant difference in the mean erosion rate between Material 1 and Material 2.

Material 1	Material 2	<i>p</i> -value
AlCoCrFeMo	AlCoCrFeMoW	0.3569947372063381
AlCoCrFeMo	AlCoCrFeMoV	0.0033700035218105127
AlCoCrFeMoW	AlCoCrFeMoV	0.011383046469980194

Paired *t*-tests were conducted between the three HEA coatings to quantify their individual difference and identify the material with the best performance. To get an accurate comparison between materials and get a better estimation of *p*-values, resampling is applied to experimental results to increase the sample size for each material to 50. The null hypothesis was chosen as: “there is no significant difference in the mean erosion rate between sample 1 and sample 2.” The detailed procedure and python code can be found in Appendix A. Table 10 indicate the *p*-value for each pair. The *p*-value is lesser than the  $\alpha$  value of 0.05 and thus significant when comparing the pair AlCoCrFeMo and AlCoCrFeMoV and the pair AlCoCrFeMoW and AlCoCrFeMoV. Hence, we can conclude that although AlCoCrFeMoV has the highest hardness it has a lesser solid state erosive wear performance than AlCoCrFeMo and AlCoCrFeMoW. The *p*-value and hence the difference between AlCoCrFeMo and AlCoCrFeMoW coatings is statistically insignificant. Hence, the addition of W to AlCoCrFeMo results in no significant changes in erosive wear performance whereas the addition of V to AlCoCrFeMo increases the rate of erosive wear.

A strong co-relation value of Adj.  $R^2 = 93\%$  for AlCoCrFeMo, Adj.  $R^2 = 92\%$  for AlCoCrFeMoW and Adj.  $R^2 = 99\%$  for AlCoCrFeMoV was found between the *H/E* ratio which signifies the material’s ability to resist strain to failure and the erosion rate. The H/E ratio is a measure of the elastic strain to break and is strongly correlated with energy dissipation in mechanical contact [110]. The *H/E* ratio has been found to be proportional to the index of plasticity through a linear relationship given by equation 8.

$$\frac{W_p}{(W_p + W_e)} \approx 1 - x \left( \frac{H}{E_r} \right), \quad (8)$$

where  $W_p$  and  $W_e$  are the plastic and elastic work done  $\frac{W_p}{(W_p+W_e)}$  is the dimensionless plasticity index and  $x$  is a constant. Generally, a higher  $H/E$  ratio implies an increased likelihood of elasticity dominated deformation and has been proposed to control SPE in terms of the transferred energy to the coated surface through the indentation process [110, 174].

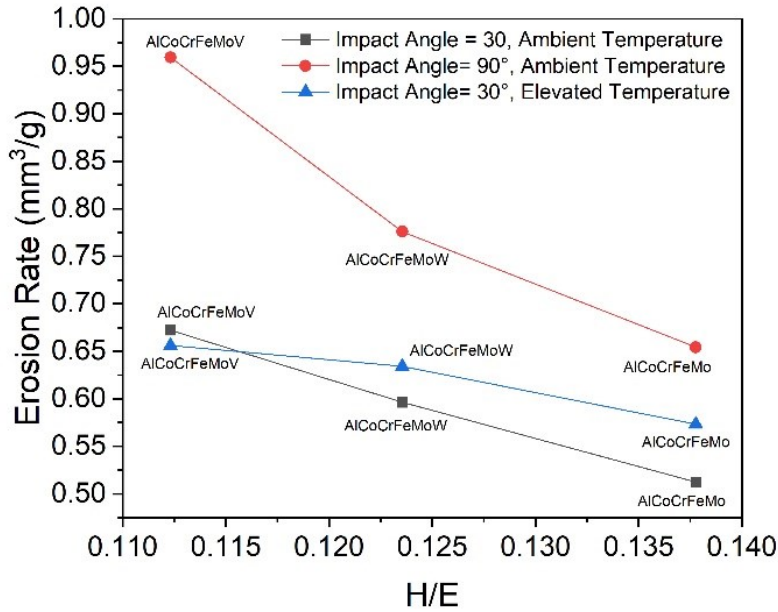


**Figure 27.** Shows the dependence of erosion rate on the  $H/E$  ratio for the three HEA coatings tested under different conditions.

As observed in Fig. 27, the solid particle erosion rate decreases with the increasing value of  $H/E$  ratio of the coatings. Thus, AlCoCrFeMo which has the highest  $H/E$  ratio shows the lowest erosion rate under given conditions. It has been suggested that improvising the  $H/E$  ratio by reducing the elastic modulus could provide better resistance to solid particle erosion [114]. Although AlCoCrFeMo has a lower hardness compared to the other two materials its extremely low modulus results in an ultimate high  $H/E$  ratio and lowest erosion rate.

## **Chapter 4: Conclusion and Summary**

This thesis study explored the feasibility of using flame spraying as a potential manufacturing technique for high entropy alloys coatings. The mechanical and physical properties of the as fabricated flame sprayed coatings were then analyzed for potential multi-functional applications. The major outcomes of the study have been summarized below.

- Novel equiatomic AlCoCrFeMo, AlCoCrFeMoW and AlCoCrFeMoV HEA coatings having an approximate thickness of 150  $\mu\text{m}$  were fabricated by flame spraying on 316 L stainless steel substrates.
- The microstructure of the HEA coatings was characterized using XRD, SEM and EDS. The HEA coatings showed BCC solid solution structures with the presence of mixed oxide regions due to oxidation in-flight.
- Vicker's microhardness tests indicated that the AlCoCrFeMoV HEA coatings has the highest average hardness followed by AlCoCrFeMoW and AlCoCrFeMo HEA coatings. Improvement in hardness is due to solid solution strengthening, BCC phases and a high fraction of oxide regions.
- Electrical characterization has shown that the flame sprayed HEA coatings exhibited high resistivity and negative thermal coefficient of resistance because of the large lattice distortions and s-d scattering of electrons.
- The Joule heating studies have exhibited that the heating performance of all the three HEA coatings was 2 to 3 times better than that of flame sprayed Ni-20Cr. However, the three HEA coatings themselves showed similar heating performance at ambient temperature and

free convection conditions. The improved performance has been attributed to the difference in electrical resistivity observed for Ni-20Cr and the HEA coatings.

- The nanoindentation studies showed that AlCoCrFeMo has a higher elastic strain to break- $H/E$  ratio compared to the other two coatings because of its exceptionally lower elastic modulus compared to the other two materials.
- Solid Particle Erosion studies have shown that the rate of erosion for all three HEA coatings depends on the impact angle. A higher rate of erosion was observed at an impact angle of  $90^\circ$  in comparison to  $30^\circ$  suggesting a brittle mode of failure.
- The erosion rate of all three coatings was found to be independent of temperature on testing up to  $250\text{ }^\circ\text{C}$ .
- It was statistically determined that AlCoCrFeMo and AlCoCrFeMoW coatings have better solid particle erosion resistance than the AlCoCrFeMoV coatings.
- The AlCoCrFeMoV coatings having the highest hardness had the least favourable erosion properties thus high hardness doesn't necessarily imply high erosion resistance. The erosion rate of the coatings was found to be linearly dependent on the  $H/E$  (elastic strain to break) ratio and decreased with increasing value of  $H/E$  ratio.

## Chapter 5: Recommendations for Future Work

The given research project has explored the significance of microstructural features on the electrical and mechanical properties of flame-sprayed HEA coatings. Under high-temperature operations, the coatings are susceptible to microstructural changes which could result in a significant change in properties. For example, Prudenziali *et al.* [74] investigated the change in electrical resistivity of thermal sprayed Ni and Ni-20Cr coatings that occur on repeated heating of the same specimen to high temperatures. They have observed that on repeated heating the resistivity observed in the first cycle was lesser than the one observed in the second cycle for Ni coatings. However, on repeating the tests on the same specimen for a greater number of times they noted the magnitude of change in resistivity in each cycle became lesser and lesser until it reached a stable value. Similar, observations were made for the Ni-20Cr coatings with the exception that their resistivity increased on repeating the tests. They have attributed this to orders taking place at a higher temperature. Bobzin *et al.* [175] also reported an irreversible increase in resistance was noted for the plasma sprayed  $\text{TiO}_x/\text{Cr}_2\text{O}_3$  beyond 300 °C which reaches saturation after conducting heat treatment. The repeated heating of the HEA coatings showed the same trend of change in resistance from the previous cycle to the next with the magnitude of changes decreasing gradually.

For most electrical applications a stable value of resistance is desired. It is anticipated that heat treating the coatings at the ideal temperature for the required amount of time will result in the formation of stable microstructures which will not be further affected by changes in temperature thus leading to stable electrical resistivity. However, it can be time-consuming to figure out the exact heat treatment temperature and duration. Also, the repeated fabrication and heating tests would result in a lot of waste of materials and energy. Hence, advanced machine learning

algorithms based on the Monte-Carlo time series approach could be employed to predict the value of stable electrical resistivity and the ideal heat treatment temperature and duration. To train the model it will be fed with the data for the change in resistance with temperatures for ten heating cycles initially for a given coating. The predicted outcomes of the model can then be verified with a subsequent limited number of experimentations.

In this initial study of the flame sprayed HEA coatings for heating applications the coatings were deposited over rectangular-shaped samples. Electrical components often have complex shapes and patterns. The issue of failure of the complex or patterned coatings at high operating temperatures due to the development of thermal stresses is of great concern from the industrial application point of view [176]. Thus, studying the fatigue, creep and failure properties of complex/patterned thermal sprayed HEA would be essential to understanding the practical feasibility of the proposed application.

The high electrical resistivity observed for the flame-sprayed coatings in this work has been attributed to the inherent nature of HEA (i.e., lattice distortion, disorder), the presence of oxides and other microstructural defects like pores. However, the single most significant factor or the relative influence of each of these factors has not been established. To understand the influence of oxides and porosity on the electrical resistivity HEA coatings having different oxide and porosity could be manufactured using different thermal spray techniques like cold spray and HVOF and their properties compared.

The high-strength flame spray HEA coatings which showed 2 to 3 times better Joule heating performance than conventional Ni-20Cr coatings could be tested for the efficacy in the de-icing process [160, 177]. Ice accretion on the surface of aircraft wings, turbine blades or carbon steel pipes could result in mechanical degradation of the components besides the substantial decrease in performance efficacy and economic losses. Thus, the use of these HEA coatings with superior mechanical and resistive heating performance will be a better alternative.

## References

- [1] B. Gludovatz, A. Hohenwarter, D. Catoor, E. H. Chang, E. P. George, and R. O. Ritchie, “A fracture-resistant high-entropy alloy for cryogenic applications,” *Science* (80-. ), vol. 345, no. 6201, pp. 1153–1158, 2014, doi: 10.1126/science.1254581.
- [2] M. H. Chuang, M. H. Tsai, W. R. Wang, S. J. Lin, and J. W. Yeh, “Microstructure and wear behavior of Al<sub>x</sub>Co 1.5CrFeNi1.5Ti<sub>y</sub> high-entropy alloys,” *Acta Mater.*, vol. 59, no. 16, pp. 6308–6317, 2011, doi: 10.1016/j.actamat.2011.06.041.
- [3] K. H. Cheng, C. H. Lai, S. J. Lin, and J. W. Yeh, “Structural and mechanical properties of multi-element (AlCrMoTaTiZr)N<sub>x</sub> coatings by reactive magnetron sputtering,” *Thin Solid Films*, vol. 519, no. 10, pp. 3185–3190, 2011, doi: 10.1016/j.tsf.2010.11.034.
- [4] Y. J. Chang and A. C. Yeh, “The evolution of microstructures and high temperature properties of Al<sub>x</sub>Co1.5CrFeNi1.5Ti<sub>y</sub> high entropy alloys,” *J. Alloys Compd.*, vol. 653, pp. 379–385, 2015, doi: 10.1016/j.jallcom.2015.09.042.
- [5] H. M. Daoud, A. M. Manzoni, N. Wanderka, and U. Glatzel, “High-Temperature Tensile Strength of Al10Co25Cr8Fe15Ni36Ti6 Compositionally Complex Alloy (High-Entropy Alloy),” *Jom*, vol. 67, no. 10, pp. 2271–2277, 2015, doi: 10.1007/s11837-015-1484-7.
- [6] Z. Fu *et al.*, “Improving the hydrogen embrittlement resistance of a selective laser melted high-entropy alloy via modifying the cellular structures,” *Corros. Sci.*, vol. 190, no. July, p. 109695, 2021, doi: 10.1016/j.corsci.2021.109695.
- [7] Y. Y. Chen, T. Duval, U. D. Hung, J. W. Yeh, and H. C. Shih, “Microstructure and electrochemical properties of high entropy alloys-a comparison with type-304 stainless steel,” *Corros. Sci.*, vol. 47, no. 9, pp. 2257–2279, 2005, doi: 10.1016/j.corsci.2004.11.008.
- [8] Y. Y. Chen, U. T. Hong, H. C. Shih, J. W. Yeh, and T. Duval, “Electrochemical kinetics of the high entropy alloys in aqueous environments - A comparison with type 304 stainless steel,” *Corros. Sci.*, vol. 47, no. 11, pp. 2679–2699, 2005, doi: 10.1016/j.corsci.2004.09.026.
- [9] K. F. Quiambao *et al.*, “Passivation of a corrosion resistant high entropy alloy in non-oxidizing sulfate solutions,” *Acta Mater.*, vol. 164, pp. 362–376, 2019, doi: 10.1016/j.actamat.2018.10.026.
- [10] Y. F. Kao, S. K. Chen, T. J. Chen, P. C. Chu, J. W. Yeh, and S. J. Lin, “Electrical, magnetic, and Hall properties of Al<sub>x</sub>CoCrFeNi high-entropy alloys,” *J. Alloys Compd.*, vol. 509, no. 5, pp. 1607–1614, 2011, doi: 10.1016/j.jallcom.2010.10.210.
- [11] P. Koželj *et al.*, “Discovery of a superconducting high-entropy alloy,” *Phys. Rev. Lett.*, vol. 113, no. 10, pp. 1–5, 2014, doi: 10.1103/PhysRevLett.113.107001.
- [12] Y. Zhang, T. Zuo, Y. Cheng, and P. K. Liaw, “High-entropy alloys with high saturation magnetization, electrical resistivity, and malleability,” *Sci. Rep.*, vol. 3, pp. 1–7, 2013, doi: 10.1038/srep01455.
- [13] J. W. Yeh *et al.*, “Nanostructured high-entropy alloys with multiple principal elements: Novel alloy design concepts and outcomes,” *Adv. Eng. Mater.*, vol. 6, no. 5, pp. 299–303, 2004, doi: 10.1002/adem.200300567.
- [14] B. Cantor, I. T. H. Chang, P. Knight, and A. J. B. Vincent, “Microstructural development in equiatomic multicomponent alloys,” *Mater. Sci. Eng. A*, vol. 375–377, no. 1-2 SPEC. ISS., pp. 213–218, 2004, doi: 10.1016/j.msea.2003.10.257.
- [15] W. Li, D. Xie, D. Li, Y. Zhang, Y. Gao, and P. K. Liaw, “Mechanical behavior of high-entropy alloys,” *Prog. Mater. Sci.*, vol. 118, no. January, p. 100777, 2021, doi:

10.1016/j.pmatsci.2021.100777.

- [16] D. Tejero-Martin, M. Rezvani Rad, A. McDonald, and T. Hussain, *Beyond Traditional Coatings: A Review on Thermal-Sprayed Functional and Smart Coatings*, vol. 28, no. 4. Springer US, 2019.
- [17] X. Feng, G. Tang, M. Sun, X. Ma, L. Wang, and K. Yukimura, “Structure and properties of multi-targets magnetron sputtered ZrNbTaTiW multi-elements alloy thin films,” *Surf. Coatings Technol.*, vol. 228, no. SUPPL.1, pp. S424–S427, 2013, doi: 10.1016/j.surfcoat.2012.05.038.
- [18] B. R. Braeckman *et al.*, “High entropy alloy thin films deposited by magnetron sputtering of powder targets,” *Thin Solid Films*, vol. 580, pp. 71–76, 2015, doi: 10.1016/j.tsf.2015.02.070.
- [19] X. W. Qiu, Y. P. Zhang, and C. G. Liu, “Effect of Ti content on structure and properties of Al<sub>2</sub>CrFeNiCoCuTix high-entropy alloy coatings,” *J. Alloys Compd.*, vol. 585, pp. 282–286, 2014, doi: 10.1016/j.jallcom.2013.09.083.
- [20] T. M. Yue, H. Xie, X. Lin, H. O. Yang, and G. H. Meng, “Solidification behaviour in laser cladding of AlCoCrCuFeNi high-entropy alloy on magnesium substrates,” *J. Alloys Compd.*, vol. 587, pp. 588–593, 2014, doi: 10.1016/j.jallcom.2013.10.254.
- [21] P. K. Huang, J. W. Yeh, T. T. Shun, and S. K. Chen, “Multi-principal-element alloys with improved oxidation and wear resistance for thermal spray coating,” *Adv. Eng. Mater.*, vol. 6, no. 1–2, pp. 74–78, 2004, doi: 10.1002/adem.200300507.
- [22] L. M. Wang, C. C. Chen, J. W. Yeh, and S. T. Ke, “The microstructure and strengthening mechanism of thermal spray coating Ni<sub>x</sub>Co0.6Fe0.2CrySi zAlTi0.2 high-entropy alloys,” *Mater. Chem. Phys.*, vol. 126, no. 3, pp. 880–885, 2011, doi: 10.1016/j.matchemphys.2010.12.022.
- [23] H. Li *et al.*, “Controllable electrochemical synthesis and magnetic behaviors of Mg-Mn-Fe-Co-Ni-Gd alloy films,” *J. Alloys Compd.*, vol. 598, pp. 161–165, 2014, doi: 10.1016/j.jallcom.2014.02.051.
- [24] V. Soare *et al.*, “Electrochemical deposition and microstructural characterization of AlCrFeMnNi and AlCrCuFeMnNi high entropy alloy thin films,” *Appl. Surf. Sci.*, vol. 358, pp. 533–539, 2015, doi: 10.1016/j.apsusc.2015.07.142.
- [25] J. B. Cheng, X. B. Liang, and B. S. Xu, “Effect of Nb addition on the structure and mechanical behaviors of CoCrCuFeNi high-entropy alloy coatings,” *Surf. Coatings Technol.*, vol. 240, pp. 184–190, 2014, doi: 10.1016/j.surfcoat.2013.12.053.
- [26] Q. H. Li, T. M. Yue, Z. N. Guo, and X. Lin, “Microstructure and corrosion properties of alcocrfeni high entropy alloy coatings deposited on AISI 1045 steel by the electrospark process,” *Metall. Mater. Trans. A Phys. Metall. Mater. Sci.*, vol. 44, no. 4, pp. 1767–1778, 2013, doi: 10.1007/s11661-012-1535-4.
- [27] C. Huang, Y. Zhang, and R. Vilar, “Microstructure characterization of laser clad TiVCrAlSi high entropy alloy coating on Ti-6Al-4V substrate,” *Adv. Mater. Res.*, vol. 154–155, pp. 621–625, 2011, doi: 10.4028/www.scientific.net/AMR.154-155.621.
- [28] H. Zhang, Y. Pan, Y. He, and H. Jiao, “Microstructure and properties of 6FeNiCoSiCrAlTi high-entropy alloy coating prepared by laser cladding,” *Appl. Surf. Sci.*, vol. 257, no. 6, pp. 2259–2263, 2011, doi: 10.1016/j.apsusc.2010.09.084.
- [29] Y. He, J. Zhang, H. Zhang, and G. Song, “Effects of different levels of boron on microstructure and hardness of CoCrFeNiAl<sub>x</sub>Cu 0.7 Si 0.1 B y high-entropy alloy coatings by laser cladding,” *Coatings*, vol. 7, no. 1, pp. 1–7, 2017, doi: 10.3390/coatings7010007.

- [30] X. Li, Z. Zheng, D. Dou, and J. Li, “Microstructure and properties of coating of FeAlCuCrCoMn high entropy alloy deposited by direct current magnetron sputtering,” *Mater. Res.*, vol. 19, no. 4, pp. 802–806, 2016, doi: 10.1590/1980-5373-MR-2015-0536.
- [31] T. K. Chen, T. T. Shun, J. W. Yeh, and M. S. Wong, “Nanostructured nitride films of multi-element high-entropy alloys by reactive DC sputtering,” *Surf. Coatings Technol.*, vol. 188–189, no. 1-3 SPEC.ISS., pp. 193–200, 2004, doi: 10.1016/j.surfcoat.2004.08.023.
- [32] C. H. Lai, K. H. Cheng, S. J. Lin, and J. W. Yeh, “Mechanical and tribological properties of multi-element (AlCrTaTiZr)N coatings,” *Surf. Coatings Technol.*, vol. 202, no. 15, pp. 3732–3738, 2008, doi: 10.1016/j.surfcoat.2008.01.014.
- [33] L. H. Tian, W. Xiong, C. Liu, S. Lu, and M. Fu, “Microstructure and Wear Behavior of Atmospheric Plasma-Sprayed AlCoCrFeNiTi High-Entropy Alloy Coating,” *J. Mater. Eng. Perform.*, vol. 25, no. 12, pp. 5513–5521, 2016, doi: 10.1007/s11665-016-2396-6.
- [34] S. Zhang, C. L. Wu, J. Z. Yi, and C. H. Zhang, “Synthesis and characterization of FeCoCrAlCu high-entropy alloy coating by laser surface alloying,” *Surf. Coatings Technol.*, vol. 262, pp. 64–69, 2015, doi: 10.1016/j.surfcoat.2014.12.013.
- [35] D. Dou, X. C. Li, Z. Y. Zheng, and J. C. Li, “Coatings of FeAlCoCuNiV high entropy alloy,” *Surf. Eng.*, vol. 32, no. 10, pp. 766–770, 2016, doi: 10.1080/02670844.2016.1148380.
- [36] P. K. Huang and J. W. Yeh, “Inhibition of grain coarsening up to 1000 °C in (AlCrNbSiTiV)N superhard coatings,” *Scr. Mater.*, vol. 62, no. 2, pp. 105–108, 2010, doi: 10.1016/j.scriptamat.2009.09.015.
- [37] X. Feng, G. Tang, L. Gu, X. Ma, M. Sun, and L. Wang, “Preparation and characterization of TaNbTiW multi-element alloy films,” *Appl. Surf. Sci.*, vol. 261, pp. 447–453, 2012, doi: 10.1016/j.apsusc.2012.08.030.
- [38] M. Zhang, X. Zhou, X. Yu, and J. Li, “Synthesis and characterization of refractory TiZrNbWMo high-entropy alloy coating by laser cladding,” *Surf. Coatings Technol.*, vol. 311, pp. 321–329, 2017, doi: 10.1016/j.surfcoat.2017.01.012.
- [39] M. H. Tsai, “Physical properties of high entropy alloys,” *Entropy*, vol. 15, no. 12, pp. 5338–5345, 2013, doi: 10.3390/e15125338.
- [40] W. Li, P. Liu, and P. K. Liaw, “Microstructures and properties of high-entropy alloy films and coatings: A review,” *Mater. Res. Lett.*, vol. 6, no. 4, pp. 199–229, 2018, doi: 10.1080/21663831.2018.1434248.
- [41] P. C. Lin, C. Y. Cheng, J. W. Yeh, and T. S. Chin, “Soft magnetic properties of high-entropy Fe-Co-Ni-Cr-Al-Si thin films,” *Entropy*, vol. 18, no. 8, pp. 1–9, 2016, doi: 10.3390/e18080308.
- [42] C. Z. Yao *et al.*, “Electrochemical preparation and magnetic study of Bi-Fe-Co-Ni-Mn high entropy alloy,” *Electrochim. Acta*, vol. 53, no. 28, pp. 8359–8365, 2008, doi: 10.1016/j.electacta.2008.06.036.
- [43] C. Y. Cheng and J. W. Yeh, “High-entropy BNbTaTiZr thin film with excellent thermal stability of amorphous structure and its electrical properties,” *Mater. Lett.*, vol. 185, no. September, pp. 456–459, 2016, doi: 10.1016/j.matlet.2016.09.050.
- [44] R. C. Lin, T. K. Lee, D. H. Wu, and Y. C. Lee, “A Study of Thin Film Resistors Prepared Using Ni-Cr-Si-Al-Ta High Entropy Alloy,” *Adv. Mater. Sci. Eng.*, vol. 2015, 2015, doi: 10.1155/2015/847191.
- [45] C. Wang *et al.*, “The resistivity–temperature behavior of Al<sub>x</sub>CoCrFeNi high-entropy alloy films,” *Thin Solid Films*, vol. 700, no. February, 2020, doi: 10.1016/j.tsf.2020.137895.

- [46] S. Y. Chang and D. S. Chen, “10-nm-thick quinary (AlCrTaTiZr)N film as effective diffusion barrier for Cu interconnects at 900 °c,” *Appl. Phys. Lett.*, vol. 94, no. 23, pp. 1–4, 2009, doi: 10.1063/1.3155196.
- [47] S. Y. Chang and D. S. Chen, “(AlCrTaTiZr)N/(AlCrTaTiZr)N0.7 bilayer structure of high resistance to the interdiffusion of Cu and Si at 900 °c,” *Mater. Chem. Phys.*, vol. 125, no. 1–2, pp. 5–8, 2011, doi: 10.1016/j.matchemphys.2010.09.016.
- [48] S. Y. Chang, C. E. Li, Y. C. Huang, H. F. Hsu, J. W. Yeh, and S. J. Lin, “Structural and thermodynamic factors of suppressed interdiffusion kinetics in multi-component high-entropy materials,” *Sci. Rep.*, vol. 4, pp. 1–8, 2014, doi: 10.1038/srep04162.
- [49] S. Y. Chang, C. Y. Wang, M. K. Chen, and C. E. Li, “Ru incorporation on marked enhancement of diffusion resistance of multi-component alloy barrier layers,” *J. Alloys Compd.*, vol. 509, no. 5, pp. L85–L89, 2011, doi: 10.1016/j.jallcom.2010.11.124.
- [50] V. Braic, M. Balaceanu, M. Braic, A. Vladescu, S. Panseri, and A. Russo, “Characterization of multi-principal-element (TiZrNbHfTa)N and (TiZrNbHfTa)C coatings for biomedical applications,” *J. Mech. Behav. Biomed. Mater.*, vol. 10, pp. 197–205, 2012, doi: 10.1016/j.jmbbm.2012.02.020.
- [51] A. Vladescu *et al.*, “In vitro biocompatibility of Si alloyed multi-principal element carbide coatings,” *PLoS One*, vol. 11, no. 8, 2016, doi: 10.1371/journal.pone.0161151.
- [52] L. Pawłowski, *The Science and Engineering of Thermal Spray Coatings: Second Edition*. 2008.
- [53] A. S. M. Ang and C. C. Berndt, “A review of testing methods for thermal spray coatings,” *Int. Mater. Rev.*, vol. 59, no. 4, pp. 179–223, 2014, doi: 10.1179/1743280414Y.0000000029.
- [54] A. Meghwal, A. Anupam, B. S. Murty, C. C. Berndt, R. S. Kottada, and A. S. M. Ang, *Thermal Spray High-Entropy Alloy Coatings: A Review*, vol. 29, no. 5. Springer US, 2020.
- [55] W. L. Hsu, H. Murakami, J. W. Yeh, A. C. Yeh, and K. Shimoda, “On the study of thermal-sprayed Ni0.2Co0.6Fe0.2CrSi0.2AlTi0.2 HEA overlay coating,” *Surf. Coatings Technol.*, vol. 316, pp. 71–74, 2017, doi: 10.1016/j.surfcoat.2017.02.073.
- [56] M. Löbel, T. Lindner, T. Mehner, and T. Lampke, “Microstructure and wear resistance of AlCoCrFeNiTi high-entropy alloy coatings produced by HVOF,” *Coatings*, vol. 7, no. 9, 2017, doi: 10.3390/coatings7090144.
- [57] A. Vallimanaian, S. P. Kumares Babu, S. Muthukumaran, M. Murali, V. Gaurav, and R. Mahendran, “Corrosion behaviour of thermally sprayed Mo added AlCoCrNi high entropy alloy coating,” *Mater. Today Proc.*, vol. 27, pp. 2398–2400, 2019, doi: 10.1016/j.matpr.2019.09.149.
- [58] V. F. Petrenko, C. R. Sullivan, and V. Kozlyuk, “Variable-resistance conductors (VRC) for power-line de-icing,” *Cold Reg. Sci. Technol.*, vol. 65, no. 1, pp. 23–28, 2011, doi: 10.1016/j.coldregions.2010.06.003.
- [59] K. Zhang, B. Han, and X. Yu, “Nickel particle based electrical resistance heating cementitious composites,” *Cold Reg. Sci. Technol.*, vol. 69, no. 1, pp. 64–69, 2011, doi: 10.1016/j.coldregions.2011.07.002.
- [60] A. G. Mohammed, G. Ozgur, and E. Sevkat, “Electrical resistance heating for deicing and snow melting applications: Experimental study,” *Cold Reg. Sci. Technol.*, vol. 160, no. July 2018, pp. 128–138, 2019, doi: 10.1016/j.coldregions.2019.02.004.
- [61] O. Parent and A. Ilinca, “Anti-icing and de-icing techniques for wind turbines: Critical review,” *Cold Reg. Sci. Technol.*, vol. 65, no. 1, pp. 88–96, Jan. 2011, doi:

10.1016/j.coldregions.2010.01.005.

- [62] M. Rezvani-Rad, "Application of Thermally-Sprayed Coatings as Heat Tracers for Carbon Steel Pipes to Mitigate the Effect of Ice Accumulation and Freezing Damage," 2019.
- [63] D. Michels, J. Hadeler, and J. H. Lienhard, "High-heat-flux resistance heaters from vps and hvof thermal spraying," *Exp. Heat Transf.*, vol. 11, no. 4, pp. 341–359, 1998, doi: 10.1080/08916159808946570.
- [64] A. Killinger and R. Gadow, "Thermally Sprayed Coating Composites for Film Heating Devices," *11th Int. Ceram. Congr.*, vol. 45, pp. 1230–1239, 2006, doi: 10.4028/www.scientific.net/ast.45.1230.
- [65] M. Prudenziati, "Development and the implementation of high-temperature reliable heaters in plasma spray technology," *Journal of Thermal Spray Technology*, vol. 17, no. 2, pp. 234–243, Jun. 2008, doi: 10.1007/s11666-008-9164-6.
- [66] M. Floristán, R. Fontarnau, A. Killinger, and R. Gadow, "Development of electrically conductive plasma sprayed coatings on glass ceramic substrates," *Surf. Coatings Technol.*, vol. 205, no. 4, pp. 1021–1028, 2010, doi: 10.1016/j.surfcoat.2010.05.033.
- [67] J. M. Lamarre, P. Marcoux, M. Perrault, R. C. Abbott, and J. G. Legoux, "Performance analysis and modeling of thermally sprayed resistive heaters," *J. Therm. Spray Technol.*, vol. 22, no. 6, pp. 947–953, 2013, doi: 10.1007/s11666-013-9946-3.
- [68] A. Lopera-Valle and A. McDonald, "Application of Flame-Sprayed Coatings as Heating Elements for Polymer-Based Composite Structures," *J. Therm. Spray Technol.*, vol. 24, no. 7, pp. 1289–1301, Oct. 2015, doi: 10.1007/s11666-015-0302-7.
- [69] D. H. Harris, R. J. Janowiecki, C. E. Semler, M. C. Willson, and J. T. Cheng, "Polycrystalline ferrite films for microwave applications deposited by arc-plasma," *J. Appl. Phys.*, vol. 41, no. 3, pp. 1348–1349, 1970, doi: 10.1063/1.1658934.
- [70] R. T. Smyth and J. C. Anderson, "Production of Resistors by Arc Plasma Spraying," *Electrocompon. Sci. Technol.*, vol. 2, no. 2, pp. 135–145, 1975, doi: 10.1155/APEC.2.135.
- [71] H. Herman, S. Sampath, and R. Mccune, "Thermal Spray cureent status and trends," no. July, pp. 17–25, 2000.
- [72] T. Tong, J. Li, Q. Chen, J. P. Longtin, S. Tankiewicz, and S. Sampath, "Ultrafast laser micromachining of thermal sprayed coatings for microheaters: Design, fabrication and characterization," *Sensors Actuators, A Phys.*, vol. 114, no. 1, pp. 102–111, 2004, doi: 10.1016/j.sna.2004.02.012.
- [73] M. Prudenziati, G. Cirri, and P. D. Bo, "Novel high-temperature reliable heaters in plasma spray technology," *J. Therm. Spray Technol.*, vol. 15, no. 3, pp. 329–331, 2006, doi: 10.1361/105996306X124293.
- [74] M. Prudenziati and M. L. Gualtieri, "Electrical properties of thermally sprayed Ni- and Ni<sub>20</sub>Cr-based resistors," *J. Therm. Spray Technol.*, vol. 17, no. 3, pp. 385–394, 2008, doi: 10.1007/s11666-008-9187-z.
- [75] A. Lopera-Valle and A. McDonald, "Application of Flame-Sprayed Coatings as Heating Elements for Polymer-Based Composite Structures," *J. Therm. Spray Technol.*, vol. 24, no. 7, pp. 1289–1301, 2015, doi: 10.1007/s11666-015-0302-7.
- [76] M. Rezvani Rad, M. Mohammadian Bajgiran, C. Moreau, and A. McDonald, "Fabrication of thermally sprayed coating systems for mitigation of ice accumulation in carbon steel pipes and prevention of pipe bursting," *Surf. Coatings Technol.*, vol. 397, no. March, p. 126013, 2020, doi: 10.1016/j.surfcoat.2020.126013.
- [77] S. T. Dehaghani, A. Dolatabadi, and A. McDonald, "Thermally sprayed metal matrix

- composite coatings as heating systems," *Appl. Therm. Eng.*, vol. 196, no. April, 2021, doi: 10.1016/j.applthermaleng.2021.117321.
- [78] K. Bobzin *et al.*, "Thermally sprayed sensor coatings for spatially resolved temperature detection," *J. Mater. Process. Technol.*, vol. 291, no. January, p. 117043, 2021, doi: 10.1016/j.jmatprotec.2021.117043.
- [79] K. Bobzin, H. Heinemann, and A. Schacht, "Assessment of High Entropy Alloys as Thermally Sprayed Heating Elements," pp. 907–912.
- [80] G. Sundararajan and R. Manish, "Solid particle erosion behaviour of metallic materials at room and elevated temperatures," *Tribol. Int.*, vol. 30, no. 5, pp. 339–359, 1997, doi: 10.1016/S0301-679X(96)00064-3.
- [81] E. Bousser, L. Martinu, and J. E. Klemburg-Sapieha, "Solid particle erosion mechanisms of protective coatings for aerospace applications," *Surf. Coatings Technol.*, vol. 257, pp. 165–181, 2014, doi: 10.1016/j.surfcoat.2014.08.037.
- [82] M. Parsi, K. Najmi, F. Najafifard, S. Hassani, B. S. McLaury, and S. A. Shirazi, "A comprehensive review of solid particle erosion modeling for oil and gas wells and pipelines applications," *J. Nat. Gas Sci. Eng.*, vol. 21, pp. 850–873, 2014, doi: 10.1016/j.jngse.2014.10.001.
- [83] L. Cao, C. Tu, P. Hu, and S. Liu, "Influence of solid particle erosion (SPE) on safety and economy of steam turbines," *Appl. Therm. Eng.*, vol. 150, no. June 2018, pp. 552–563, 2019, doi: 10.1016/j.applthermaleng.2018.12.172.
- [84] G. P. Tilly, "Erosion caused by airborne particles," *Wear*, vol. 14, no. 1, pp. 63–79, 1969, doi: 10.1016/0043-1648(69)90035-0.
- [85] J. T. DeMasi-Marcin and D. K. Gupta, "Protective coatings in the gas turbine engine," *Surf. Coatings Technol.*, vol. 68–69, no. C, pp. 1–9, 1994, doi: 10.1016/0257-8972(94)90129-5.
- [86] D. W. Wheeler and R. J. K. Wood, "Erosion damage in diamond coatings by high velocity sand impacts," *Philos. Mag.*, vol. 87, no. 36, pp. 5719–5740, 2007, doi: 10.1080/14786430701713828.
- [87] S. Amirhaghi, H. S. Reehal, R. J. K. Wood, and D. W. Wheeler, "Diamond coatings on tungsten carbide and their erosive wear properties," *Surf. Coatings Technol.*, vol. 135, no. 2–3, pp. 126–138, 2001, doi: 10.1016/S0257-8972(00)01083-5.
- [88] E. Bousser, L. Martinu, and J. E. Klemburg-Sapieha, "Solid particle erosion mechanisms of hard protective coatings," *Surf. Coatings Technol.*, vol. 235, pp. 383–393, 2013, doi: 10.1016/j.surfcoat.2013.07.050.
- [89] H. G. Prengel, P. C. Jindal, K. H. Wendt, A. T. Santhanam, P. L. Hegde, and R. M. Penich, "A new class of high performance PVD coatings for carbide cutting tools," *Surf. Coatings Technol.*, vol. 139, no. 1, pp. 25–34, 2001, doi: 10.1016/S0257-8972(00)01080-X.
- [90] F. Zupanič, "Wear resistance of coke-crushing hammers," *Can. Metall. Q.*, vol. 52, no. 4, pp. 458–464, 2013, doi: 10.1179/1879139513Y.0000000103.
- [91] M. A. Uusitalo, P. M. J. Vuoristo, and T. A. Mäntylä, "High temperature corrosion of coatings and boiler steels in oxidizing chlorine-containing atmosphere," *Mater. Sci. Eng. A*, vol. 346, no. 1–2, pp. 168–177, 2003, doi: 10.1016/S0921-5093(02)00537-3.
- [92] M. A. Uusitalo, P. M. J. Vuoristo, and T. A. Mäntylä, "High temperature corrosion of coatings and boiler steels below chlorine-containing salt deposits," *Corros. Sci.*, vol. 46, no. 6, pp. 1311–1331, 2004, doi: 10.1016/j.corsci.2003.09.026.
- [93] P. M. Roger, I. M. Hutchings, and J. A. Little, "Oberflächenbehandlung gegen Erosion.pdf," vol. 187, pp. 238–246, 1995.

- [94] M. R. Ramesh, S. Prakash, S. K. Nath, P. K. Sapra, and B. Venkataraman, “Solid particle erosion of HVOF sprayed WC-Co/NiCrFeSiB coatings,” *Wear*, vol. 269, no. 3–4, pp. 197–205, 2010, doi: 10.1016/j.wear.2010.03.019.
- [95] J. R. T. Branco, R. Gansert, S. Sampath, C. C. Berndt, and H. Herman, “Solid particle erosion of plasma sprayed ceramic coatings,” *Mater. Res.*, vol. 7, no. 1, pp. 147–153, 2004, doi: 10.1590/s1516-14392004000100020.
- [96] P. Kulu, I. Hussainova, and R. Veinthal, “Solid particle erosion of thermal sprayed coatings,” *Wear*, vol. 258, no. 1–4 SPEC. ISS., pp. 488–496, 2005, doi: 10.1016/j.wear.2004.03.021.
- [97] N. Krishnamurthy, M. S. Murali, B. Venkataraman, and P. G. Mukunda, “Characterization and solid particle erosion behavior of plasma sprayed alumina and calcia-stabilized zirconia coatings on Al-6061 substrate,” *Wear*, vol. 274–275, pp. 15–27, 2012, doi: 10.1016/j.wear.2011.08.003.
- [98] H. Ashrafizadeh, P. Mertiny, and A. McDonald, “Evaluation of the effect of temperature on mechanical properties and wear resistance of polyurethane elastomers,” *Wear*, vol. 368–369, pp. 26–38, 2016, doi: 10.1016/j.wear.2016.08.008.
- [99] D. G. Bhosale, T. R. Prabhu, W. S. Rathod, M. A. Patil, and S. W. Rukhande, “High temperature solid particle erosion behaviour of SS 316L and thermal sprayed WC-Cr<sub>3</sub>C<sub>2</sub>–Ni coatings,” *Wear*, vol. 462–463, no. May, p. 203520, 2020, doi: 10.1016/j.wear.2020.203520.
- [100] A. Vallimanalan *et al.*, “Synthesis, characterisation and erosion behaviour of AlCoCrMoNi high entropy alloy coating,” *Mater. Res. Express*, vol. 6, no. 11, p. 116543, 2019, doi: 10.1088/2053-1591/ab4477.
- [101] S. Kumar, D. Kumar, O. Maulik, A. K. Pradhan, V. Kumar, and A. Patniak, “Synthesis and Air Jet Erosion Study of AlXFe1.5CrMnNi0.5 ( $x = 0.3, 0.5$ ) High-Entropy Alloys,” *Metall. Mater. Trans. A Phys. Metall. Mater. Sci.*, vol. 49, no. 11, pp. 5607–5618, 2018, doi: 10.1007/s11661-018-4894-7.
- [102] J. Lv *et al.*, “Effects of WC addition on the erosion behavior of high-velocity oxygen fuel sprayed AlCoCrFeNi high-entropy alloy coatings,” *Ceram. Int.*, vol. 48, no. 13, pp. 18502–18512, 2022, doi: 10.1016/j.ceramint.2022.03.120.
- [103] S. Zhang *et al.*, “Microstructure and high temperature erosion behavior of laser cladded CoCrFeNiSi high entropy alloy coating,” *Surf. Coatings Technol.*, vol. 417, no. 66, 2021, doi: 10.1016/j.surfcoat.2021.127218.
- [104] H. Kim *et al.*, “Mechanical and electrical properties of NbMoTaW refractory high-entropy alloy thin films,” *Int. J. Refract. Met. Hard Mater.*, vol. 80, no. January, pp. 286–291, 2019, doi: 10.1016/j.ijrmhm.2019.02.005.
- [105] Y. Y. Santana *et al.*, “Influence of mechanical properties of tungsten carbide-cobalt thermal spray coatings on their solid particle erosion behaviour,” *Surf. Eng.*, vol. 28, no. 4, pp. 237–243, 2012, doi: 10.1179/1743294411Y.0000000016.
- [106] A. Leyland and A. Matthews, “On the significance of the H/E ratio in wear control: A nanocomposite coating approach to optimised tribological behaviour,” *Wear*, vol. 246, no. 1–2, pp. 1–11, 2000, doi: 10.1016/S0043-1648(00)00488-9.
- [107] A. Leyland and A. Matthews, “Design criteria for wear-resistant nanostructured and glassy-metal coatings,” *Surf. Coatings Technol.*, vol. 177–178, pp. 317–324, 2004, doi: 10.1016/j.surfcoat.2003.09.011.
- [108] C. Rebholz, H. Ziegele, A. Leyland, and A. Matthews, “Structure, mechanical and

tribological properties of nitrogen-containing chromium coatings prepared by reactive magnetron sputtering,” *Surf. Coatings Technol.*, vol. 115, no. 2–3, pp. 222–229, 1999, doi: 10.1016/S0257-8972(99)00240-6.

- [109] M. A. Baker, S. Klose, C. Rebholz, A. Leyland, and A. Matthews, “Evaluating the microstructure and performance of nanocomposite PVD TiAlBN coatings,” *Surf. Coatings Technol.*, vol. 151–152, pp. 338–343, 2002, doi: 10.1016/S0257-8972(01)01657-7.
- [110] B. D. Beake, “The influence of the H/E ratio on wear resistance of coating systems – Insights from small-scale testing,” *Surf. Coatings Technol.*, vol. 442, no. February, p. 128272, 2022, doi: 10.1016/j.surfcoat.2022.128272.
- [111] J. A. Greenwood and J. B. P. Williamson, “Contact of nominally flat surfaces,” *Proc. R. Soc. London. Ser. A. Math. Phys. Sci.*, vol. 295, no. 1442, pp. 300–319, 1966, doi: 10.1098/rspa.1966.0242.
- [112] J. Musil and M. Jirout, “Toughness of hard nanostructured ceramic thin films,” *Surf. Coatings Technol.*, vol. 201, no. 9-11 SPEC. ISS., pp. 5148–5152, 2007, doi: 10.1016/j.surfcoat.2006.07.020.
- [113] J. Musil, “Hard nanocomposite coatings: Thermal stability, oxidation resistance and toughness,” *Surf. Coatings Technol.*, vol. 207, pp. 50–65, 2012, doi: 10.1016/j.surfcoat.2012.05.073.
- [114] S. Hassani, M. Bielawski, W. Beres, L. Martinu, M. Balazinski, and J. E. Klemburg-Sapieha, “Predictive tools for the design of erosion resistant coatings,” *Surf. Coatings Technol.*, vol. 203, no. 3–4, pp. 204–210, 2008, doi: 10.1016/j.surfcoat.2008.08.050.
- [115] E. Bousser, M. Benkahoul, L. Martinu, and J. E. Klemburg-Sapieha, “Effect of microstructure on the erosion resistance of Cr-Si-N coatings,” *Surf. Coatings Technol.*, vol. 203, no. 5–7, pp. 776–780, 2008, doi: 10.1016/j.surfcoat.2008.08.012.
- [116] E. Bousser, L. Martinu, and J. E. Klemburg-Sapieha, “Solid particle erosion mechanisms of protective coatings for aerospace applications,” *Surf. Coatings Technol.*, vol. 257, pp. 165–181, 2014, doi: 10.1016/j.surfcoat.2014.08.037.
- [117] J. Deng, F. Wu, Y. Lian, Y. Xing, and S. Li, “Erosion wear of CrN, TiN, CrAlN, and TiAlN PVD nitride coatings,” *Int. J. Refract. Met. Hard Mater.*, vol. 35, pp. 10–16, 2012, doi: 10.1016/j.ijrmhm.2012.03.002.
- [118] A. Fischer-Cripps, *Mechanical Characterizations of Surfaces and Coatings*. Elsevier Ltd, 2006.
- [119] H. Wang, L. Zhu, and B. Xu, “Residual Stresses and Nanoindentation Testing of Films and Coatings,” *Residual Stress. Nanoindentation Test. Film. Coatings*, pp. 21–36, 2018, doi: 10.1007/978-981-10-7841-5.
- [120] W. C. Oliver and G. M. Pharr, “An improved technique for determining hardness and elastic modulus using load and displacement,” *J Mater Res*, vol. 7, no. 1, pp. 1564–1583, 1992.
- [121] E. Weppelmann and M. V. Swain, “Investigation of the stresses and stress intensity factors responsible for fracture of thin protective films during ultra-micro indentation tests with spherical indenters,” *Thin Solid Films*, vol. 286, no. 1–2, pp. 111–121, 1996, doi: 10.1016/S0040-6090(95)08525-4.
- [122] A. A. Volinsky, J. B. Vella, and W. W. Gerberich, “Fracture toughness, adhesion and mechanical properties of low-K dielectric thin films measured by nanoindentation,” *Thin Solid Films*, vol. 429, no. 1–2, pp. 201–210, 2003, doi: 10.1016/S0040-6090(03)00406-1.
- [123] B. Yang, L. Riester, and T. G. Nieh, “Strain hardening and recovery in a bulk metallic glass under nanoindentation,” *Scr. Mater.*, vol. 54, no. 7, pp. 1277–1280, 2006, doi:

10.1016/j.scriptamat.2005.12.049.

- [124] X. Fu, C. A. Schuh, and E. A. Olivetti, “Materials selection considerations for high entropy alloys,” *Scr. Mater.*, vol. 138, pp. 145–150, 2017, doi: 10.1016/j.scriptamat.2017.03.014.
- [125] O. A. Waseem and H. J. Ryu, “Powder Metallurgy Processing of a W<sub>x</sub>TaTiVCr High-Entropy Alloy and Its Derivative Alloys for Fusion Material Applications,” *Sci. Rep.*, vol. 7, no. 1, pp. 1–14, 2017, doi: 10.1038/s41598-017-02168-3.
- [126] Y. D. Wu *et al.*, “A refractory Hf<sub>25</sub>Nb<sub>25</sub>Ti<sub>25</sub>Zr<sub>25</sub> high-entropy alloy with excellent structural stability and tensile properties,” *Mater. Lett.*, vol. 130, pp. 277–280, 2014, doi: 10.1016/j.matlet.2014.05.134.
- [127] O. N. Senkov, G. B. Wilks, D. B. Miracle, C. P. Chuang, and P. K. Liaw, “Refractory high-entropy alloys,” *Intermetallics*, vol. 18, no. 9, pp. 1758–1765, 2010, doi: 10.1016/j.intermet.2010.05.014.
- [128] H. Yao *et al.*, “High strength and ductility AlCrFeNiV high entropy alloy with hierarchically heterogeneous microstructure prepared by selective laser melting,” *J. Alloys Compd.*, vol. 813, p. 152196, 2020, doi: 10.1016/j.jallcom.2019.152196.
- [129] S. Son *et al.*, “Superior antifouling properties of a CoCrFeMnNi high-entropy alloy,” *Mater. Lett.*, vol. 300, no. May, p. 130130, 2021, doi: 10.1016/j.matlet.2021.130130.
- [130] S. Daryoush, H. Mirzadeh, and A. Ataie, “Amorphization, mechano-crystallization, and crystallization kinetics of mechanically alloyed AlFeCuZnTi high-entropy alloys,” *Mater. Lett.*, vol. 307, no. October 2021, p. 131098, 2022, doi: 10.1016/j.matlet.2021.131098.
- [131] Y. P. Wang, B. S. Li, M. X. Ren, C. Yang, and H. Z. Fu, “Microstructure and compressive properties of AlCrFeCoNi high entropy alloy,” *Mater. Sci. Eng. A*, vol. 491, no. 1–2, pp. 154–158, 2008, doi: 10.1016/j.msea.2008.01.064.
- [132] S. Xia, Z. Xia, D. Zhao, Y. Xie, X. Liu, and L. Wang, “Microstructure formation mechanism and corrosion behavior of FeCrCuTiV two-phase high entropy alloy prepared by different processes,” *Fusion Eng. Des.*, vol. 172, no. July, p. 112792, 2021, doi: 10.1016/j.fusengdes.2021.112792.
- [133] M. A. Avila-Rubio *et al.*, “Microstructure and microhardness of high entropy alloys with Zn addition: AlCoFeNiZn and AlCoFeNiMoTiZn,” *Adv. Powder Technol.*, vol. 32, no. 12, pp. 4687–4696, 2021, doi: 10.1016/j.apt.2021.10.012.
- [134] Q. Ye, B. Yang, G. Yang, J. Zhao, and Z. Gong, “Stability prediction of AlCoCrFeMo0.05Ni2 high entropy alloy by Kinetic Monte Carlo method,” *Mater. Lett.*, vol. 306, no. June 2021, p. 130907, 2022, doi: 10.1016/j.matlet.2021.130907.
- [135] L. J. Zhang *et al.*, “Effect of solid carburization on the surface microstructure and mechanical properties of the equiatomic CoCrFeNi high-entropy alloy,” *J. Alloys Compd.*, vol. 769, pp. 27–36, 2018, doi: 10.1016/j.jallcom.2018.07.329.
- [136] A. Nishimoto, T. Fukube, and T. Maruyama, “Microstructural, mechanical, and corrosion properties of plasma-nitrided CoCrFeMnNi high-entropy alloys,” *Surf. Coatings Technol.*, vol. 376, no. July 2018, pp. 52–58, 2019, doi: 10.1016/j.surfcoat.2018.06.088.
- [137] A. Günen, “Tribocorrosion behavior of boronized Co<sub>1.19</sub>Cr<sub>1.86</sub>Fe<sub>1.30</sub>Mn<sub>1.39</sub>Ni<sub>1.05</sub>Al<sub>0.17</sub>B<sub>0.04</sub> high entropy alloy,” *Surf. Coatings Technol.*, vol. 421, no. May, p. 127426, 2021, doi: 10.1016/j.surfcoat.2021.127426.
- [138] M. S. Karakaş *et al.*, “Microstructure, some mechanical properties and tribocorrosion wear behavior of boronized Al<sub>0.07</sub>Co<sub>1.26</sub>Cr<sub>1.80</sub>Fe<sub>1.42</sub>Mn<sub>1.35</sub>Ni<sub>1.10</sub> high entropy alloy,” *J. Alloys Compd.*, vol. 886, p. 161222, 2021, doi: 10.1016/j.jallcom.2021.161222.
- [139] R. J. Scales, D. E. J. Armstrong, A. J. Wilkinson, and B. S. Li, “On the brittle-to-ductile

- transition of the as-cast TiVNbTa refractory high-entropy alloy," *Materialia*, vol. 14, no. September, 2020, doi: 10.1016/j.mtla.2020.100940.
- [140] M. Wang, Z. Ma, Z. Xu, and X. Cheng, "Microstructures and mechanical properties of HfNbTaTiZrW and HfNbTaTiZrMoW refractory high-entropy alloys," *J. Alloys Compd.*, vol. 803, pp. 778–785, 2019, doi: 10.1016/j.jallcom.2019.06.138.
- [141] F. Liu, P. K. Liaw, and Y. Zhang, "Recent Progress with BCC-Structured High-Entropy Alloys," *Metals (Basel)*, vol. 12, no. 3, 2022, doi: 10.3390/met12030501.
- [142] M. Wang, Z. L. Ma, Z. Q. Xu, and X. W. Cheng, "Designing VxNbMoTa refractory high-entropy alloys with improved properties for high-temperature applications," *Scr. Mater.*, vol. 191, pp. 131–136, 2021, doi: 10.1016/j.scriptamat.2020.09.027.
- [143] C. C. Tung, J. W. Yeh, T. tsung Shun, S. K. Chen, Y. S. Huang, and H. C. Chen, "On the elemental effect of AlCoCrCuFeNi high-entropy alloy system," *Mater. Lett.*, vol. 61, no. 1, pp. 1–5, 2007, doi: 10.1016/j.matlet.2006.03.140.
- [144] H. Wu, S. Zhang, Z. Y. Wang, C. H. Zhang, H. T. Chen, and J. Chen, "New studies on wear and corrosion behavior of laser cladding FeNiCoCrMox high entropy alloy coating: The role of Mo," *Int. J. Refract. Met. Hard Mater.*, vol. 102, no. October 2021, 2022, doi: 10.1016/j.ijrmhm.2021.105721.
- [145] V. K. Soni, S. Sanyal, and S. K. Sinha, "Influence of tungsten on microstructure evolution and mechanical properties of selected novel FeCoCrMnWx high entropy alloys," *Intermetallics*, vol. 132, no. March, p. 107161, 2021, doi: 10.1016/j.intermet.2021.107161.
- [146] Y. Dong and Y. Lu, "Effects of Tungsten Addition on the Microstructure and Mechanical Properties of Near-Eutectic AlCoCrFeNi2 High-Entropy Alloy," *J. Mater. Eng. Perform.*, vol. 27, no. 1, pp. 109–115, 2018, doi: 10.1007/s11665-017-3096-6.
- [147] N. Malatji, T. Lengopeng, S. Pityana, and A. P. I. Popoola, "Microstructural, mechanical and electrochemical properties of AlCrFeCuNiWx high entropy alloys," *J. Mater. Res. Technol.*, vol. 11, pp. 1594–1603, 2021, doi: 10.1016/j.jmrt.2021.01.103.
- [148] B. Yin, F. Maresca, and W. A. Curtin, "Vanadium is an optimal element for strengthening in both fcc and bcc high-entropy alloys," *Acta Mater.*, vol. 188, pp. 486–491, 2020, doi: 10.1016/j.actamat.2020.01.062.
- [149] H. Arabnejad, A. Mansouri, S. A. Shirazi, and B. S. McLaury, "Evaluation of solid particle erosion equations and models for oil and gas industry applications," *Proc. - SPE Annu. Tech. Conf. Exhib.*, vol. 2015-Janua, no. April 2016, pp. 3603–3621, 2015, doi: 10.2118/174987-ms.
- [150] F. Cernuschi *et al.*, "Solid particle erosion of thermal spray and physical vapour deposition thermal barrier coatings," *Wear*, vol. 271, no. 11–12, pp. 2909–2918, 2011, doi: 10.1016/j.wear.2011.06.013.
- [151] R. B. Nair, G. Perumal, and A. McDonald, "Effect of Microstructure on Wear and Corrosion Performance of Thermally-Sprayed AlCoCrFeMo High Entropy Alloy Coatings," *Adv. Eng. Mater.*, vol. 2101713, pp. 1–16, 2022, doi: 10.1002/adem.202101713.
- [152] W. C. Oliver, "<Nanoindentation\_review.pdf>," 2004.
- [153] A. Meghwal *et al.*, "Multiscale mechanical performance and corrosion behaviour of plasma sprayed AlCoCrFeNi high-entropy alloy coatings," *J. Alloys Compd.*, vol. 854, p. 157140, 2021, doi: 10.1016/j.jallcom.2020.157140.
- [154] P. Patel *et al.*, "Microstructural and Tribological Behavior of Thermal Spray CrMnFeCoNi High Entropy Alloy Coatings," *J. Therm. Spray Technol.*, vol. 31, no. 4, pp. 1285–1301, 2022, doi: 10.1007/s11666-022-01350-y.

- [155] Y. Cui, J. Shen, S. M. Manladan, K. Geng, and S. Hu, “Strengthening mechanism in two-phase FeCoCrNiMnAl high entropy alloy coating,” *Appl. Surf. Sci.*, vol. 530, p. 147205, 2020, doi: 10.1016/j.apsusc.2020.147205.
- [156] A. S. M. Ang *et al.*, “Plasma-Sprayed High Entropy Alloys: Microstructure and Properties of AlCoCrFeNi and MnCoCrFeNi,” *Metall. Mater. Trans. A Phys. Metall. Mater. Sci.*, vol. 46, no. 2, pp. 791–800, 2015, doi: 10.1007/s11661-014-2644-z.
- [157] Z. Bergant and J. Grum, “Porosity evaluation of flame-sprayed and heat-treated nickel-based coatings using image analysis,” *Image Anal. Stereol.*, vol. 30, no. 1, pp. 53–62, 2011, doi: 10.5566/ias.v30.p53-62.
- [158] A. A. Coatings, W. Tillmann, O. Khalil, and M. Abdulgader, “Porosity Characterization and Its Effect on Thermal,” 2019.
- [159] W. H. Liu *et al.*, “Ductile CoCrFeNiMox high entropy alloys strengthened by hard intermetallic phases,” *Acta Mater.*, vol. 116, no. September, pp. 332–342, 2016, doi: 10.1016/j.actamat.2016.06.063.
- [160] M. Rezvani Rad, M. Mohammadian Bajgiran, C. Moreau, and A. McDonald, “Fabrication of thermally sprayed coating systems for mitigation of ice accumulation in carbon steel pipes and prevention of pipe bursting,” *Surf. Coatings Technol.*, vol. 397, no. June, p. 126013, 2020, doi: 10.1016/j.surfcoat.2020.126013.
- [161] S. T. Dehaghani, A. McDonald, and A. Dolatabadi, “An experimental study of the performance of flame-sprayed Ni-based metal matrix composite coatings as resistive heating elements,” *Proc. Int. Therm. Spray Conf.*, vol. 2019-May, pp. 527–534, 2019.
- [162] M. A. Kretova, R. A. Konchakov, N. P. Kobelev, and V. A. Khonik, “Point Defects and Their Properties in the Fe20Ni20Cr20Co20Cu20 High-Entropy Alloy,” *JETP Lett.*, vol. 111, no. 12, pp. 679–684, 2020, doi: 10.1134/S0021364020120097.
- [163] J. W. Yeh, “Physical Metallurgy of High-Entropy Alloys,” *Jom*, vol. 67, no. 10, pp. 2254–2261, 2015, doi: 10.1007/s11837-015-1583-5.
- [164] G. Niu, G. Saint-Girons, and B. Vilquin, *Epitaxial systems combining oxides and semiconductors*. Elsevier, 2013.
- [165] J. H. Mooij, “Electrical conduction in concentrated disordered transition metal alloys,” *Phys. Status Solidi*, vol. 17, no. 2, pp. 521–530, 1973, doi: 10.1002/pssa.2210170217.
- [166] S. Ciuchi, D. Di Sante, V. Dobrosavljević, and S. Fratini, “The origin of Mooij correlations in disordered metals,” *npj Quantum Mater.*, vol. 3, no. 1, 2018, doi: 10.1038/s41535-018-0119-y.
- [167] R. Mueller, K. Agyeman, and C. C. Tsuei, “Negative-temperature coefficients of electrical resistivity in amorphous La-based alloys,” *Phys. Rev. B*, vol. 22, no. 6, pp. 2665–2669, 1980, doi: 10.1103/PhysRevB.22.2665.
- [168] H. Tanimoto, R. Hozumi, and M. Kawamura, “Electrical resistivity and short-range order in rapid-quenched CrMnFeCoNi high-entropy alloy,” *J. Alloys Compd.*, vol. 896, p. 163059, 2022, doi: 10.1016/j.jallcom.2021.163059.
- [169] A. V. Levy, “The solid particle erosion behavior of steel as a function of microstructure,” *Wear*, vol. 68, no. 3, pp. 269–287, 1981, doi: 10.1016/0043-1648(81)90177-0.
- [170] G. Sundararajan, “A comprehensive model for the solid particle erosion of ductile materials,” *Wear*, vol. 149, no. 1–2, pp. 111–127, 1991, doi: 10.1016/0043-1648(91)90368-5.
- [171] R. Kingswell, D. S. Rickerby, S. J. Bull, and K. T. Scott, “Erosive wear of thermally sprayed tungsten coatings,” *Thin Solid Films*, vol. 198, no. 1–2, pp. 139–148, 1991, doi:

10.1016/0040-6090(91)90332-R.

- [172] R. Gonzalez, A. McDonald, and P. Mertiny, "Effect of flame-sprayed Al-12Si coatings on the failure behaviour of pressurized fibre-reinforced composite tubes," *Polym. Test.*, vol. 32, no. 8, pp. 1522–1528, 2013, doi: 10.1016/j.polymertesting.2013.10.002.
  - [173] X. Wang *et al.*, "Solid particle erosion of alumina ceramics at elevated temperature," *Mater. Chem. Phys.*, vol. 139, no. 2–3, pp. 765–769, 2013, doi: 10.1016/j.matchemphys.2013.02.029.
  - [174] E. Bousser, L. Martinu, and J. E. Klemberg-Sapieha, "Solid particle erosion mechanisms of hard protective coatings," *Surf. Coatings Technol.*, vol. 235, pp. 383–393, 2013, doi: 10.1016/j.surfcoat.2013.07.050.
  - [175] K. Bobzin, W. Wietheger, M. A. Knoch, and A. Schacht, "Heating behaviour of plasma sprayed TiO<sub>x</sub>/Cr<sub>2</sub>O<sub>3</sub> coatings for injection moulding," *Surf. Coatings Technol.*, vol. 399, no. January, p. 126199, 2020, doi: 10.1016/j.surfcoat.2020.126199.
  - [176] J. M. Lamarre, P. Marcoux, M. Perrault, R. C. Abbott, and J. G. Legoux, "Performance analysis and modeling of thermally sprayed resistive heaters," in *Journal of Thermal Spray Technology*, Aug. 2013, vol. 22, no. 6, pp. 947–953, doi: 10.1007/s11666-013-9946-3.
  - [177] S. T. Dehaghani, A. Dolatabadi, and A. McDonald, "Thermally sprayed metal matrix composite coatings as heating systems," *Appl. Therm. Eng.*, vol. 196, no. July, 2021, doi: 10.1016/j.aplthermaleng.2021.117321.
- 
- [178] B.S. Murty, J.W. Yeh, S. Ranganathan, and P.P. Bhattacharjee, "High-entropy alloys,". Elsevier, 2019.
  - [179] C. Sandberg, *et al.*, "Chapter B6: Heat Tracing of Piping Systems", Piping Handbook, McGraw-Hill Education, 2000, pp. B.242-B243.
  - [180] H. F. Younis, R. S. Dahbura and J. H. Lienhard V, "Thin film resistance heaters for high heat flux jet-array cooling experiments," vol. 353, pp. 127-134, 1997.
  - [181] G.E. Dieter, and D. Bacon, *Mechanical metallurgy (Vol. 3)*. New York: McGraw-hill, 1976
  - [182] R. Bhattacharya, O.N. Senkov, A.K. Rai, X. Ma, and P. Ruggiero, High Entropy Alloy Coatings for Application as Bond Coating for Thermal Barrier Coating Systems, *J Therm Spray Tech* (2020) 29:857–893 889 Thermal Spray: Fostering a Sustainable World for a Better Life, 10-12 May 2016 (Shanghai, China), ASM International, 2016, p 279-285
  - [183] Shen WJ, Tsai MH, Tsai KY, et al. Superior oxidation resistance of (Al0.34Cr0.22Nb0.11Si0.11Ti0.22)50N50 high entropy nitride. *J Electrochem Soc.* 2013;160:C531–C535.

## Appendix

### Two-Sample *t*-test

A two-sample *t*-test is defined as a statistical hypothesis testing technique in which two independent samples are compared to determine if the means of two populations are statistically different. The two-sample *t*-test is used when the standard deviations of the populations to be compared are unknown and the sample size is small.

$$t = \frac{(\mu_1 - \mu_2)}{S_p^2 \sqrt{\left(\frac{1}{n_1} + \frac{1}{n_2}\right)}} \quad (9)$$

$$S_p^2 = \frac{S_1^2(n_1-1) + S_2^2(n_2-1)}{(n_1+n_2-2)} \quad (10)$$

Where,  $\mu_1$  and  $\mu_2$  are the sample means,  $n_1$  and  $n_2$  are the sample sizes,  $S_p^2$  is the estimate of common variance computed using equation 10.  $S_1^2$  and  $S_2^2$  are the two individual sample variances.

### Python Code for Paired *t*-test for analyzing difference in Joule heating performance

```
def bootstrap(sample, size=10):
    return np.random.choice(sample, size)

AlCoCrFeMo = bootstrap([0.0162, 0.15285, 0.29142])
AlCoCrFeMoW = bootstrap([0.01655, 0.11463, 0.26239])
AlCoCrFeMoV = bootstrap([0.01591, 0.15165, 0.29775])
```

```

Ni20Cr = bootstrap([0.00551, 0.04534, 0.0991])

materials = {'AlCoCrFeMo': AlCoCrFeMo, 'AlCoCrFeMoW': AlCoCrFeMoW, 'AlCoCrFeMoV': AlCoCrFeMoV, 'Ni20Cr': Ni20Cr}

for id, material in materials.items():
    for id_another, another_material in materials.items():
        if id != id_another:
            print(f'Conducting pairwise T-Tes for {id} and {id_another}')
            print(stats.ttest_ind(material, another_material))
            print('')

```

## Output

Conducting pairwise T-Tes for AlCoCrFeMo and AlCoCrFeMoW  
Ttest\_indResult(statistic=0.1978338645988786, pvalue=0.8453920671263961)

---

Conducting pairwise T-Tes for AlCoCrFeMo and AlCoCrFeMoV  
Ttest\_indResult(statistic=0.8629782583162802, pvalue=0.3995021304305474)

---

Conducting pairwise T-Tes for AlCoCrFeMo and Ni20Cr  
Ttest\_indResult(statistic=3.624242639150089, pvalue=0.0019397040399221014)

---

Conducting pairwise T-Tes for AlCoCrFeMoW and AlCoCrFeMo  
Ttest\_indResult(statistic=-0.1978338645988786, pvalue=0.8453920671263961)

---

Conducting pairwise T-Tes for AlCoCrFeMoW and AlCoCrFeMoV  
Ttest\_indResult(statistic=0.623077155801088, pvalue=0.5410487644497303)

---

Conducting pairwise T-Tes for AlCoCrFeMoW and Ni20Cr  
Ttest\_indResult(statistic=2.861343252718938, pvalue=0.010375297501606503)

---

Conducting pairwise T-Tes for AlCoCrFeMoV and AlCoCrFeMo  
Ttest\_indResult(statistic=-0.8629782583162802, pvalue=0.3995021304305474)

---

Conducting pairwise T-Tes for AlCoCrFeMoV and AlCoCrFeMoW  
Ttest\_indResult(statistic=-0.623077155801088, pvalue=0.5410487644497303)

---

Conducting pairwise T-Tes for AlCoCrFeMoV and Ni20Cr  
Ttest\_indResult(statistic=1.9038729649577275, pvalue=0.04303931303971115)

---

Conducting pairwise T-Tes for Ni20Cr and AlCoCrFeMo  
Ttest\_indResult(statistic=-3.624242639150089, pvalue=0.0019397040399221014)

---

Conducting pairwise T-Tes for Ni20Cr and AlCoCrFeMoW

```
Ttest_indResult(statistic=-2.861343252718938, pvalue=0.010375297501606503)
```

---

```
Conducting pairwise T-Tes for Ni20Cr and AlCoCrFeMoV  
Ttest_indResult(statistic=-1.9038729649577275, pvalue=0.04303931303971115)
```

---

### Python Code for Independent two sample *t*-test to investigate the difference in erosion performance at room and elevated temperatures

```
import numpy as np
from scipy import stats

# T-test for difference in mean for AlCoCrFeMo
"""

Null Hypothesis: There is no significant difference in mean of erosion rate between samples at R
T and 250
Alternate Hypothesis: there is a significant difference in mean of erosion rate

Alpha: 5%
Beta: 80%

"""

rt = [0.47713717693837, 0.547615830674759]
et = [0.827214245732264, 0.686587823957779]

# Note: Sample size is different and each sample is indepenet to one another
# We will use 2 sample t-test for equal variance

stats.ttest_ind(rt, et)
```

### Output

```
Ttest_indResult(statistic=-3.1090376372122783, pvalue=0.08974546279588673)
```

```
# T-test for difference in mean for AlCoCrFeMoW
"""

Null Hypothesis: There is no significant difference in mean of erosion rate between samples at R
T and 250
Alternate Hypothesis: there is a significant difference in mean of erosion rate

Alpha: 5%
```

Beta 80%

""

rt = [0.642879564716962, 0.549963377628962]

et = [0.601443967772314, 0.611488960971016, 0.68933765826096]

# Note: Sample size is different and each sample is indepenet to one another  
# We will use 2 sample t-test for equal variance

stats.ttest\_ind(rt, et)

Output

Ttest\_indResult(statistic=-0.7556624454122501, pvalue=0.5047698223225346)

# T-test for difference in mean for AlCoCrFeMoV

""

Null Hypothesis: There is no significant difference in mean of erosion rate between samples at R T and 250

Alternate Hypothesis: there is a significant difference in mean of erosion rate

Alpha: 5%

Beta 80%

""

rt = [0.863959102527692, 0.480545299630787]

et = [0.560636182902584, 0.61005396194263, 0.68673672252201]

# Note: Sample size is different and each sample is indepenet to one another  
# We will use 2 sample t-test for equal variance

stats.ttest\_ind(rt, et)

Output

Ttest\_indResult(statistic=0.3528103025785154, pvalue=0.7475635847327808)

## Python Code for Paired *t*-test for analyzing difference in solid particle erosion performance for the three HEA coatings

```
# Pairwise T-test with bootstrap
```

```
def bootstrap(sample, size=50):
    return np.random.choice(sample, size)

materials = {'AlCoCrFeMo': AlCoCrFeMo, 'AlCoCrFeMoW': AlCoCrFeMoW, 'AlCoCrFeMoV':
: AlCoCrFeMoV, 'steel': steel}

for id, material in materials.items():
    for id_another, another_material in materials.items():
        if id != id_another:
            print(f'Conducting pairwise T-Tes for {id} and {id_another}')
            print(stats.ttest_ind(bootstrap(material), bootstrap(another_material)))
            print('')
```

### Output

```
Conducting pairwise T-Tes for AlCoCrFeMo and AlCoCrFeMoW
Ttest_indResult(statistic=-1.605855657570311, pvalue=0.11152327650539004)
```

---

```
Conducting pairwise T-Tes for AlCoCrFeMo and AlCoCrFeMoV
Ttest_indResult(statistic=-4.147749462903844, pvalue=7.15086209192842e-05)
```

---

```
Conducting pairwise T-Tes for AlCoCrFeMoW and AlCoCrFeMo
Ttest_indResult(statistic=1.605855657570311, pvalue=0.11152327650539004)
```

---

```
Conducting pairwise T-Tes for AlCoCrFeMoW and AlCoCrFeMoV
Ttest_indResult(statistic=-3.258133738642143, pvalue=0.001541731350523742)
```

---

```
Conducting pairwise T-Tes for AlCoCrFeMoV and AlCoCrFeMo
Ttest_indResult(statistic=4.147749462903844, pvalue=7.15086209192842e-05)
```

---

```
Conducting pairwise T-Tes for AlCoCrFeMoV and AlCoCrFeMoW
Ttest_indResult(statistic=3.258133738642143, pvalue=0.001541731350523742)
```

---